

FAR INFRARED ABSORPTION BY SMALL PARTICLES

By

YOUNG HOON KIM

A DISSERTATION PRESENTED TO THE GRADUATE SCHOOL
OF THE UNIVERSITY OF FLORIDA IN
PARTIAL FULFILLMENT OF THE REQUIREMENTS
FOR THE DEGREE OF DOCTOR OF PHILOSOPHY

UNIVERSITY OF FLORIDA

1986

ACKNOWLEDGMENTS

It is my great pleasure to thank my advisor Professor D. B. Tanner for his guidance, patience, valuable advice, and support on all levels during my graduate career. Also, I would like to thank Professors N. S. Sullivan, P. Sikivie, S. E. Nagler, and G. B. Hoflund for serving on my supervisory committee.

I am grateful to my fellow students for their friendship and cooperation during my five years stay in the FIR (far-infrared) group. In particular, members of the "Florida FIR group"—C. D. Porter, X. Q. Yang, Drs. R. P. McCall, M. Gutowski, M. Gutowska, I. Hamburg, A. Memon, and, of course, D. B. Tanner—have provided a pleasant research environment. In addition, I should like to mention C. D. Porter for his help in numerical calculations and computer programming. Also, my Korean fellow students in the physics department deserve thanks for sharing friendship and useful conversation.

My recent experience with the "Florida Axion group" was special and exciting and I give thanks to its members.

A special acknowledgment goes to Dr. J. Newkirk at Major Analytical Instrument Center for TEM (transmission electron microscope) analysis, to H. Nachtrieb and his crew members for their fine machining works, and to D. Sanford and C. Fombarlet for general

technical help and for supplying liquid helium. I am thankful to Karen Teele for typing the first version of this dissertation, to Sofia Kohli for her fast and accurate typing of the final version, to C. Fombarlet for his technical drawings, and to H. Schrader for printing all TEM pictures used in this dissertation.

Finally, very special thanks go to my wife, Hye Kyong, and my son, Eugene, for their love, care and understanding, and to my parents for their love and support from Korea.

TABLE OF CONTENTS

	Page
ACKNOWLEDGMENTS	ii
ABSTRACT	vi
CHAPTER	
I INTRODUCTION	1
Statement of the Problem	1
Review	12
Theory	15
Search for the Solution	27
II EXPERIMENT	31
Sample Preparation and Characterization	31
Infrared and Optical Technique	47
Instrumentation	51
Measurement	55
III RESULTS	59
FIR Data	59
MIR Data	70
Visible Frequency Data	84
Nonmetallic Possibility	89
IV THEORY	95
Formalism	95
Small Particle and Matrix Element	102
Calculation of $\epsilon(\omega)$	107
The Classical (Bulk) Limit	129
The Small Particle Problem	133
V SUMMARY AND CONCLUSION	149

APPENDIX	<u>Page</u>
A SURFACE ROUGHNESS	152
B LEVEL STATISTICS	160
C INTERBAND TRANSITION	169
D RECOVERY OF THE BULK NATURE	175
E AN UNSUCCESSFUL MODEL CALCULATION	179
REFERENCES	190
BIOGRAPHICAL SKETCH	196

Abstract of Dissertation Presented to the Graduate School
of the University of Florida in Partial Fulfillment of the
Requirements for the Degree of Doctor of Philosophy

FAR INFRARED ABSORPTION BY SMALL PARTICLES

By

Young Hoon Kim

May 1986

Chairman: David B. Tanner
Major Department: Physics

The properties of small metal particles of the order of 100 \AA size have been studied. In particular, the anomalously large far infrared absorption by small particles has been a puzzling problem since its discovery in 1972. Even though many experimental and theoretical efforts have been made to understand this peculiar phenomenon, no clear answer has been made yet. In order to understand the underlying physics of the anomalous far infrared response of a small "metallic" system whose geometrical dimension is smaller than any characteristic length scale, a question about the fundamental nature of a small particle was raised and investigated both experimentally and theoretically in this work.

For the measurements, small metal particles (Al, Ag, or Au) were mixed with insulating particles (KCl or paraffin), with the small particle-insulator mixture being then compressed into a pellet.

Transmission electron microscopy of ion-milled or chemically polished samples showed the random nature of the small particle composite. The far infrared through visible frequency optical properties of samples having metal fractions between 0.0001 and 0.032 were measured. A persistent anomalously large far infrared absorption was observed, which could not be explained by existing theories.

In the mid-infrared frequency range, the absorption was smaller and could be fit to classical theories by assuming an unexpectedly short electronic mean free path. An extremely broad surface plasmon resonance was observed for Ag-KCl and Au-KCl composite system. Additionally, different energy band structure from the bulk state was found for aluminum small particles.

Theoretical work included calculations of the dielectric function of a small particle at frequencies near the size-quantization energy gap. These calculations showed that the particle behaved as an insulator rather than as a small solid metal.

CHAPTER I INTRODUCTION

This dissertation explores the far-infrared (FIR), the mid-infrared (MIR), and the optical properties of small "metallic" particles experimentally and theoretically. In this work, three different kinds of small particles (Al, Ag, and Au) were studied. These small particles were dispersed in an insulating medium (KCl or paraffin) for experimental measurements of the electromagnetic response.

One might expect that the properties of a small particle would be different from those of an infinite metallic system when the geometrical size of a metal is smaller than the physical characteristic length scale. Also, one might think some unusual physical properties arise from the smallness of the size of the particles. This aspect will be extensively studied and discussed in this work.

Statement of the Problem

Metals

A metal is a type of condensed matter with high electrical conductivity. A great detail of metal physics, both the static and the dynamic properties of the electrons such as heat capacity, magnetic susceptibility, electron spin resonance, and electromagnetic properties, etc., is now understood.^{1,2}

When isolated metal atoms are brought together to form a solid, the valence electrons interact with their counterparts on neighboring

atoms. As a result of this interaction the electrons are no longer effectively associated with any particular constituent atom. In contrast, the core electrons are generally unaffected by the condensation and remain bound to individual nuclei. Consequently, we can view a solid crystalline metal as having two structural units. One is the group of positive ions which are on the regular periodic lattice sites and which usually are treated as a positive jellium background in a theoretical calculation. The other is the group of conduction electrons, which are distributed throughout the interionic space and which often are modeled as an electron gas or a Fermi liquid. At zero temperature these conduction electrons fill all available energy levels up to a maximum energy which is called the Fermi energy. The energy distribution function of the electrons has a sharp discontinuity at the Fermi energy regardless of any interactions, although interactions such as impurity scattering causes a smearing of the discontinuous step in their momentum distribution function. Therefore, we can characterize a metal as a system which has a Fermi surface and easily accessible, vacant excited energy states available to the conduction electrons.

The existence of the conduction electrons leads to the interesting physical properties of a metal such as the conduction electron energy band which consists of many energy levels and a collective excitation (plasma oscillation) of the free electrons. The origin of the discrete energy levels in which the electrons can be excited in response to the external influences, such as external electromagnetic fields or temperature gradient, lies in the quantization of the kinetic

energy of electrons. Since there are about 10^{23} electrons/cm³ in a typical metal, their average energy level spacing would be the order of 10^{-10} eV, which essentially represents the continuum states.

In order to study the physics of the conduction electrons, an important quantity to understand is the electrical conductivity (or dielectric function) of a metal. If there was no lattice excitation (phonon) and no lattice defects in an entirely pure metal, there would be no scattering of the electrons by the structure and the conductivity $\sigma(\omega)$ of the system would be

$$\sigma(\omega) = \frac{ne^2}{m} \frac{\pi}{2} \delta(\omega) \quad (1.1)$$

where n is the electron number density, m is the electron mass, and ω is the frequency of the applied fields. Equation (1.1) describes a system in which the lifetime of the electrons is infinity. However, because in actual metals the conduction electrons interact with each other, with the ions, and especially with the impurity atoms, the lifetime of a free electron between collisions becomes rather short, leading to a finite dc conductivity and the optical conductivity as

$$\sigma(\omega) = \frac{\sigma_0}{1 + i\omega\tau} \quad (1.2)$$

Here $\sigma_0 = \frac{ne^2\tau}{m}$ and τ is the relaxation time, which is assumed to be constant.

However, one difficulty in the free electron gas approximation is that a free electron gas cannot absorb a photon because an electron

cannot conserve both momentum and energy by absorbing the photon alone; therefore, there is no mechanism for the loss of electromagnetic energy for a metal. Instead, a metal actually absorbs some small amount of radiation energy in the FIR region where the electrons in metals show an outstanding free electron gas nature. Holstein³ showed that there exists two dissipative processes in a metal: One is due to the presence of a surface which enables the electrons to acquire an energy from the oscillating external electric field when they pass through the skin depth layer, and then the absorbed energy is converted into heat through the diffuse collision with the surface. The other is a bulk process which is known as the Holstein process. The conduction electron absorbs an incident photon and emits a phonon simultaneously. Consequently, a metal does absorb the FIR photon because the collision with the surface or the Holstein process allows the conservation of both energy and momentum for an electron. But, these realistic contributions modify the relaxation time of an electron to be weakly frequency dependent, modify the Drude behavior to some extent.

Now, what will happen if we reduce the geometrical dimension of a metal to a scale which is smaller than any physical characteristic length such as the electron mean free path in a metal, penetration depth of fields, the wave length of the external fields, and the electron coherence length, but still large enough to be called a small solid metal?

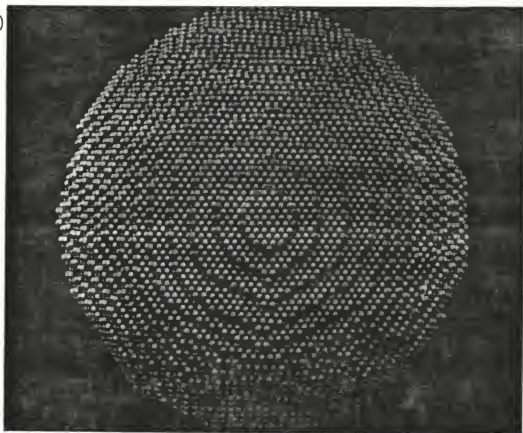
Small Particles

Because the size of the metal is smaller than the electron mean free path, the conduction electrons now can see the surface. In other words, the translational symmetry in the motion of electrons is broken. One of the consequences of the broken symmetry is that the surface plays a direct quantum mechanical role and actually determines the eigenstates of electrons bound within the finite volume of a particle. If we model a small particle as a spherical box filled with electron gas and assume that the smooth and regular surface serves as an infinite potential barrier, the corresponding eigenstates would be highly degenerate, and the average energy gap ΔE would be the order of $E_F/N_e^{1/3}$ where E_F is the Fermi energy and N_e is the number of electrons in the system. But, as proposed first by Kubo⁴ the random irregularity of the surface is sufficient to break the degeneracy and to randomize the distribution of levels (a simple illustration is presented in Appendix A). Therefore, the corresponding energy gap would be the order of E_F/N_e if all the degeneracy is lifted and the distribution would follow a Poisson distribution. As shown in Figure 1.1, a model of a small particle with an FCC structure reconstructed from the Field Ion Microscope analysis of tungsten⁵ is indeed rough to atomic scale and indirectly justifies the choice of the random distribution of the energy levels. However, the correlation between the energy levels in such a random system imposed an importance of the statistics of new classes of ensemble which was hypothesized by Dyson⁶ and was first applied to the small particle problem by Gor'kov and Eliashberg⁷ (see Appendix B).

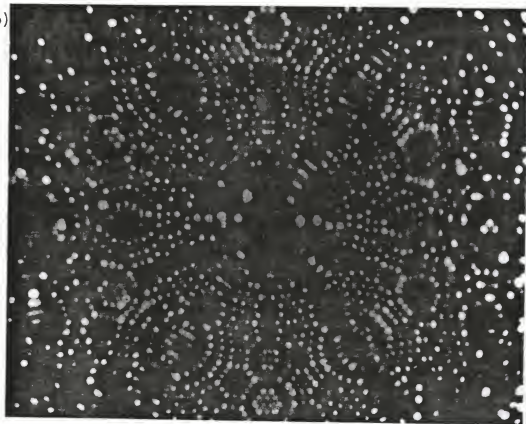
Figure 1.1 Small particle model

- (a) A model of a small particle reconstructed from the Field Ion Microscope analysis. (Reference 5)
- (b) A Field Ion Micrograph of Tungsten tip (Reference 5); the center axis is $[011]$

(a)



(b)



Another consequence of the smallness of a metal particle is the broken symmetry in the Bloch state at the surface which has been ignored in the experiment and many body theories for a bulk metal because of the negligible surface to volume ratio. As the size of the system gets smaller, however, this ratio no longer is negligible. Because the ratio of the number of the surface atoms, N_s , to the number of the total atoms, N , for a small particle is proportional to $N^{-1/3}$, the role of the surface imperfections (vacancies and impurities) which localizes electrons at the surface and forms of the localized band between the conduction and the valence bands of a metal^{8,9} should be appreciable experimentally for a small particle as a result of the quantum size effect.

Lower Bound to the Smallness

It is instructive to consider a lower limit to the size of a small particle to retain the metallic characteristic (free conduction electrons). Obviously, as the size of a particle decreases, the metallic nature of a particle will disappear and the particle will eventually recover the molecular behavior. In other words, we can set a criterion to determine the metal-insulator (molecule) transition of a small particle by considering two energy scales in a similar way to that done by Thouless¹⁰: One is the gap energy (ΔE) due to the level quantization

$$\Delta E = \frac{1}{\nu(E_F)} = \frac{2E_F}{3N_e} \quad (1.3)$$

and the other is the energy (δE) associated with the diffusion time τ_D

$$\delta E = \frac{\hbar}{\tau_D} \quad (1.4)$$

Now, when the gap energy wins over δE (i.e., $\Delta E/\delta E > 1$), the electrons are no longer free electrons. Also, the electrons are in the extended states when $\Delta E/\delta E < 1$. Therefore, at the transition point ($\Delta E/\delta E = 1$), we have a critical particle radius a_c as

$$a_c = \left(\frac{E_F \tau_D}{2\pi n \hbar} \right)^{1/3} \quad (1.5)$$

where n is the electron density. For example, $a_c(\text{Al}) = 5 \text{ \AA}$ with $\tau_D = 0.8 \times 10^{-14} \text{ sec}$, $n = 18.06 \times 10^{22}$, and $E_F = 11.63 \text{ eV}$ for aluminum and for silver, $a_c(\text{Ag}) = 9.7 \text{ \AA}$ with $\tau_D = 4.0 \times 10^{-14} \text{ sec}$, $n = 5.85 \times 10^{22}$, and $E_F = 5.48 \text{ eV}$. Here the τ_D for the bulk state has been used because we reduce the geometrical dimension of a particle from its bulk state.

Also, this criterion can be compared with the Ioffe-Regel metal-insulator transition criterion¹¹

$$k_F a \leq 2\pi \quad (1.6)$$

which gives $a(\text{Al}) = 3.59 \text{ \AA}$ and $a(\text{Ag}) = 5.24 \text{ \AA}$.

Therefore, the argument given in this section assures that we are dealing with small "metal" particles and justifies the theoretical model of electron gas in a restricted geometry.

Anomalous Far-Infrared (FIR) Absorption

It has been understood that the classical theory of scattering and absorption of electromagnetic wave by a small particle, which is known as the Mie theory, is almost complete. One of the most successful achievements of the classical scattering theory is the prediction of the surface plasmon mode in a small particle which originates from the limitation of the long-range correlation of the electrons by the surface (i.e., a collective oscillation caused by a restoring force from the induced charge on the surface). This is also known as the Mie or Maxwell-Garnett resonance.

From the classical point of view, introducing the surface means that the scattering of electrons by the surface should be included. This can be done by adding a surface scattering contribution to the relaxation time, τ , of the electrons in the Drude formula given by Equation (1.2)

$$\frac{1}{\tau} = \frac{1}{\tau_b} + \frac{1}{\tau_s} \quad (1.7)$$

where τ_b is the relaxation time for the electrons in a bulk metal, $\tau_s = a/v_F$, a is the radius of the particle and v_F is the Fermi velocity. Because the Drude dielectric function with the modified relaxation time explains qualitatively the observed small particle effect in the visible frequency range,¹² it had been believed that the same is true in the FIR range as shown in Figure 1.2 until the anomalous FIR absorption by small metallic particles which shows a contradiction to the

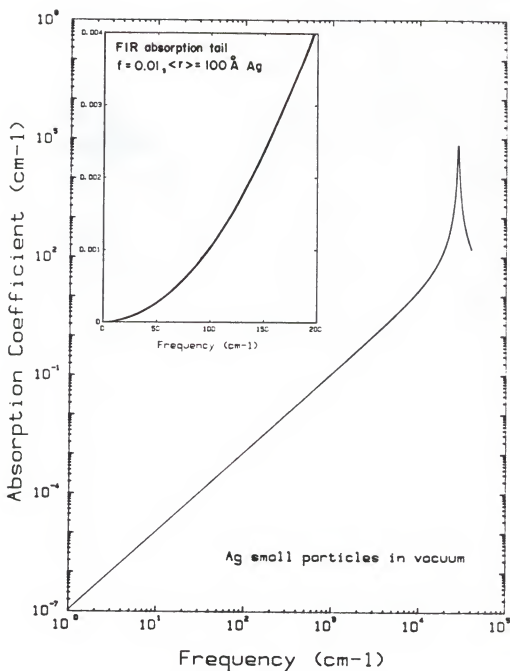


Figure 1.2 The Maxwell-Garnett resonance of Ag particles in a vacuum on the basis of classical theory ($f = 0.01$, $\epsilon_{\infty} = 4.83$, $\langle a \rangle = 100 \text{ \AA}$, $\omega_p = 7.31 \times 10^4 \text{ cm}^{-1}$); the small insert shows the FIR tail

prediction of the classical theory was discovered by Tanner¹³ in 1972. The experimental FIR absorption coefficient for various kinds of metallic particles was orders of magnitude larger than the prediction. Also, he observed some possible evidence of the quantum size effect in small particles which seems to arise from the energy level correlation calculated by Gor'kov and Eliashberg.⁷ But, to the present time, both the classical and the quantum mechanical calculation have failed to give the correct explanation of the anomalous FIR absorption by small particles inspite of the agreement of the frequency dependence with the experimental results and no clear answer has been given yet.

Review

Experiment

The first FIR measurements on a ~ 100 Å size, gas-evaporated small metallic particles were done by Tanner et al.¹⁴ Preparation by gas-evaporation was expected to be a promising method to make well-characterized spherical small particles with controllable parameters such as the average particle size, possibly the particle size distribution, and the thickness of the oxide layer on the surface of the metal particles. The oxide was introduced to guarantee the electrical isolation among the particles. For the FIR study of small particles, they used the samples which contained free-standing smoke (clusters of well-isolated small particles) clamped between two polyethelene pieces. Because the density of the smoke was very low in comparison with that of the bulk state, the volume fraction of the metal in the sample to

vacuum was less than 0.1. The measured FIR absorption coefficients of small particles were proportional to the square of the frequency, but the proportionality constant was anomalously larger than the theoretical results. Also, no temperature dependence of the FIR absorption was found up to 20° K.

Granqvist et al.¹⁵ repeated the FIR measurement on aluminum small particles, confirmed the anomalous FIR absorption, and found the absorption to increase with particle size. But they found no evidence of the Gor'kov and Eliashberg⁷ level correlation effect and they demonstrated the significance of the particle size distribution in the observation of the effect.

A systematic improvement on the sample preparation was made by Russell et al.¹⁶ They were able to control the volume concentration of the small metal particles by using an insulating medium, KCl, as a host. They found out the significance of the eddy current loss in large size particles (1 μm) and the linear dependence on the volume fraction in the absorption coefficient.

At the same period, Carr et al.¹⁷ measured the FIR absorption for relatively smaller sizes of particles than those of Russell et al.,¹⁶ but large enough to ignore the quantum size effect. They obtained similar results to the previous measurements except that the absorption coefficient of aluminum small particles showed a quadratic dependence on volume fraction. They also measured the FIR absorption in Al_2O_3 , which was a possible explanation for the anomalous absorption,¹⁸ and found that the contribution of the metal oxide was not responsible for the anomalous absorption. Except for the Al particles, their FIR data fit

$$\alpha = K_{\text{exp}} f \nu^2 \quad (1.8)$$

where α is the absorption coefficient, K_{exp} is a constant in cm , f is the volume fraction of the metal, and ν is the frequency in cm^{-1} .

Recently, Devaty and Sievers¹⁹ reported a conclusive result about the FIR problem. They studied a different small particle system, 100 Å Ag particles embedded in a gelatin matrix, in which they were able to control the dispersion of the particles and found out that a clustered sample had a much larger FIR absorption coefficient than a well-dispersed sample. But the nonclustered small particle sample still showed a factor of 100 times larger absorption than theory. Also, they confirmed that the absorption coefficient was independent of both temperature and magnetic field (up to 60 kG). However, Lee et al.²⁰ observed a weak temperature dependence of the FIR absorption for fairly large silver particles ($a > 500$ Å) embedded in a Teflon matrix. Also, the authors measured the FIR absorption coefficient which is close to the classical predictions. These results suggest that this size particle no longer retains the effect of the broken symmetry.

The early work on the optical properties of small particles was started by investigating the color change in a colored NaCl from yellow to blue as the sample was annealed in 1905. Since then, many studies have been made on small particles (colloids) in a colored alkali halide crystal.²¹ The interpretation of the color (F) centers and the colloids in the system as a one-component, two-phase thermodynamic system made a successful explanation for the observed phenomena. In other words, the

colloids, precipitates of excess alkali metal, behave like a condensed phase and the F centers behave like a vapor phase. The blue shift in the resonance from the F center peak was interpreted as the corresponding Mie resonance (surface plasmon mode) of the particles. Another system used for the study of the surface plasmon was Au-SiO₂ composite.²² The gold small particles were grown as precipitates by irradiation in SiO₂ matrix. Although in general there was a lack of information about the size distribution and crystallinity of the particles grown in the matrix, the Mie theory was qualitatively successful, even though the experiments showed more broadening in the resonance curve than the theory predicted, as summarized in Table 1.1.²²⁻³¹

Theory

Classical Theory

We want to calculate the electromagnetic response of a particle and the cooperative behavior of a collection of particles dispersed in a medium. The response of a single particle can be calculated by the Mie theory or by the approximation of the quasi-static limit. The details of the Mie theory can be found in a review paper by Carr et al.³² and the references therein. However, the numerical calculation done by Henry³³ showed that the difference between the Mie theory and the quasi-static limit is negligible for the small size particles in which we are interested ($a \sim 100 \text{ \AA}$) and that only dipole terms are important in the Mie series. The quasi-static limit calculation of the electric and magnetic polarizability of a small particle in a dielectric medium can be found either in Jackson or in Landau and Lifshitz.³⁴

Table 1.1 Summary of optical data

Workers	$\langle a \rangle$ (\AA)	$\Delta\nu = \frac{1}{2\pi c} \left(\frac{V_F}{a} \right)$ (cm^{-1})	$\Delta\nu_{\text{obs}}$ (cm^{-1})	ℓ_{fit} (\AA)	System Studied
Scott et al. ²³	50	912	2,060	22	K-KBr
Doyle ²⁴	--	161*	1,610-4,840	36-12	Na-NaCl
Doremus ²²	26	2,836	2,760	27	Au-Glass
	60	1,229	2,140	34	Au-Glass
	100	737	3,560	21	Au-Glass
Jain and Arora ²⁵	75	983	3,810	19	Ag-KCl
Kreibig ²⁶	28	2,634	3,730	20	Au-Glass
Granqvist and Hunderi ²⁷	16	4,610	8,440	8.7	Au deposit on substrate
Norman et al. ²⁸	~ 50	1,470	5,680	13	Discontinuous Au film
Persson and Liebsch ²⁹	~ 50	1,475	12,100	6.1	Ag-gelatin
Gibson and Buhrman ³⁰	~ 50	1,470	14,300	5.1	Au-MgO granular film
	~ 50	1,470	7,580	9.7	Au-Al ₂ O ₃ granular film
Kaiser et al. ³¹	~ 32	2,304	8,066	9.1	Discontinuous Au film

Note: $\langle a \rangle$: average particle radius

*: $a \sim \ell_{\text{bulk}} = 350 \text{ \AA}$

$\Delta\nu$: expected broadening at FWHM

$\Delta\nu_{\text{obs}}$: observed broadening at FWHM

ℓ_{fit} : electron mean free path used to fit to data

In the quasi-static limit, the depolarization field can be regarded as uniform, determined by the depolarization factor. For a sphere, we can write the electric field inside, \vec{E}_{in} , as

$$\vec{E}_{in} = \left(1 - \frac{4\pi}{3} \gamma_e\right) \vec{E} \quad (1.9)$$

where \vec{E} is the applied field and γ_e is the electric polarizability per unit volume of the sphere. Also, by solving the standard boundary value problem, we get

$$\vec{E}_{in} = \frac{3\epsilon_0}{\epsilon_m + 2\epsilon_0} \vec{E} = \left(1 - \frac{\epsilon_m - \epsilon_0}{\epsilon_m + 2\epsilon_0}\right) \vec{E} \quad (1.10)$$

where ϵ_0 , ϵ_m are the dielectric constant of the medium and the particle, respectively. Therefore, from Equations (1.9) and (1.10) we can identify the γ_e as

$$\gamma_e = \frac{3}{4\pi} \left(\frac{\epsilon_m + \epsilon_0}{\epsilon_m + 2\epsilon_0} \right) \quad (1.11)$$

One important remark about the polarizability γ_e in Equation (1.11) is that γ_e is singular when $\epsilon_m(\omega) = -2\epsilon_0$ which predicts the existence of the surface plasmon. For a Drude metal at the high frequencies,

$$\epsilon_m(\omega) \sim 1 - \frac{\omega_p^2}{\omega^2} \quad (1.12)$$

where ω_p is the plasma frequency defined as $\left(\frac{4\pi ne^2}{m}\right)^{1/2}$. Hence, the surface plasmon frequency ω_{sp} is

$$\omega_{sp} = \frac{\omega_p^2}{\sqrt{1 + 2\epsilon_0}} \quad (1.13)$$

The contribution of the magnetic dipole moment in the FIR region is caused by a non-zero magnetization in the medium because of the eddy current. This contribution considered by many workers^{13,15,16,35} is known to be important for a small metal sphere. By solving the boundary value problem of a conducting sphere in a time varying uniform magnetic field, the magnetic polarizability per unit volume γ_m is

$$\gamma_m = \frac{3}{8\pi} \left[\frac{3}{(ka)^2} - 1 - \frac{3}{ka} \cot(ka) \right] \quad (1.14)$$

where $k = \sqrt{\epsilon_m} \frac{\omega}{c}$ is the wave vector inside of the particle.

In order to describe a system with small metal particles in a medium, some kind of averaging process is necessary. One model is the Maxwell-Garnett theory (MGT),³⁶ an analogy to the Clausius-Mossotti formula.³⁷ The MGT gives the effective dielectric function of the system as

$$\frac{\epsilon_{MGT} - \epsilon_0}{\epsilon_{MGT} + 2\epsilon_0} = f \frac{\epsilon_m - \epsilon_0}{\epsilon_m + 2\epsilon_0} \quad (1.15)$$

where ϵ_{MGT} is the effective dielectric function and f is the volume fraction of metal. For a sufficiently dilute system ($f \ll 1$), Equation (1.15) can be approximated as

$$\frac{\epsilon_{\text{MGT}}}{\epsilon_0} = 1 + 4\pi f \gamma_e + \frac{16}{3} \pi^2 f^2 \gamma_e^2 + O(f^3) \quad (1.16)$$

Similarly, the effective magnetic permeability can be expanded within MGT as

$$\mu_{\text{MGT}} = 1 + 4\pi f \gamma_m + O(f^2) \quad (1.17)$$

Here the magnetic permeability of the medium is chosen to be unity.

Therefore, the absorption coefficient α_{MGT} is obtained from

$$\alpha_{\text{MGT}} = \frac{2\omega}{c} \text{Im} \sqrt{\epsilon_{\text{MGT}} \mu_{\text{MGT}}} \quad (1.18)$$

Another averaging process is known as the Bruggeman theory³⁸ or the Effective Medium Approximation (EMA).^{39,40} The EMA asserts that the position-dependent electric field in the medium becomes

$$\vec{E}(\vec{r}) = \left[1 - \frac{\epsilon(\vec{r}) - \epsilon_{\text{EMA}}}{\epsilon(\vec{r}) + 2\epsilon_{\text{EMA}}} \right] \langle \vec{E} \rangle \quad (1.19)$$

therefore

$$\left\langle \frac{\epsilon - \epsilon_{\text{EMA}}}{\epsilon + 2\epsilon_{\text{EMA}}} \right\rangle = 0 \quad (1.20)$$

Here $\epsilon(\vec{r})$ is the position-dependent dielectric function, ϵ_{EMA} is the effective dielectric function, and the angular bracket represents the ensemble average. Now, if we assume that the system satisfies ergodicity, the condition to be satisfied to have a meaning of average for a truly random system, then we can replace the ensemble average with the volume average such as

$$\langle \vec{E} \rangle = f \vec{E}_m + (1 - f) \vec{E}_0 \quad (1.21)$$

where \vec{E}_m is the electric field in particle and \vec{E}_0 is the field in medium. From Equations (1.19) and (1.20) immediately we get

$$\left[f \left(1 - \frac{\epsilon_m - \epsilon_{\text{EMA}}}{\epsilon_m + 2\epsilon_{\text{EMA}}} \right) + (1 - f) \left(1 - \frac{\epsilon_0 - \epsilon_{\text{EMA}}}{\epsilon_0 + 2\epsilon_{\text{EMA}}} \right) \right] = 1 \quad (1.22)$$

It is remarkable that the EMA predicts the metal-insulator transition at $f = \frac{1}{3}$. In contrast, the MGT has no transition point. Again, in the dilute limit

$$\frac{\epsilon_{\text{EMA}}}{\epsilon_0} = 1 + 4\pi f \gamma_e + \frac{16\pi^2 f^2 \gamma_e^2}{\epsilon_m + 2\epsilon_0} + O(f^3) \quad (1.23)$$

The EMA thus predicts the same result as MGT to the first order in f .

In the limit of low frequency and small volume fraction, the problem is now reduced to the calculation of the susceptibilities of a small particle so that from Equations (1.16), (1.17), and (1.18) we have

$$\alpha = \alpha_0 + \frac{4\pi\omega}{c} f \sqrt{\epsilon_0} \text{Im} (\gamma_e + \gamma_m) \quad (1.24)$$

where $\alpha_0 = \frac{2\omega}{c} \sqrt{\epsilon_0}$, absorption by the medium. In the low-frequency limit, the imaginary part of γ_e can be written as

$$\text{Im}\gamma_e = \frac{9\epsilon_0 \omega \sigma_1}{16\pi^2 (\sigma_1^2 + \sigma_2^2)} \quad (1.25)$$

with $\epsilon_m(\omega) = 1 + \frac{4\pi i \sigma(\omega)}{\omega}$ and $\sigma(\omega) = \sigma_1(\omega) + i\sigma_2(\omega)$. Also, by expanding the equation (1.14) in the $ka \ll 1$ limit (however, a little care is necessary during the expansion⁴¹), we get

$$\text{Im}\gamma_m = \frac{1}{40\pi} \text{Im}(ka)^2 = \frac{\omega a^2}{10c^2} \sigma_1 \quad (1.26)$$

Therefore, after subtracting or ignoring the absorption by the medium, the FIR absorption coefficient in MGT becomes

$$\alpha_{\text{MGT}} = f \frac{\omega^2}{c^2} \sqrt{\epsilon_0} \left[\frac{9c\sigma_1\epsilon_0}{4\pi(\sigma_1^2 + \sigma_2^2)} + \frac{2\pi}{5c} a^2 \sigma_1 \right] \quad (1.27)$$

or

$$\alpha_{\text{MGT}} = (K_e + K_m) f \nu^2 \quad (1.28a)$$

in experimentally more appealing form. Here K_e is the proportionality constant of the electric dipole term,

$$K_e \equiv \frac{3\pi\epsilon_0^{3/3} (\sigma_1/30c)}{10[(\sigma_1/30c)^2 + (\sigma_2/30c)^2]} \quad (1.28b)$$

and K_m is the constant for the magnetic dipole contribution,

$$K_m = 48\pi^3 a^2 \epsilon_0^{1/2} (\sigma_1/30c) \quad (1.28c)$$

with $\nu = \omega/2\pi c$ and $\sigma_1/30c$ in $\Omega^{-1}\text{cm}^{-1}$.

A test of whether the measured FIR absorption follows an $\epsilon_0(\omega)^{3/2}$ or an $\epsilon_0(\omega)^{1/2}$ dependence can be done to identify the importance of the electric dipole and the magnetic dipole contributions to the absorption.

Another remark is that there is an enhancement of the static dielectric constant of the small metal particle composite. From Equations (1.16) and (1.23), we have

$$\epsilon_{\text{eff}} \sim (1 + 3f)\epsilon_0 \text{ for } \epsilon_0 \ll \epsilon_m \text{ and } f \ll 1 \quad (1.29)$$

where ϵ_{eff} is the effective dielectric function (either ϵ_{EMA} or ϵ_{MGT}). From a different point of view, Equation (1.29) can be understood as a result of the expansion of

$$\epsilon_{\text{eff}} \sim \epsilon_0 \left(1 - \frac{f}{f_c} \right)^{-\nu} \quad (1.30)$$

with $\nu = 1$ and $f \ll f_c = 1/3$. Equation (1.30) shows the scaling law behavior near the critical volume fraction f_c . The actual value of ν and f_c in a three-dimensional small-particle composite has been measured by Grannan et al.⁴² and calculated by Straley⁴³ and Bergman and Imry.⁴⁴

Quantum Mechanical Theory

Since the kinetic energy of electrons is quantized as discussed earlier, the standard quantum mechanical calculation of the induced dipole moment of the system can be done by treating the interaction $H_1 = e\vec{E} \cdot \vec{r}$ as a perturbation. Here \vec{r} is the position vector of an electron measured with an origin at the center of the system, \vec{E} is the applied electric field, and e is the electron charge. Also, the distinction between the highly degenerate and the nondegenerate energy level contribution to the dipole moment can be realized as follows. To the first order, the perturbed one-electron wave function ψ'_n becomes

$$\psi'_n = \psi_n^0 + \sum_{m \neq n} \frac{\langle m | eEz | n \rangle}{E_m - E_n} \psi_m^0 \text{ with } \vec{E} = Ek \quad (1.31)$$

where ψ_n^0 is the unperturbed n^{th} state eigenfunction, E_n is the corresponding eigenvalue, and k is the z-direction unit vector.

Therefore, the dipole moment p can be calculated by

$$p = \langle \psi'_n | ez | \psi'_n \rangle = \left\{ 2e^2 \sum_{m \neq n} \frac{|\langle m | z | n \rangle|^2}{E_m - E_n} \right\} \quad (1.32)$$

In order to visualize the effect of the degeneracy, let us consider the excitation between adjacent levels with average energy gap, ΔE , for simplicity. The the dipole moment becomes

$$p \sim \frac{2e^2}{\Delta E} |\langle 1 | z | 2 \rangle|^2 E \quad (1.33)$$

and corresponding static electric polarizability α_e is obtained by using the definition $\vec{p} = \alpha_e \vec{E}$. Thus, we obtain

$$\alpha_e \sim \left(\frac{e^2}{a\Delta E} \right) a^2 \text{ with } |\langle 1|z|2\rangle|^2 \sim a^2 \quad (1.34)$$

Hence, the enhancement on the electric polarizability due to the level quantization is

$$\frac{\alpha_e}{\alpha_e^{cl}} = \frac{e^2}{a\Delta E} \quad (1.35)$$

where α_e^{cl} is the classical electric polarizability, a^3 for a metal sphere. Now, for the Kubo system, on the one hand, ΔE is the order of E_F/N_e ; therefore,

$$\frac{\alpha_e}{\alpha_e^{cl}} \sim \frac{e^2}{a} \frac{N_e}{E_F} \sim (k_F a)^2 \quad (1.36)$$

with $N_e \sim \left(\frac{a}{a_0} \right)^3$, where a_0 is the Bohr radius. Consequently, we have the enhancement which increases quadratically with the particle radius a .

On the other hand, for a highly degenerate system which has an energy gap order of $E_F/N_e^{1/3}$, the ratio of the polarizability gives

$$\frac{\alpha_e}{\alpha_e^{cl}} \sim \frac{e^2}{a} \frac{N_e^{1/3}}{E_F} \sim \frac{e^2/a_0}{E_F} \sim 1 \quad (1.37)$$

which shows no enhancement.

However, in a realistic system, the one electron picture breaks down because of screening.⁴⁵ In the classical approach, the screening effect can be included by replacing the external electric field \vec{E} by the field inside of the particle \vec{E}_{in} as in the following:

$$\vec{p} = \alpha_e \vec{E}_{in} \text{ and } \vec{E}_{in} = \vec{E} - \frac{4\pi}{3} \vec{p} \quad (1.38)$$

or

$$\alpha_{obs} = \frac{p}{E} = \alpha_e / \left(1 + \frac{4\pi}{3V} \alpha_e \right) \quad (1.39a)$$

$$= V \chi_e / \left(1 + \frac{4\pi}{3} \chi_e \right) \quad (1.39b)$$

Here α_{obs} is the observed electric polarizability, χ_e is the electric susceptibility defined by $\vec{p} = \chi_e \vec{E}_{in}$, and \vec{p} is defined as the dipole moment per unit volume. In the classical limit ($\Delta E \rightarrow 0$), α_{obs} approaches the classical value ($\alpha_e^{cl} = a^3$) which satisfies the correspondence condition.

An alternative approach to the screening can be made by considering the Coulomb interactions between electrons at different energy levels, even though the screening in a small particle is smaller than that in the bulk state. Lushnikov and Simonov⁴⁶ included the electron-electron interaction in the calculation of α_e within the Random Phase Approximation and found out that $\alpha_e / \alpha_e^{cl} \sim 1$ for a small particle at metal density. These results explain the reason for the absence of the enhancement on the observed electric polarizability.

But, there still exists a possibility of experimental observation of the effect of the energy level correlation which was first realized by Gor'kov and Eliashberg.⁷ In a recent calculation, Devaty and Sievers⁴⁷ showed that a nonquadratic frequency dependence on the FIR absorption coefficient could be regarded as the Gor'kov and Eliashberg effect. However, the magnitude of theoretical FIR absorption coefficient is still orders of magnitude smaller than the experimental results.

Kawabata and Kubo⁴⁸ used the fluctuation-dissipation theorem to calculate the optical conductivity of a small particle in visible frequency range and gave a quantum mechanical interpretation of the broadening of the surface plasmon resonance peak. Their calculation showed that the optical conductivity of a small particle was broadened significantly from the Drude conductivity.

Wood and Ashcroft⁴⁹ also carried out a calculation of the dielectric function of a small metallic cube by evaluating the momentum matrix element explicitly within the linear response theory and the random phase approximation. They obtained a similar result as Kawabata and Kubo except for a geometrical factor. However, their result failed to explain the anomalous FIR absorption.

The small particle problem can be summarized as follows:

1. The FIR absorption coefficient can be expressed as

$$\alpha = K_{\text{exp}} \nu^2$$
except for the aluminum small particle case.
2. $K_{\text{exp}} \gg K_{\text{theory}}$.

3. K_{exp} is not a function of either temperature or magnetic field.
4. K_{exp} is increased as the particle size increases.

Search for the Solution

The following questions are raised in order to understand the anomalous FIR response of the small particle system from experimental and theoretical points of view: whether the anomalous FIR absorption will be persistent to mid-infrared (MIR) frequencies or not, whether the clustering is responsible for the observed anomalous FIR absorption or not, whether there exists a possible absorption mechanism incorporated with phonons or not, and whether the choice of the Drude type dielectric function is adequate for a small particle or not.

Clustering Effects

Many efforts have been made to understand the anomalous FIR absorption by small particles. One possible candidate is clustering. Because there was no convincing direct experimental evidence on the randomness of the dispersed small particles in a medium, the effect of small particle clusters could play an important role in the FIR absorption mechanism.

Many workers⁵⁰⁻⁵³ have demonstrated that the FIR absorption can be enhanced by clustering to be close to the experimental results. This enhancement occurs because of the poor effective conductivity of individual clusters. However, in the clustering model, the quadratic frequency dependence inevitably breaks down as shown by Sen and Tanner.⁵⁴

In this work, more systematic analysis on sample characterization and FIR measurements will be made for clustered samples and presumably nonclustered samples.

Phonons

Glick and Yorke⁵⁵ suggested a possible enhanced FIR absorption in a small particle by direct coupling of external electric field to the phonon through the unscreened surface ions. The theory was able to show the temperature independence and enhanced absorption but gave a wrong particle size dependence on the absorption coefficient. Also, an effect of surface, which modifies the phonon density of states, was not included.

Another possibility is the Holstein process in a small particle, since the particle dimension is much less than the classical skin depth and electron-phonon coupling gives a frequency-dependent relaxation time in addition to the lifetime in the bulk state. For a small particle, the phonon density of states has to be modified by including the surface contribution. By solving the Weyl's boundary value problem,⁵⁶ we obtain the phonon density of states such as

$$D(\omega) = \frac{2a^3}{3\pi v_3} \omega^2 + \frac{a^2}{2v_2} \omega + O(a) \quad (1.40)$$

where

$$\frac{1}{v_3} = \frac{2}{v_t^3} + \frac{1}{v_l^3} \quad \text{and} \quad \frac{1}{v_2} = \frac{2v_t^4 - 3v_t^2 v_l^2 + 3v_l^4}{v_t^2 v_l^2 (v_l^2 - v_t^2)}$$

Here v_t and v_l are the transverse and the longitudinal sound velocity, respectively. With the modified density of states and renormalized plasma frequency, we can evaluate the electron-phonon contribution in FIR by making use of Allen's formula.⁵⁷ However, the results show a quartic dependence on frequency in the absorption coefficient,⁵⁸ which is not consistent with the observation. It is likely that the electron-phonon interaction would be less effective in a small particle because of the difficulties in energy and momentum conservation due to the quantization of electron energy and phonon frequency.

Non-Drudian Possibility

The last, conceptually rather difficult, possibility is the non-Drudian behavior. For example, the Anderson localization⁵⁹ is generally believed to occur in an electron system with impurities whose concentration is above a certain critical concentration. We can interpret the diffusionless process as a consequence of locally broken symmetry in the translational motion of electrons.

Now, for a small particle, the quantum mechanical role of the surface localizes the electrons and quantizes their kinetic energy. In fact, the finiteness of the size (or broken symmetry) imposes another important consequence; unlike the case of the electron gas in the bulk state, the momentum matrix element does not vanish. To put this idea another way, the position matrix element of an electron is always finite in such a finite system, requiring a fundamental modification to the calculation of the conductivity of a small particle.

These points will be extensively studied experimentally and theoretically in this dissertation.

In the next chapter, detailed experimental techniques will be discussed including sample preparation and characterization, instrumentation, and measurements.

In Chapter III, the experimental measurements of FIR, MIR, and visible frequency response of Al-KCl, Au-KCl, and Ag-KCl small particle composites and the interpretation of the results will be given.

A quantum mechanical theory of electrical and optical conductivity of a small particle will be presented along with the energy level correlation effect and a possible explanation for the broadening of the surface plasmon mode will be made in Chapter IV.

Finally, a summary and conclusion will be given in Chapter V.

CHAPTER II EXPERIMENT

Sample Preparation and Characterization

Small Particles

Small particles were prepared by the gas-evaporation technique.⁶⁰ As shown in Figure 2.1, small particles were deposited on the inside of a fused quartz cylinder (5-1/2" I.D. and 12" long) in the form of smoke (aggregates of small particles) by the evaporation of a metal (Al, Ag, or Au) under an inert gas atmosphere.

There are three major controllable factors which determine the size of the particle and the size distribution in this method:

1. Type of inert gas
2. Pressure of the inert gas in the vacuum chamber
3. Evaporation rate (temperature of the source)

The first and the second condition mainly determine the size of particles. The average size of particles is proportional to the pressure and the atomic mass of the inert gas used and the vapor pressure and the atomic mass of the metal. Throughout this experiment, He or Ar gas was used for Al small particles and Ar + 10% O₂ gas mixture was used for Ag and Au small particles. The purpose of the oxygen was to guarantee the electrical isolation between particles by forming an oxide layer on the surface of the particles. The background pressure before introducing the inert gas was less than 5×10^{-6} Torr. The gas pressure of the

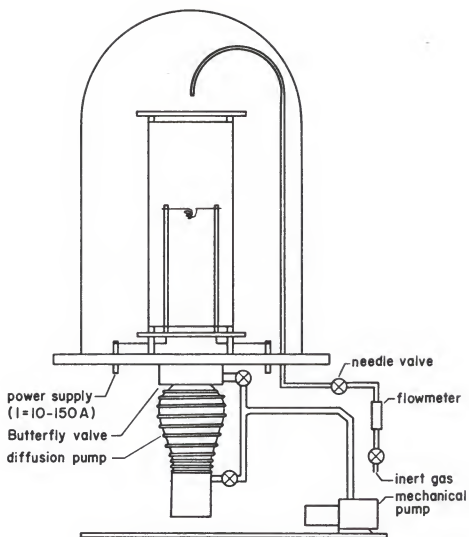


Figure 2.1 Small particle preparation apparatus

inside of the bell jar was controlled by changing the flow rate and the pumping speed. The third condition mainly contributes to the yields and the size distribution. As a heat source, several different designs of tungsten baskets were used. Among them, a basket with two tungsten wires (9.5 mm diameter) twisted together gave the best results. Also, an Alumina-coated Mo boat was tested for comparison. Typically, about 100 ~ 200 mg of pure Al (99.9999%), Ag (99.9995%), or Au (99.99%) was used to prepare small particles.

A Transmission Electron Microscope (TEM) was used to measure the particle size and the size distribution. Also, the thickness of the oxide layer could be measured in principle by comparing the bright field picture of a particle with the corresponding dark field picture to $\pm 3 \text{ \AA}$ accuracy. The typical thickness which is known to be the order of 10 \AA within the instrumental resolution (3 \AA line to line). In addition, the electron diffraction and the EDX (Energy Dispersive X-ray) spectroscopy analysis of small particles were done through the TEM. The TEM pictures of two different sizes of Al small particles are shown in Figures 2.2 and 2.3 and a result of the small particle data is given in Table 2.1. Also, the result of the oxide thickness estimation is shown in Table 2.2.

Composites

Pure KCl was used as a dielectric medium for all frequency ranges (FIR, MIR, Near-IR, and Visible) measurements. Also, paraffin was used for FIR measurements over the frequencies of the optical phonon band of KCl.

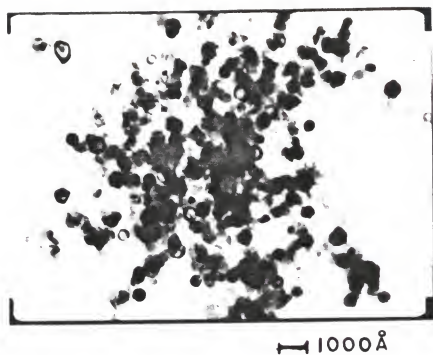


Figure 2.2 Transmission electron micrograph of Al 15 (top) and the corresponding electron diffraction pattern (bottom)

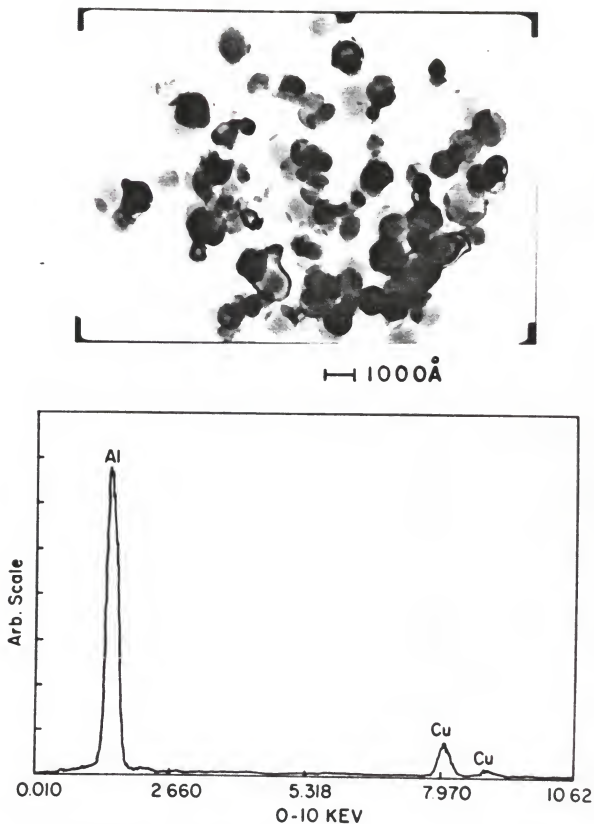


Figure 2.3 Transmission electron micrograph of Al 18 (top) and the corresponding EDX analysis (bottom) which shows no contamination by foreign atoms within the resolution (1 atomic %)

Table 2.1 Small particle parameters

Batch	Type of Gas	Pressure (Torr)	Type of Source	Current (A)	$\langle a \rangle$ (Å)	σ	Optical Measurement
A1 1	He	1.5	Type 1*	25	85	1.68	Yes
A1 2	He	1.0	Type 1*	25	94	1.34	No
A1 3	He	2.0	Type 1	20	77	1.61	No
A1 4	He	3.0	Type 1*	25	154	1.62	No
A1 5	He	1.0	Type 2	120	57	1.65	No
A1 6	He	1.0	Type 2	130	62	2.03	No
A1 7	He	3.5	Type 2	120	61	1.66	No
A1 8	He	0.5	Type 3	10	56	1.33	Yes
A1 9	He	1.5	Type 3	10	44	1.42	Yes
A1 10	He	1.5	Type 3	10	104	1.31	Yes
A1 11	Ar	0.5	Type 3	10	94	1.47	Yes
A1 12	Ar	1.0	Type 3	10	180	1.24	Yes
A1 13	Ar	2.0	Type 3	10	165	1.50	Yes
A1 14	Ar	0.5	Type 3	10	103	1.40	Yes
A1 15	Ar	1.0	Type 3	10	183	1.41	Yes
A1 16	Ar	3.0	Type 3	10	235	1.37	Yes
A1 17	Ar	5.0	Type 3	10	280	1.41	Yes
A1 18	Ar	10.0	Type 3	10	399	1.43	Yes

Table 2.1—Continued

Batch	Type of Gas	Pressure (Torr)	Type of Source	Current (A)	$\langle a \rangle$ (Å)	σ	Optical Measurement
Ag 1	Ar+10% O ₂	1.0	Type 3	20	52	1.42	Yes
Ag 2	Ar+10% O ₂	5.0	Type 3	20	250	1.93	Yes
Au 1	Ar+10% O ₂	1.0	Type 3	10	152	1.72	Yes
Au 2	Ar+10% O ₂	5.0	Type 3	10	150	1.86	Yes

Note: σ : geometrical standard deviation

Type 1*: 0.03" diameter W wire spiral

Type 1: 0.5 mm diameter W wire spiral

Type 2: Al₂O₃ coated Mo boat

Type 3: W basket made with two 0.5 mm diameter wires twisted together

Table 2.2 Analysis of the oxide layer

Aluminum	Particle radius in bright field $r_B(\text{\AA})$	Particle radius in dark field $r_D(\text{\AA})$	Oxide thickness $t(\text{\AA}) \pm 3\text{\AA}$ ($t = r_B - r_D$)
Al 1	100	85	15
	135	120	15
	80	65	15
Al 9	85	75	10
	95	85	10
	50	40	10
	50	40	10
Al 13	115	100	15
	70	55	15
	130	115	15

The bulk KCl or paraffin was ground up to $1\text{ }\mu$ size grains in a Freezer Mill operating at 77°K and then the dried KCl powder (dried at 150°C for 3 ~ 5 hours under vacuum) or paraffin (dried under vacuum at room temperature) was mixed with small particles. The volume fraction (f) was estimated by (to the first order)

$$f = \left(\frac{\rho_h}{\rho_m} \right) \frac{W_m}{W_h} \quad (2.1)$$

where ρ_m (ρ_h) is the density of metal (host medium) and W_m (W_h) is the weight of metal (host medium). The mixture was mixed in a Freezer Mill and then pressed in an evacuated die into a $5/8$ " diameter pellet. The compression took place at about 130,000 psi for KCl and at 3,200 psi for paraffin. The composite pellet was reground several times until a satisfactory homogeneity was achieved. Normally four times of regrinding was enough for low volume fraction samples ($f \leq 0.008$). For the visible frequency measurements, the samples were diluted ten times from $f = 0.001$ samples to have enough transmission of light. The pressure-regrinding process was repeated four times for these diluted samples. The thickness of the sample ranged from 0.18 mm to 5.0 mm, depending on the volume fraction and the frequency ranges covered.

Samples, for two different Al particle sizes which were believed to have large clusters of small particles, were deliberately prepared without using the Freezer Mill in order to study the effect of clustering.

A correction of the volume fraction is necessary to estimate the true metal volume fraction because each metal particle has about 10 Å thick oxide coating. In actual calculation, the following correction can be made to the apparent volume fraction

$$f' = \left(\frac{a - t}{a} \right)^3 f \quad (2.2)$$

where f' is the corrected volume fraction, a is the particle radius, and t is the thickness of the oxide coating.

Also, in order to get rid of the interference fringes in the FIR transmission measurement due to the multiple internal reflection between front and back surfaces of a sample, one series of samples had an extra layer of KCl added to make the total thickness of the sample larger than about 5 mm. Under the assumption that the difference between the static dielectric constants of the small particle-KCl composite and of the pure KCl layer is negligible, the FIR beam will not distinguish the boundary.

Sample Characterization

A TEM or an optical microscope was used to characterize the randomness of small particle distribution in a composite. For the TEM study, very thin sections of a sample were made by using either an ion mill or a chemical polisher. In order to mill down a sample through the ion mill, a sample was cut into 3 mm diameter pellets and ground down to 100 μ thickness and dimpled until the thickness of the thinnest portion became about 10 μ . Then, the ion mill was used to make a pinhole

on the specimen. The TEM pictures were taken in the vicinity of the pinhole where the electrons can be transmitted.

Another effective method was attempted by using a chemical polisher. Since water dissolves KCl, a 90% alcohol and 10% distilled water mixture was used as a chemical solution. A 3 mm diameter sample was sandwiched between two jet streams of alcohol-water mixture and polished down until a pinhole was made.

It took about 3-5 minutes to prepare a sample with the chemical polishing method in contrast to 5-10 hours in the ion milling method.

The prepared sample was placed on a cold stage operating normally at -100°C to prevent the melting of the sample when the electron beam was condensed on a particular area, and the sample stage was mounted in the TEM. About 10-15 different areas were examined for each sample and the results are shown in Figures 2.4, 2.5, and 2.6. Individual particles can be seen clearly in the TEM pictures. Especially because the typical thickness of the area examined is about $1,000 \text{ \AA}$, the composite is surprisingly close to the truly random system with well separated individual particles for samples made with Al 14 (103 \AA) particles.

In addition, an optical microscope and TEM study was done on the clustered samples which were mixed without using the Freezer Mill to see the size and the distribution of clusters as shown in Figures 2.7 and 2.8.

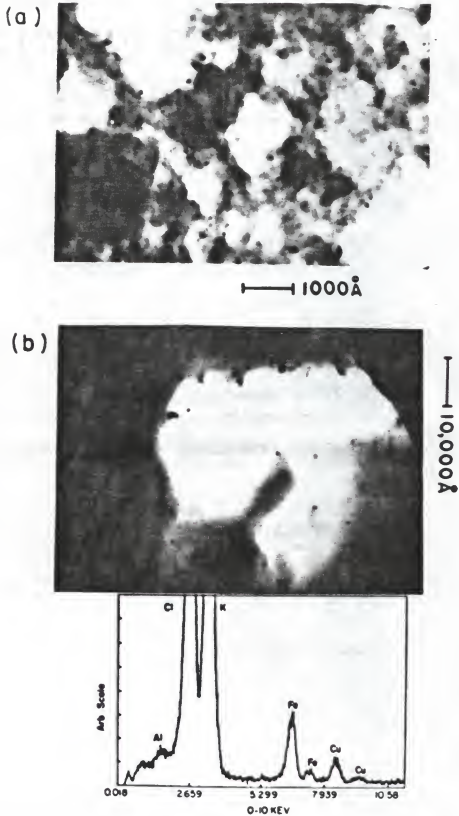
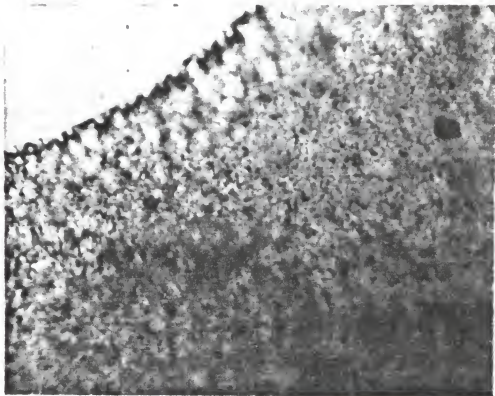


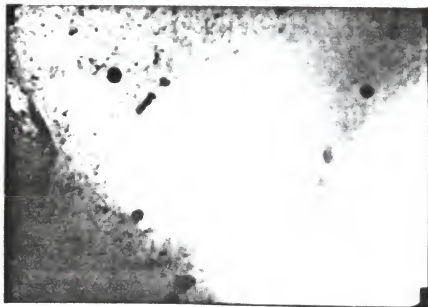
Figure 2.4 Transmission electron micrographs of Al-KCl composites (a) Water polished $f = 0.032$ Al 1- KCl composite plate (# of regrinding = b) and (b) ion milled $f = 0.001$ Al 18-KCl composite plate with EDX result which shows some Fe contamination (circled area) during the sample manufacturing process (% of regrinding = 4)

(a)



— 2 μ

(b)



— 2000 \AA

Figure 2.5 Optical and transmission electron micrographs of $f = 0.001$ Al 18 - KCl composite (# of regrinding = 4)
 (a) Optical micrograph of chemically polished plate and
 (b) transmission electron micrograph of ion milled plate

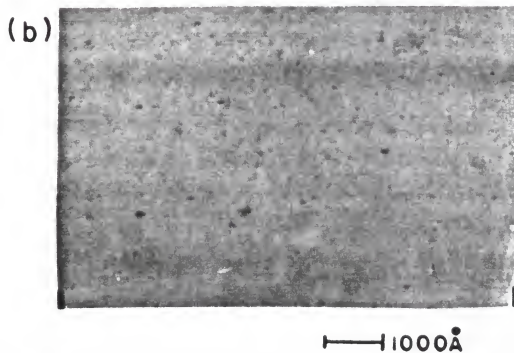
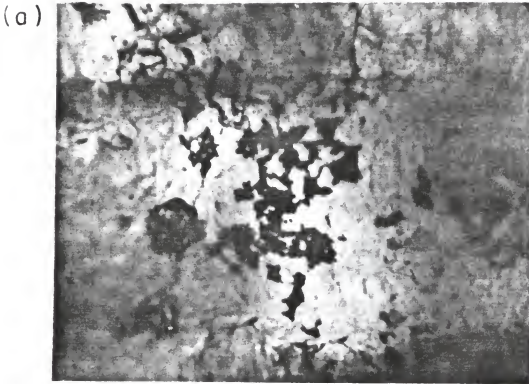
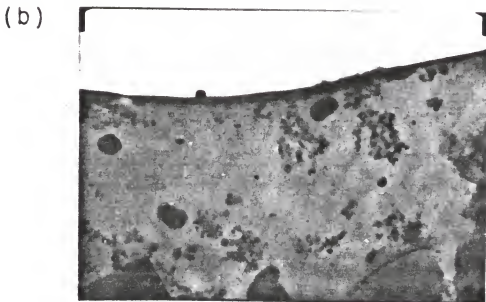


Figure 2.6 Transmission electron micrographs of Al 14-KCl composite ($f = 0.001$, ground 4 times)
(a) Ion milled and (b) chemically polished plate



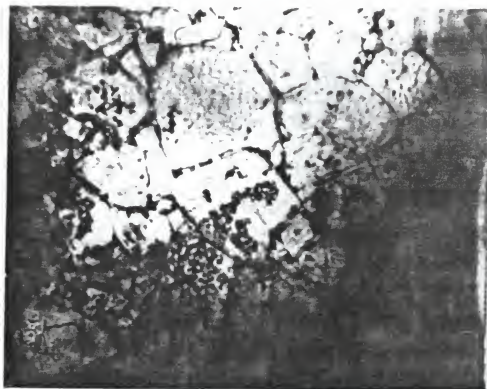
— 2 μ



— 1 μ

Figure 2.7 Optical and transmission electron micrographs of Al 18-KCl composite ($f = 0.001$, mixed by hand)
(a) Optical microscope result and (b) TEM result

(a)


 $\text{—} 2\mu$

(b)

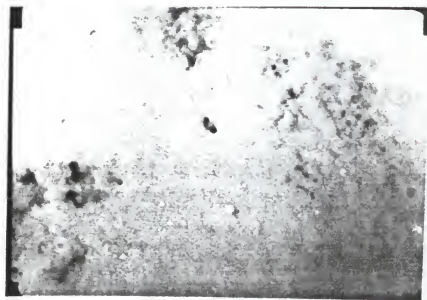

 $\text{—} 1000\text{\AA}$

Figure 2.8 Optical and transmission electron micrographs of Al 14-KCl composite (mixed by hand)
 (a) Optical microscope result ($f = 0.002$) and (b) TEM result ($f = 0.001$)

Infrared and Optical Technique

Fourier Transform Spectroscopy

Interference of light from two mutually coherent sources is a well-known phenomenon. As illustrated in Figure 2.9(a), the intensity I at D can be written as the time average of the square modulus of the sum of two amplitudes $A_1(t)$ and $A_2(t + \tau)$, which correspond to the amplitude from slit 1 and slit 2, respectively.

$$\begin{aligned} I &= \langle [A_1(t) + A_2(t + \tau)][A_1(t) + A_2(t + \tau)]^* \rangle \\ &= I_1 + I_2 + 2\text{Re} \langle A_1(t) A_2^*(t + \tau) \rangle \end{aligned} \quad (2.3)$$

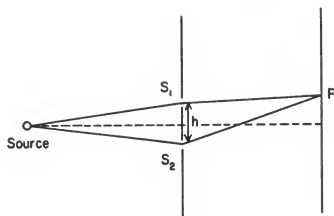
where $I_1 = \langle |A_1(t)|^2 \rangle$, $I_2 = \langle |A_2(t + \tau)|^2 \rangle$, and the angular bracket represents the time average. I_1 (I_2) is the intensity of light through S_1 (S_2) only. The last term in Equation (2.3) contains all interference effects because of the temporal correlation between two amplitudes caused by τ . When $\tau \rightarrow \infty$ (i.e., $h \rightarrow \infty$), there is no correlation. Therefore,

$$I \equiv I_\infty = I_1 + I_2 \quad (2.4)$$

Now, if we can manage to give the time difference τ between two light beams in the limit of $h \rightarrow 0$, then $|A_1| = |A_2|$ by ignoring the fluctuation in the amplitude. Hence,

$$I = I_\infty + 2\text{Re} \langle A(t) A^*(t + \tau) \rangle \quad (2.5)$$

(a)



(b)

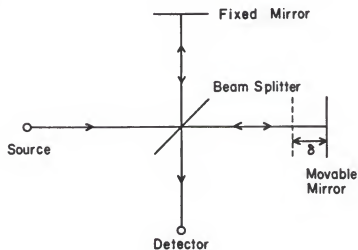


Figure 2.9 Two different illustrations of obtaining interference
 (a) Double slit and (b) Michelson interferometer

where the subscripts 1 and 2 have been deleted. The function $\langle A(t) A^*(t + \tau) \rangle$ is called as the autocorrelation function; it satisfies the Wiener-Khinchine theorem.⁶¹ That is,

$$\langle A(t) A^*(t + \tau) \rangle = \text{FT} [|A(v)|^2] \quad (2.6)$$

where FT represents the Fourier transformation and v represents frequency. As shown in Figure 2.9(b), the Michelson interferometer is a perfect example of what can be described by Equation (2.5). By changing from the time domain to a spatial coordinate, such as $\delta = c\tau$ where δ is the path difference between the two mirrors, and defining the correlation function $\Gamma(\delta)$ as

$$\Gamma(\delta) = 2 \text{Re} \langle A(0) A^*(\delta) \rangle \quad (2.7)$$

we can rewrite expression (2.5) as

$$I(\delta) = I_\infty + \Gamma(\delta) \quad (2.8)$$

Again, $\Gamma(\delta)$ satisfies the Wiener-Khinchine theorem. Therefore, the power spectrum can be obtained by an inverse Fourier transform of the $\Gamma(\delta)$:

$$S(v) = \int_{-\infty}^{\infty} \Gamma(\delta) e^{2\pi i v \delta} d\delta \quad (2.9)$$

where $v = \frac{\omega}{2\pi c}$ and $S(v) = |A(v)|^2$. Now, when $\delta = 0$, $I_0 = 2I_\infty$; therefore, we can rewrite Equation (2.9) in the desired form

$$S(\nu) = \int_{-\infty}^{\infty} (I(\delta) - \frac{1}{2} I_0) e^{2\pi i \nu \delta} d\delta \quad (2.10)$$

$I(\delta)$ is the measured quantity in the experiment.

In actual measurements apodization is necessary to remove the difficulty arising from finite maximum path difference. Proper filtering is also essential to overcome the aliasing problem due to discrete sampling by removing the frequencies higher than the maximum cut-off frequency determined by the sampling interval.⁶²

Optical Spectroscopy

As the frequency range of interest increases towards the higher frequency region, the Fellgett advantage⁶³ which counts for the thermal detector noise only in the infrared loses its importance due to the increasing photon noise in the radiation field. Therefore, a monochromator is normally used to avoid many difficulties in Fourier transform spectroscopy in the Near-IR and visible frequency range. But, the photon noise also eventually limits the performance of the monochromator at very high frequencies.

Generally, a grating monochromator is used by applying the rule of diffraction. For a wave length λ ,

$$\nu = \frac{n}{2d} \frac{1}{\sin\theta} \quad (2.11)$$

where n is the integer order, d is the grating constant (cm/line), θ is the angle of the grating measured from the position for normal incidence

of the light. The resolution is determined by the slit width and $\Delta\theta$, which is the angle of rotation at each step.

Instrumentation

Michelson Interferometer

In the FIR region, the Fellgett advantage is obtained from the signal-to-noise ratio argument and Fourier transform spectroscopy maximizes the efficiency of the experiment.

To measure the spectrum in the 10 to 800 cm^{-1} region, a Michelson interferometer⁶⁴ was used. Correct combination of the thickness of a Mylar beam splitter, filters, and the sampling step size is important to remove the aliasing problem. As shown in Figure 2.10, the entire instrument is placed inside a vacuum tank to prevent FIR absorption due to water vapor in the air.

Lamellar Grating Interferometer

A lamellar grating interferometer⁶⁵ was used to cover the frequency range from 2 cm^{-1} to 60 cm^{-1} . In principle, this instrument works in the same way as the Michelson type interferometer, but has better modulation than that of the Michelson interferometer, which has poor beam splitter efficiency in the very FIR. A detailed instrumental set-up is shown in Figure 2.11.

Grating Monochromator

A Perkin-Elmer model grating monochromator was used (Figure 2.12) to cover from MIR to ultra-violet frequency. As described in the optical spectroscopy section, each single frequency is selected by using

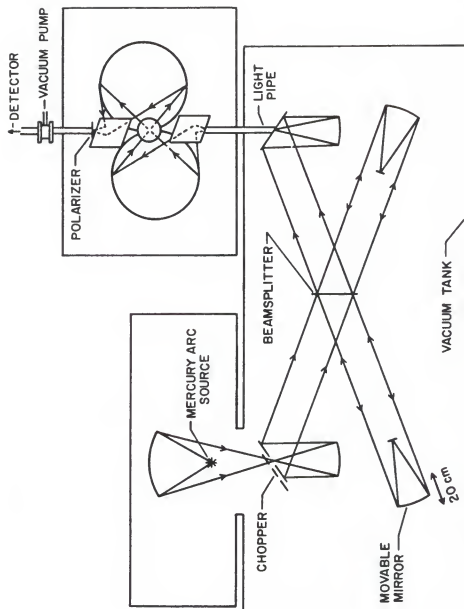
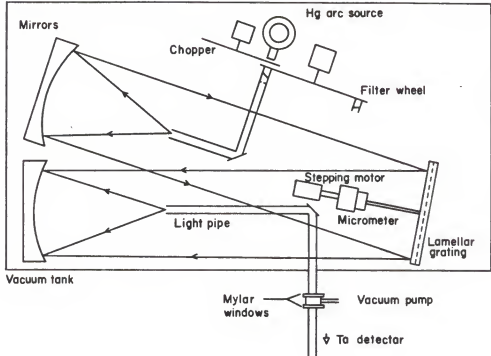


Figure 2.10 Schematic diagram of Michelson interferometer

(a)



(b)

Cross sectional view of Lamellar Grating

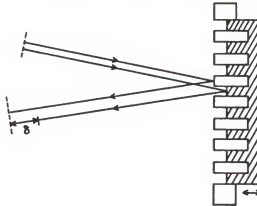


Figure 2.11 Lamellar grating interferometer (a) and cross sectional of the lamellar grating to show the optical path difference (b)

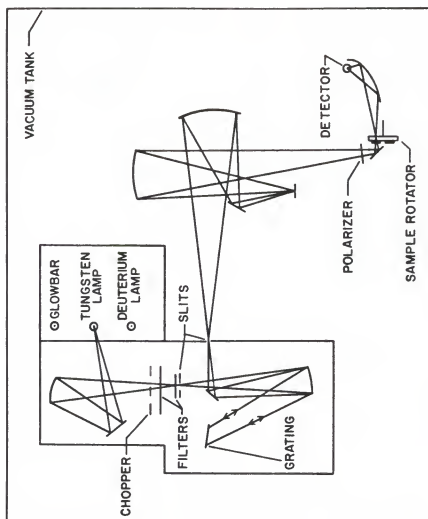


Figure 2.12 Schematic diagram of grating monochromator

the grating, filter, and the matching source. A more detailed source of information about the operation of this instrument is found in the work by Cummings.⁶⁶

Measurement

Source and Detector

A mercury arc lamp was used as a FIR source, and the source was chopped to remove all background radiation. A doped germanium bolometer operating at 1.2°K served as a FIR detector. Figure 2.13 shows a diagram of the cryostat.

In order to detect the FIR signal from the instrument, a 1/2" I.D. brass tube was used to guide the radiation through the cryostat.

For higher frequency measurements, three different types of detectors for three different matching sources were used with the Perkin-Elmer grating monochromator. Table 2.3 shows a summary of the combination of instrument, source, detector, and frequency range used in this work.

Data Acquisition

The FIR signal was detected by a bolometer, which was biased from the external DC voltage source. The voltage change across the detector due to the change of the resistance in response to the incoming radiation was fed into a lock-in amplifier (Ithaco 393). The amplified signal was sent to a chart recorder and a digital voltmeter (DVM). The signal was averaged by the DVM (Fluke) for a given time interval (typically, 1 to 5 seconds, which depends on the signal-to-noise

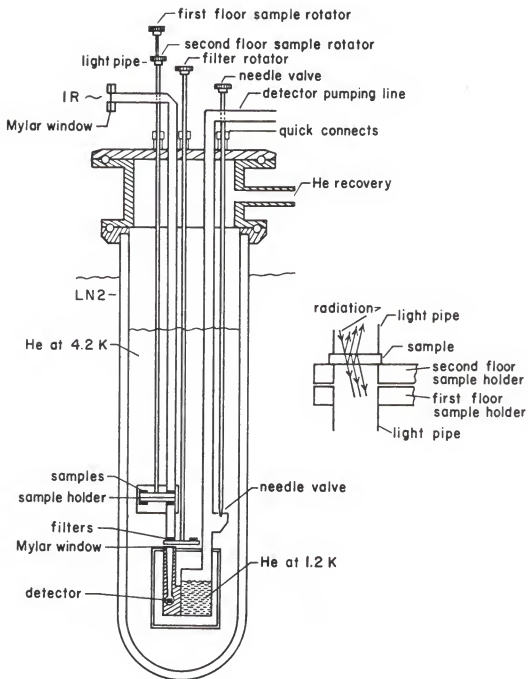


Figure 2.13 Schematic diagram of detector cryostat

Table 2.3 Summary

Frequency (cm^{-1})	Source	Detector	Instrument
2-60	Mercury arc lamp	Bolometer	Lamellar grating interferometer
10-800	Mercury arc lamp	Bolometer	Michelson interferometer
690-4,400	Globar	Thermocouple	Perkin-Elmer monochromator
4,400-15,400	Tungsten lamp	PbS	Perkin-Elmer monochromator
14,600-27,000	Tungsten lamp	Photomultiplier	Perkin-Elmer monochromator
26,000-47,000	D ₂ lamp	Photomultiplier	Perkin-Elmer monochromator

condition). And then, the digitized information by the DVM was stored in a PDP 11/23 computer. After having taken a point, the computer sent a signal to the stepping motor controller to advance to the next step. This process was repeated until the desired number of data points had been taken. The stored data were analyzed through the Fast Fourier Transform programs after having finished the data acquisition.

For the grating monochromator, the spectrum was directly acquired from the detector used and the same procedure as in the FIR measurement case was repeated until a whole spectrum range was covered. The spectrum was normalized and analyzed through the computer.

CHAPTER III RESULTS

The electromagnetic response of the small particle composites were analyzed from transmission measurements, with the absorption coefficient given by

$$\alpha(\omega) = -\frac{1}{d} \ln T(\omega) + \frac{2}{d} \ln [1 - R(\omega)] \quad (3.1)$$

here $\alpha(\omega)$ is the absorption coefficient at frequency ω , d is the thickness of the sample, $T(\omega)$ is the measured transmission, and $R(\omega)$ is the reflectance of the sample. Typically, the reflectance of a composite sample ($f \leq 0.03$) is close to that of pure KCl and essentially frequency independent. Therefore, the reflectance of pure KCl was used in the data analysis.

FIR Data

Absorption Coefficient

Figure 3.1 shows a result of the FIR measurements on small aluminum particle-KCl composites. The data can be shown to fit the following formula:

$$\alpha_{\text{exp}}(\nu) = \kappa_{\text{exp}} f \nu^2 + \alpha_0 \quad (3.2)$$

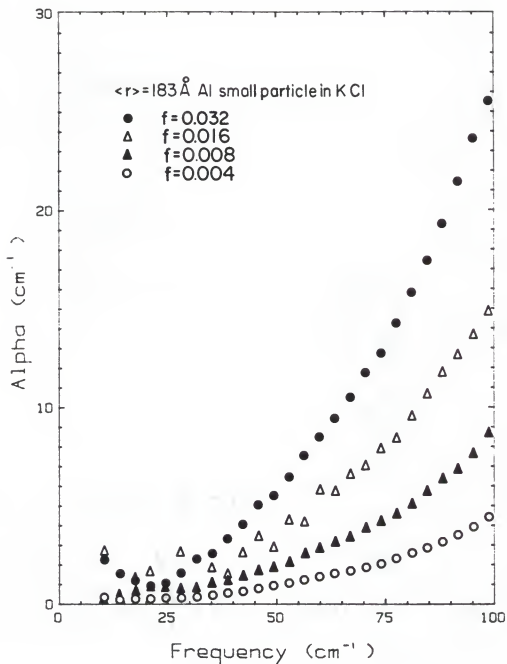


Figure 3.1 FIR absorption coefficients of Al (Al 15)-KCl composites

where α_0 is the correction for the reflection and the detector nonlinearity. The proportionality constant K_{exp} can be a function of a number of variables; for example,

$$K_{\text{exp}} = K(\epsilon_m, \epsilon_0, a, f) \quad (3.3)$$

where $\epsilon_m(\epsilon_0)$ is the dielectric constant of the metal (surrounding medium), a is the radius of the particle, and f is the volume fraction.

As shown in Figure 3.2, the ν^2 dependence is quite obvious in the α_{exp} versus ν^2 plot. In this particular measurement, an extra KCl layer was used to remove interference effects, as described earlier. One remark on these data is that the volume fraction dependence of the absorption coefficient is close to linear in f in contrast to the previous work done by Carr et al.¹⁷ In other words, K_{exp} is not a function of f . The f^2 dependence in the previous results could be attributed to the effect of interparticle tunneling due to the clustering of particles.

Another experimental characteristic of the FIR absorption by small particles is that there is no clear distinction among different types of metals which suggests that the FIR absorption mechanism is governed by electrons. For example, some results of the FIR measurements on Ag and Au small particles show about the same order in magnitude of absorption as that of the similar size aluminum particles and also show the quadratic frequency dependence of the absorption coefficient as shown in Figure 3.3.

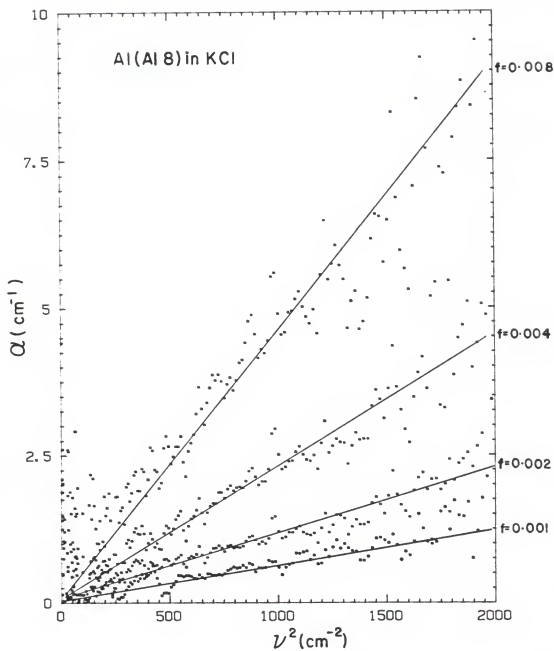


Figure 3.2 α_{exp} vs. ν^2 plot of FIR absorption coefficient of AL (Al 18)-KCl composites

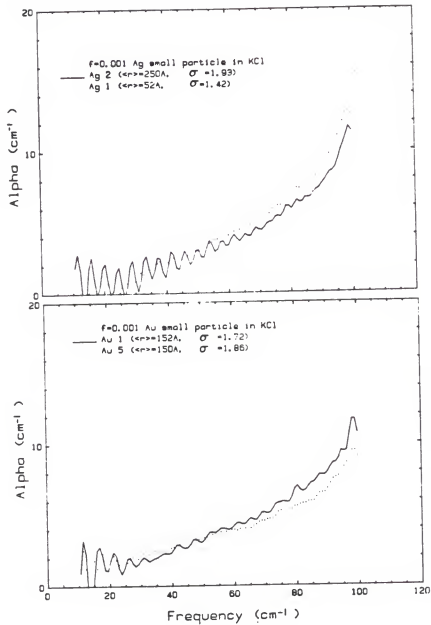


Figure 3.3 FIR absorption coefficient of Ag-KCl and Au-KCl composites (note that the interference fringes are arising from the multiple reflection)

A comparison of the experimental absorption coefficient with the result of the corresponding classical theory is made in Figure 3.4. The persistent anomalous FIR absorption, which does not agree with the absorption described by the classical small particle model can be clearly seen in this plot.

The particle size dependence on the FIR absorption strength, K_{exp} , in Figure 3.5 shows a difference to the theory which suggests that the intrinsic electrical properties of a small particle could be different from what we have believed to be correct (e.g., the concept of small "Drude metal" particle and the surface scattering rate approximation, etc.). Also, as shown in Figure 3.6, a correction due to the oxide coating on small particles was made on K_{exp} under the assumption that the core metal part of particles is solely responsible for the anomalous FIR absorption by calculating the true volume fraction such as

$$K'_{\text{exp}} = \left(\frac{a}{a - t} \right)^3 K_{\text{exp}} \quad (3.4)$$

where a is the particle radius and t is the thickness of the oxide coating, here assumed to be 10 \AA .

Clustering Effect-FIR

One conjecture made to resolve the FIR problem attributes it to clustering of the individual particles, because there was no clear experimental verification of randomness. This clustering theory does

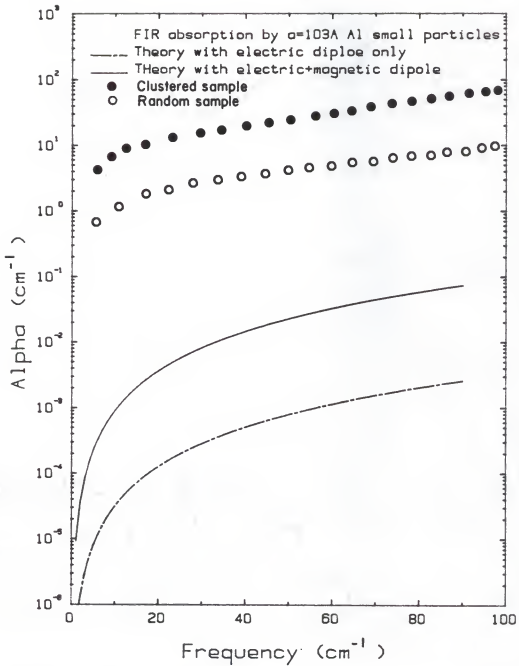


Figure 3.4 A comparison of an experimental result to the result of classical calculation

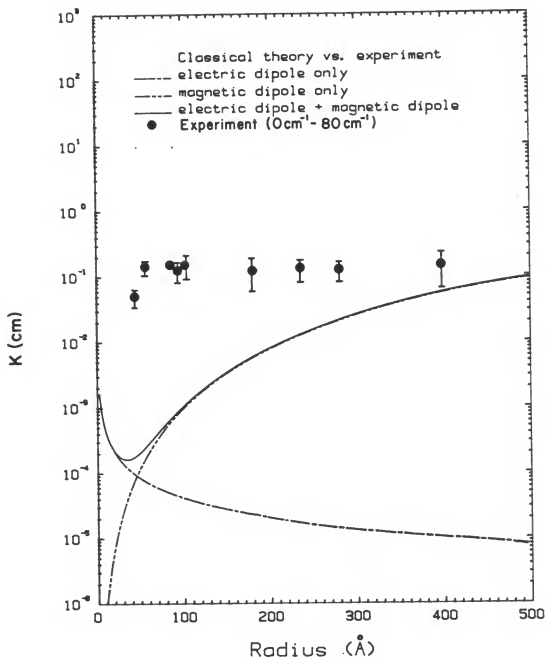


Figure 3.5 K_{exp} in cm vs. particle size plot along with the theoretical calculation of K_e (electric dipole) and K_m (magnetic dipole)

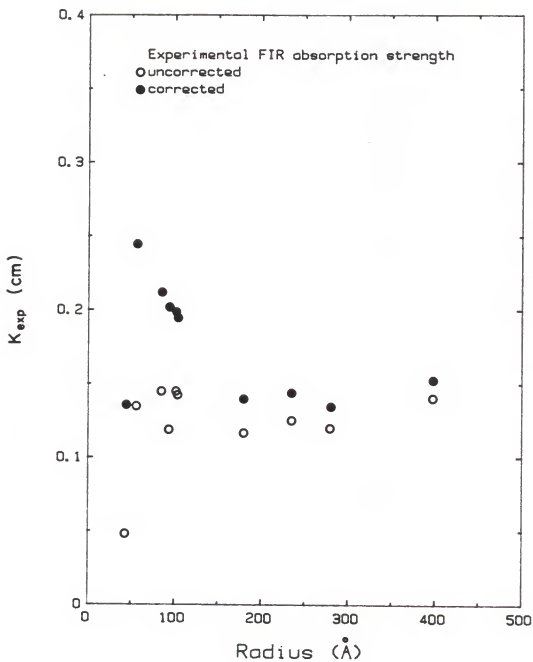


Figure 3.6 K'_{exp} (closed circle) vs. particle size plot; also, K_{exp} (open circle) is shown

show as much enhanced FIR absorption, which mainly results from the poor effective conductivity of clusters (order of micron size) as compared to a metallic particle.

From the experimental point of view, two tests of the mixing and grinding effect on the small particle-insulator composites can be done: first, directly by TEM analysis, and, second, by the FIR and MIR measurements on these samples. As shown in Chapter II, the results of the TEM analysis showed no clustering in carefully prepared composites and showed a clear difference between the random and the clustered samples. The effect on the FIR absorption of successive regrinding by the "freezer mill" is shown in Figure 3.7. The absorption coefficient of sample mixed by hand also is shown in Figure 3.7. The FIR absorption strength, K_{exp} , decreases significantly after first regrinding by the "freezer mill." However, the grinding effect shown in Figure 3.7 demonstrates a tendency of increasing K_{exp} , which saturates beyond a certain number of grindings as the number of grindings by the freezer mill increases, which could be due to a possible contamination by foreign materials during the regrinding process.

By judging from the TEM analysis and the FIR measurement, clustering is definitely not the major cause of the anomalous FIR absorption and the sample mixed by hand which contains micron-size clusters or larger did show an enhanced absorption. Therefore, the anomalous FIR absorption is indeed the small particle phenomenon.

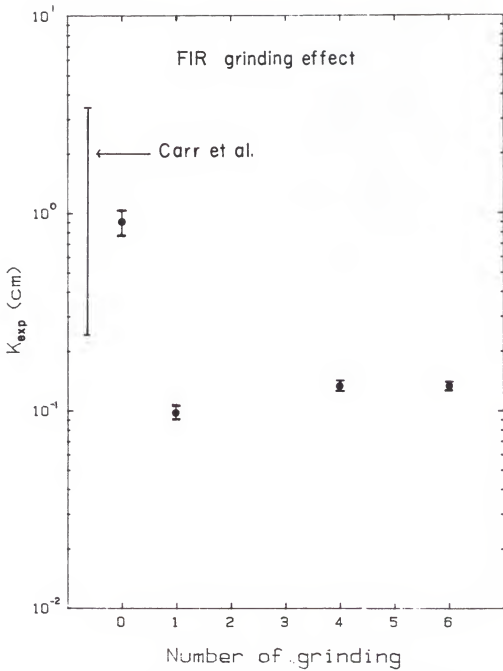


Figure 3.7 Grinding effect on FIR absorption of Al-KCl composites; the arrow indicates the result of Carr et al.¹⁷

Scaling Behavior in $\epsilon_1(0)$

As a byproduct, the information about the enhancement of the static dielectric constant of composites can be analyzed from interference fringes due to multiple internal reflections. This analysis is most easily done by Fourier transforming corrected (for the base line, $K_{\text{exp}} f v^2$) the absorption coefficient. This transform shows a maximum located at $x = 2nd$ (n = index of refraction and d = thickness of sample). An example calculation is shown in Figure 3.8. The curve has a Lorentzian shape because the interference fringes decays exponentially as the frequency increased due to absorption. The volume fraction dependent behavior of $\epsilon_1(0)$ is shown in Figure 3.9. The enhancement in $\epsilon_1(0)$ with increasing small particle concentration agrees with the results of Grannan et al.,⁴² described in Chapter I.

MIR Data

Absorption Coefficient

A dramatic and unexpected change in the absorption coefficient was observed as the frequency increased above the FIR frequency. As shown in Figure 3.10, there is a sudden decrease in the absorption coefficient near $1,000 \text{ cm}^{-1}$, after which the absorption increases quadratically again as the frequency continues to increase. However, the MIR absorption strength, K_{exp} , is much smaller than K_{exp} in the FIR region. The MIR data were fitted to

$$\alpha_{\text{exp}} = K_{\text{exp}} f v^2 \quad (3.5)$$

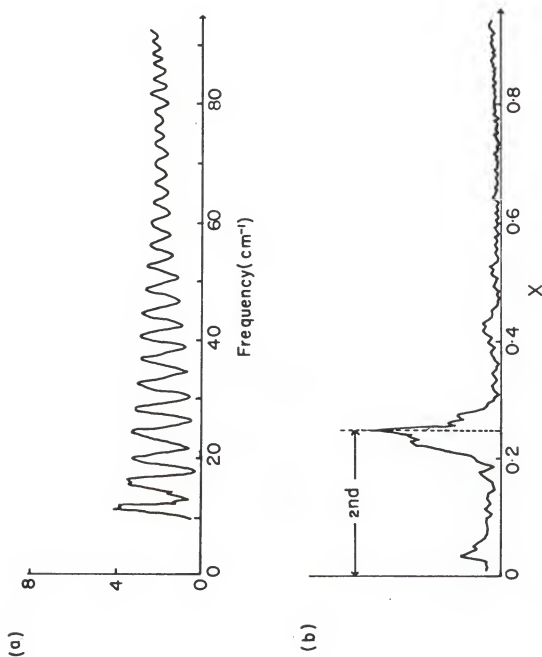
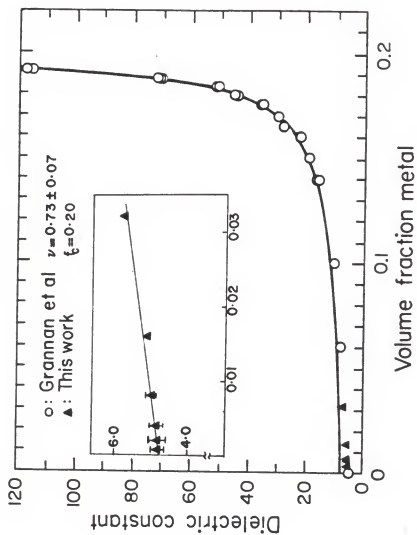


Figure 3.8 An example of obtaining the index of refraction by Fourier transform technique
 (a) Base line corrected absorption coefficient of $f = 0.016$ Al 1-KCl composite
 ($d = 0.055$ cm) and (b) Fourier transformed result of (a)

Figure 3.9 Scaling behavior of $\epsilon_1(0)$

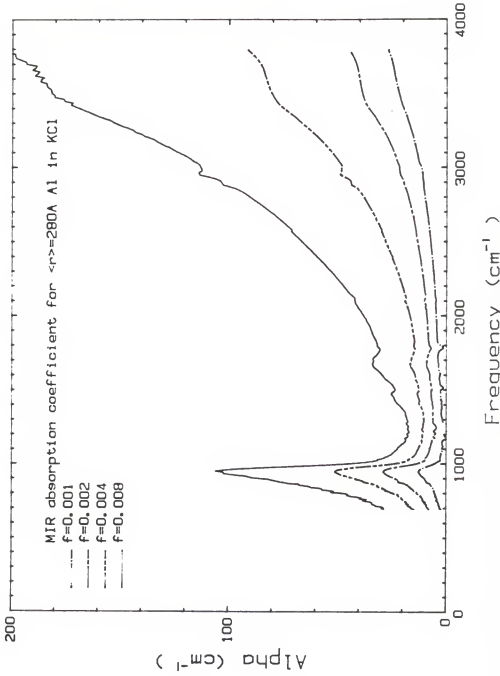


Figure 3.10 MIR absorption coefficients of Al-KCl composites

The measured K_{exp} in the MIR range is plotted in Figure 3.11 versus particle size. There are some variations in K_{exp} as the size changes, but it is quite different from the result predicted by the classical model calculation.

Note that the classical theory given in Chapter I explains K_{exp} in magnitude if we use a sufficiently short electron mean free path, $\lambda = v_F \tau$, in the Drude dielectric function. A fit with $\lambda = 1 \text{ \AA}$ ($\tau = 4.95 \times 10^{-17} \text{ sec}$) is also shown in Figure 3.11 as the solid curve. The satisfactory results with an unphysical parameter (1 \AA mean free path) are rather surprising and stimulates the speculation about the non-Drudian possibilities of the electron behavior in a small particle.

The MIR absorption data of the Au and Ag small particles are shown in Figure 3.12. There are noticeable differences in the MIR behavior of Ag and Au particles from that of aluminum: The MIR absorption coefficients of Ag and Au samples do not seem to follow Equation (3.5) and, in addition, there are many narrow structures not seen in aluminum small particles. Since most metal oxides have a series of optical phonon modes in the frequency range between 300 cm^{-1} and $1,000 \text{ cm}^{-1}$ and the small particles always have the oxide coating on their surface which was introduced for the electrical isolation between the particles, there should exist the optical phonon contribution of the oxide in the absorption mechanism in the given frequency range.

Oxide Contribution

The effective dielectric function, ϵ_p , of a small particle constituted of a metallic core surrounded by an oxide coating can be written as

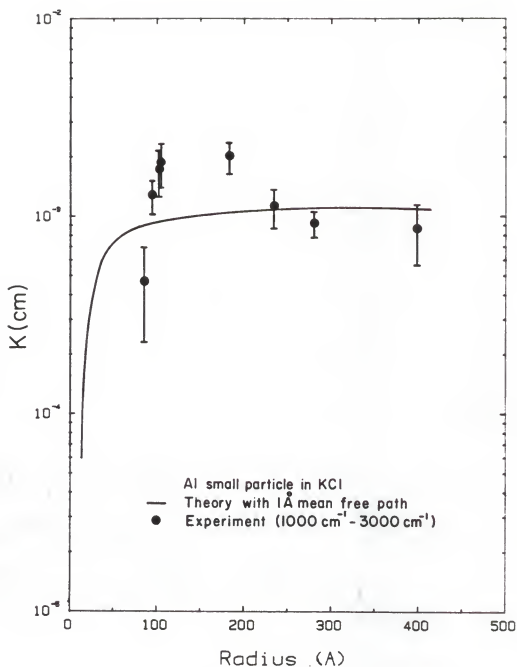


Figure 3.11 K_{exp} in MIR frequency vs. particle size; the classical calculation with $\tau = 4.95 \times 10^{-17}$ sec is shown as the solid line

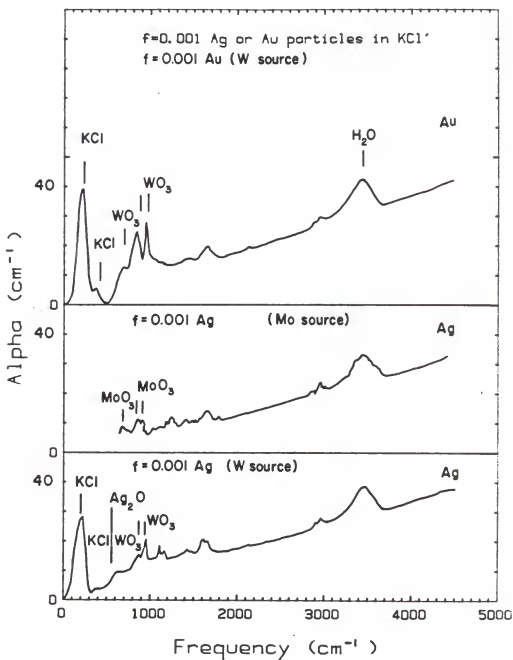


Figure 3.12 MIR absorption coefficients of Au-KCl and Ag-KCl composites

$$\epsilon_p = \epsilon_{ox} \frac{3\epsilon_m - 2\xi(\epsilon_m - \epsilon_{ox})}{3\epsilon_{ox} + \xi(\epsilon_m - \epsilon_{ox})} \quad (3.6)$$

where ϵ_{ox} is the dielectric function of the oxide coating and

$$\xi = 1 - \left(\frac{a-t}{a} \right)^3.$$

Here t is the oxide thickness and a is the radius of the particle (metal plus oxide).

In the case of the aluminum oxide, the parameters for ϵ_{ox} (resonance frequency and oscillator strength for each mode) were chosen from the work done by Barker.⁶⁷ But the linewidth has to be increased by a factor of 100 to match the magnitude of the broad absorption. Even so, as shown in Figure 3.13, the fit to the experimental observation by using the parameters and Equation (3.6) gives a location for the peak in the calculated plot which does not match the observed peak. Also, an experimental ϵ_{ox} for evaporated aluminum oxide (AlO_x) obtained by Eriksson et al.⁶⁸ was used for comparison and the result is shown in Figure 3.13. A fairly good agreement (the fit is about 30 cm^{-1} red shifted) with the experimental data was obtained, which supports the electron diffraction result that the oxide coating is in an amorphous form rather than a crystalline form. However, as shown in the small insert in Figure 3.13, the high-resolution experimental data shows some weak individual phonon peaks of aluminum oxide with their natural width. This observation suggests that the oxide coating consists of amorphous aluminum oxide with small fraction of crystalline aluminum oxide.

Another possible candidate is tungsten oxide, which has the higher longitudinal mode than the aluminum oxide. However, EDX Analysis

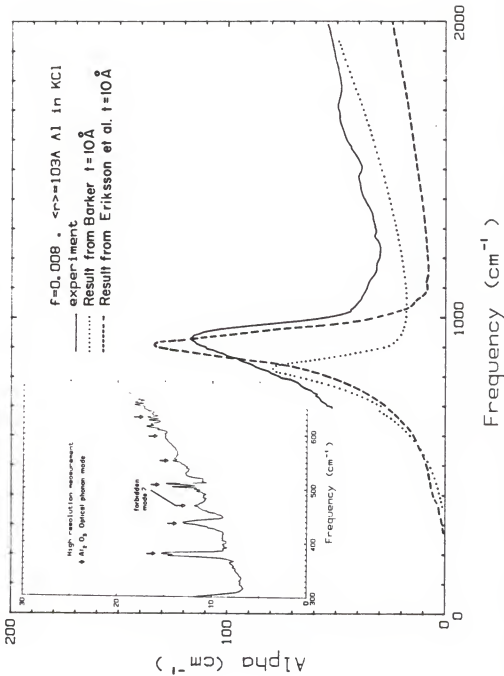


Figure 3.13 A theory fit (dashed curve) to MIR data by using parameters given in Reference 67 and a data fit (dotted curve) with experimental value obtained in Reference 68; the small insert shows a result of high resolution measurement

shows no direct evidence of the tungsten contamination in Al small particles (see Figure 2.5). Also, because no oxygen gas was introduced during the aluminum evaporation process, there will be minimal oxidation of the tungsten filament at the 5.0×10^{-6} Torr background pressure in the bell jar.

As shown in Figure 3.12, there are many different types of oxide contributions to the absorption coefficient of Ag and Au composites. For these metals, because evaporation took place in approximately 10% oxygen and 90% of Ar inert gas mixture, O_2 also oxidized the source material (either Mo or W). Thus, we have small Ag or Au particles with an oxide coating combined with WO_3 or MoO_3 . A TEM view of these samples is shown with the corresponding EDX analysis in Figure 3.14. Therefore, the broad absorption in the frequency range between 300 cm^{-1} and $1,000\text{ cm}^{-1}$ is mainly due to optical phonons in the amorphous oxide coating and the absorption characteristic depends on the type of metal.

One remark on Ag and Au small particle data is that because now the Ag (Au) smokes are the mixture of Ag (Au) particles with oxide coating and the source material oxide, the actual metal volume fraction was always smaller than that of the calculation when the composite was prepared. This point will be clear in the Maxwell-Garnett resonance data.

Another remark is the nonquadratic behavior in the MIR absorption coefficient of Ag (Au) particles could be due to some finite (but low) dc conductivity of Ag (Au) oxide as will be discussed in Appendix E.

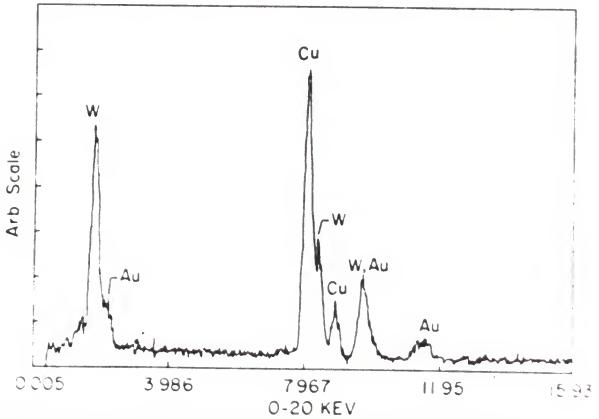
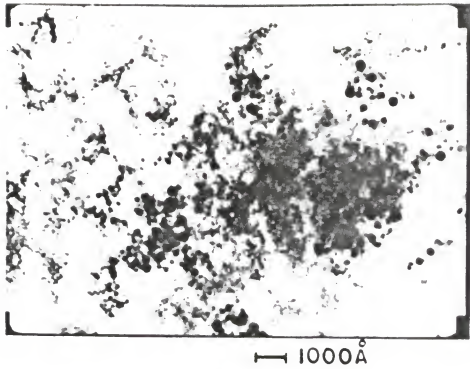


Figure 3.14 A TEM result of Au small particles with EDX analysis; note that the size distribution is very broad

Grinding Effect-MIR

The evolution of the MIR absorption coefficient with successive regrindings of the random composite samples is shown in Figure 3.15. An effect of grinding on the MIR absorption coefficient was evident unlike the FIR case. The MIR absorption data shown in Figure 3.15(a) are for samples mixed by hand. Two distinct characteristics can be noticed: One is that the frequency dependence on the MIR absorption coefficient is not quadratic any more even though the FIR tail still is quadratic. The other is that the absorption coefficient is not linear in the volume fraction at all. The nonquadratic dependence (rather square root dependence) on the MIR absorption coefficients can be explained by the resistor-capacitor model worked out by Sen and Tanner.⁵⁴ In Figure 3.15(b), the results of the remixed sample (not reground from the pellet) in the freezer-mill are shown. The evolution from $\sqrt{\omega}$ to ω^2 dependence on the MIR absorption coefficient starting from the lowest volume fraction can be clearly seen. However, the magnitude of absorption is still very large, but decreased from the samples mixed by hand. Next, the plot in Figure 3.15(c) shows the ordinary absorption coefficient after regrinding twice from the samples used in Figure 3.15(b). But, the volume fraction dependence is not still linear and the magnitude of the absorption is decreased again, but is still larger than the next plot, Figure 3.15(d). The results of the final stage of the grinding procedure is shown in Figure 3.15(d); the absorption coefficient now shows a linear dependence on the volume fraction. Also, the same effect for different particle sizes is shown in Figure 3.16.

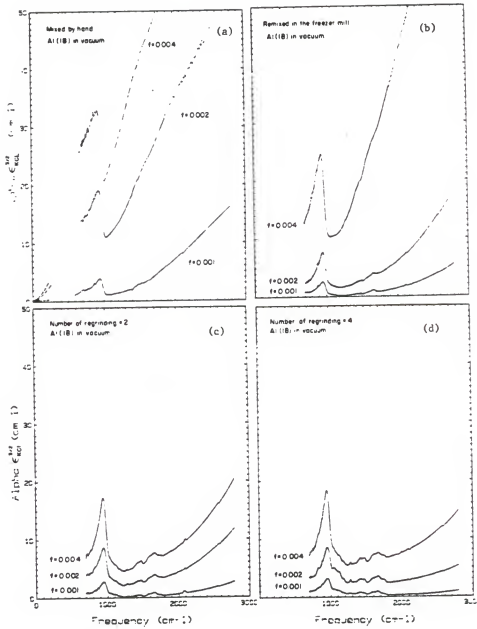


Figure 3.15 The grinding effect on MIR absorption data of Al (A1 18)-KCl composites (note that the absorption coefficients have been scaled by $\epsilon_{3/2}$)

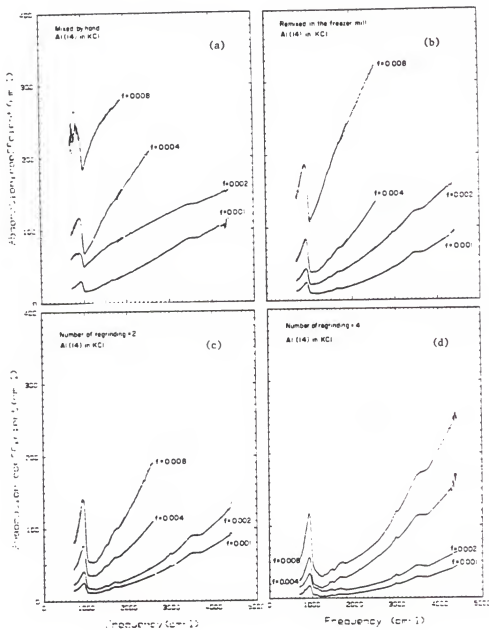


Figure 3.16 The grinding effect on MIR absorption coefficients of Al (Al 14)-KCl composites

Therefore, we can safely conclude that if the absorption coefficient is linear in f , then the sample satisfies the random homogeneity condition.

Visible Frequency Data

Now, a couple of the classical, but fundamental, tests can be made in this frequency range. For aluminum small particles interband absorption can be studied; for Au and Ag particles, the surface plasmon mode can be studied. The surface plasmon mode is not seen in Al because it occurs at $\omega = 6 \times 10^4 \text{ cm}^{-1}$ (7.6 eV).

The samples were diluted 10 times from $f = 0.001$ Al, Ag, or Au-KCl composite and reground 4 times for the optical measurements.

Interband Transition in Al

As can be seen in Appendix C, the parallel band absorption is one of the characteristics of simple nontransition metals. Bulk aluminum has this characteristic absorption at $12,000 \text{ cm}^{-1}$. Optical measurements on the diluted aluminum small particles composites showed an unexpected result that the location of the interband absorption peak of aluminum small particles was red-shifted by about $1,000 \text{ cm}^{-1}$ from that of a bulk aluminum as shown in Figure 3.17.

This surprising result may be interpreted as a result of expansion of the lattice constant of the aluminum small particle. Because, as shown in Appendix C, the absorption is caused by the pseudopotential U_{200} of aluminum parallel band and the pseudopotential is proportional to a^{-2} where a is the lattice constant. Therefore, a

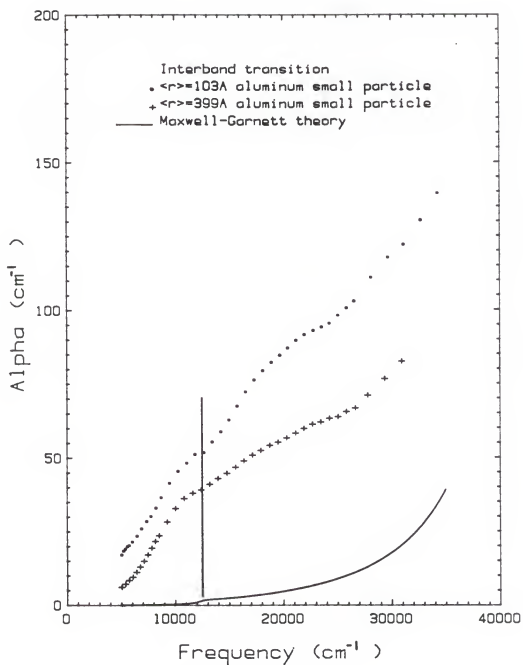


Figure 3.17 Interband transition of aluminum small particles

change in the lattice constant of a few percent leads to the red-shift in the interband absorption peak.

In addition, there is another broad structure developed around $20,000 \text{ cm}^{-1}$. The oscillator strength of this broad peak tends to decrease as the particle size gets larger (i.e., as the surface to volume ratio decreases). This peculiar structure might be due to the broken Bloch symmetry at the surface which has been ignored in the bulk system as discussed in Chapter I.

Surface Plasmon Mode

As briefly reviewed in Chapter I, another characteristic of a small particle is the Maxwell-Garnett resonance, which occurs at a frequency related to the plasma frequency by

$$\omega_s = \omega_p \sqrt{\frac{(1-f)}{(1-f)\epsilon_\infty + (2+f)\epsilon_0}} \quad (3.7)$$

where ω_p is the bare plasma frequency, ϵ_∞ is the core dielectric constant, and ϵ_m is the dielectric constant of the medium. Here the Drude dielectric function was used for ϵ_m .

Because Ag and Au are not free electron metals, the screened plasma frequency enables us to observe the surface plasmon when Ag or Au particles are dispersed in a medium with dielectric constant ϵ_0 (KCl was used in this study). The experimental observation of the Maxwell-Garnett resonance of Au-KCl composites is shown in Figure 3.18 and the resonance of Ag-KCl composites is shown in Figure 3.19. In order to fit the classical theory to the experiment, the volume fraction

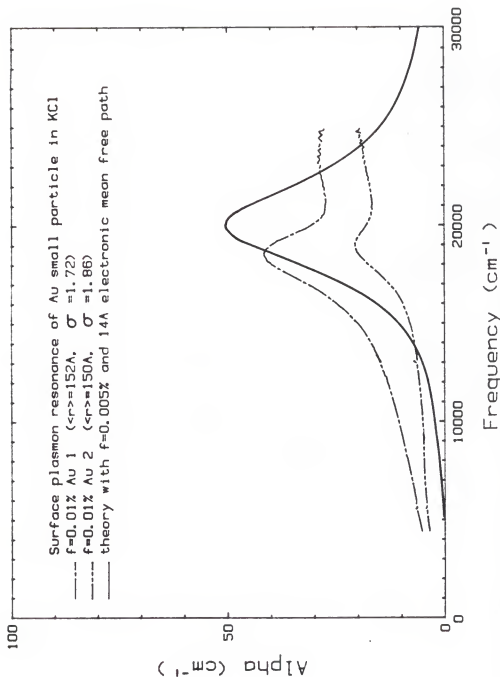


Figure 3.18 The Maxwell-Garnett resonance (surface plasmon mode) of Au-CK1 composite

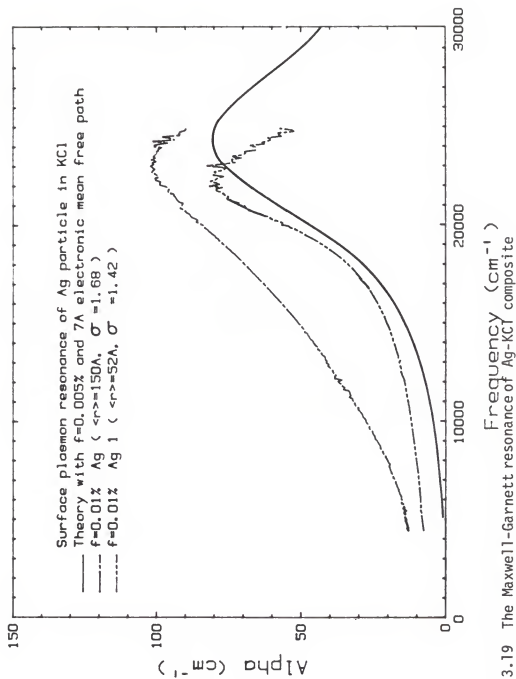


Figure 3.19 The Maxwell-Garnett resonance of Ag-KCl composite

had to be reduced by 20% which confirms that there were less small particles than estimated by the weight of the smoke.⁶⁶ Also, the observed resonance peaks are red shifted from the result of the classical theory. This problem can be solved by oxide coating⁶⁹ and by remembering that there was extra oxide contribution made from the source material and this source metal oxide enhanced ϵ_0 , leading to the red-shift.

The width of the resonance line was much broader than the prediction. Therefore, the order of 10 \AA electron mean free path had to be introduced to explain the experiment. As shown in Table 1.1, many similar results (broadening) were observed by other workers. Therefore, we have seen a tendency which favors the nonmetallic possibility in the small particle problem, because 10 \AA meanfree path is unrealistic if we assume metallic behavior.

Nonmetallic Possibility

Now, there are many things to be organized at this point. Because evidence for a behavior in small particles differing from the Drude particle point of view have been observed, some tests need to be done.

Electric or Magnetic Dipole?

As predicted by the Maxwell-Garnett theory in the low frequency and low volume fraction limit [see Equation (1.22)], the importance of either the electric dipole term or the magnetic dipole term can be determined by scaling the absorption coefficient by $\epsilon_0(\omega)^{3/2}$ or $\epsilon_0(\omega)^{1/2}$,

respectively, where $\epsilon_0(\omega)$ is the frequency dependent dielectric function of the surrounding medium. Because the magnetic dipole term is important when the DC conductivity is reasonably high, the conductivity of a small particle can be categorized by judging from this test. The results are shown in Figure 3.20. Also, an example of scaling by $\epsilon_0^{3/2}$ is shown in Figure 3.21 for overall frequencies.

The absorption coefficients scale well with $\epsilon_0^{3/2}$, favoring the electric dipole term for small size particles not the magnetic dipole. In other words, the intrinsic conductivity is more likely poor according to this analysis.

Electron Relaxation Time

The fundamental assumption of the Drude theory is that there is a constant relaxation time. Now, if we assume that the dielectric function of a small particle is the Drude dielectric function,

$$\epsilon_m(\omega) = 1 - \frac{\omega_p^2}{\omega^2 + i\omega/\tau} \quad (3.8)$$

and calculate the τ from the experimental data by writing the absorption coefficient such as

$$\alpha_{\text{exp}}(\omega) = F(\epsilon_0, f, \omega_p, \omega, \tau) \quad (3.9)$$

(Here, the Maxwell-Garnett effective dielectric function with only the electric dipole term is used), then the relaxation time τ can be calculated by inverting the function such as

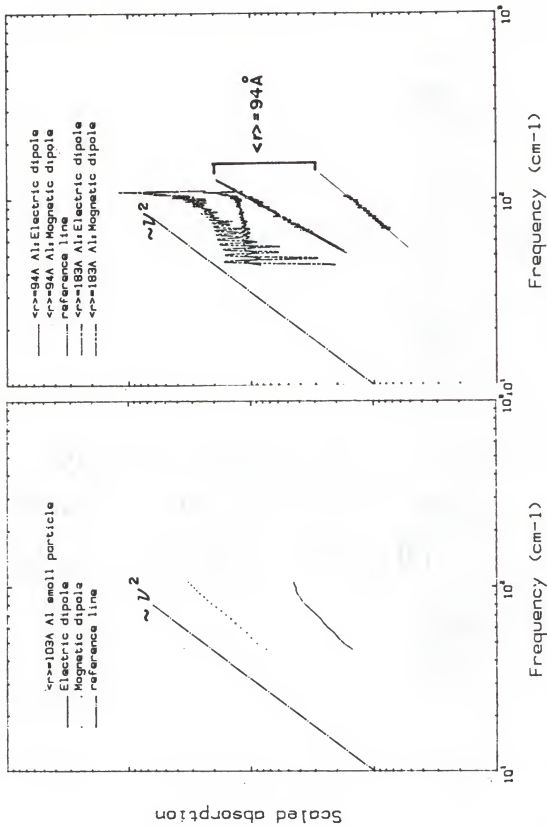


Figure 3.20 FIR absorption coefficients scaled by $\epsilon_0(\omega)^{3/2}$ and $\epsilon_0(\omega)^{1/2}$ for two different particle sizes

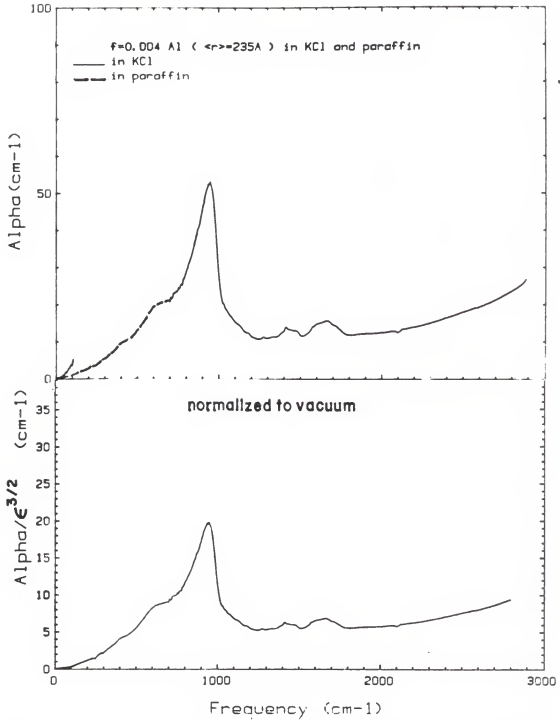


Figure 3.21 An example of absorption coefficient before and after scaling by $\epsilon_0(\omega)^{3/2}$; notice that the optical phonon frequency range of KCl is replaced by the data taken from Al-paraffin composites

$$\tau = G(\epsilon_0, f, \omega_p, \omega, \alpha_{\text{exp}}) \quad (3.10)$$

where the Maxwell-Garnett theory was used to describe the function. Then the particles will have dc conductivity.

$$\sigma = \frac{ne^2\tau}{m} \quad (3.12)$$

This conductivity is shown in Figure 3.22 for $\langle a \rangle = 235 \text{ \AA}$ size small particles. What we expect from this calculation is a constant value when we plot the dc conductivity versus frequency. But, the results surprisingly showed that the behavior of the small particle is rather close to that of an insulator! Therefore, we have the definite evidence of the non-Drudian behavior of a small particle.

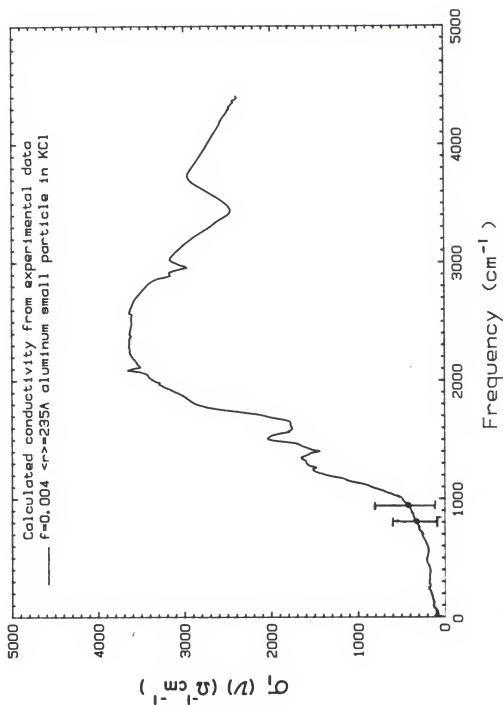


Figure 3.22 σ_{dc} of an aluminum small particle calculated from the experimental data

CHAPTER IV THEORY

Formalism

In this chapter, some consequences of the broken translational symmetry in the electron motion will be extensively studied within linear response theory and the random phase approximation (self-consistent field theory).^{70-72,49} Also, the theory will be compared to the experimental results and some predictions will be made for the experimental observation.

General Theory: Review

When a small sphere filled with electrons is placed in a semi-classical electromagnetic field, the response of electrons to the external field gives a perturbation to the density operator at equilibrium ρ^0 such as

$$\rho = \rho^0 + \rho^1 \quad (4.1)$$

to linear order in an external perturbation H_1 . By choosing a gauge in which the scalar potential vanishes, we have

$$H_1 = \frac{e}{2mc} (\vec{p} \cdot \vec{A} + \vec{A} \cdot \vec{p}) \quad (4.2)$$

Here \vec{A} is the vector potential and \vec{p} is the electron momentum. The unperturbed density operator, ρ^0 , satisfies

$$\rho^0 |i\rangle = f(E_i) |i\rangle \equiv f_i |i\rangle \quad (4.3)$$

where f_i is the Fermi-Dirac distribution function and $|i\rangle$ are the eigenstates of the unperturbed free particle Hamiltonian H_0 with eigenvalue E_i . Then the Liouville equation

$$i\hbar \frac{\partial \rho}{\partial t} = [H, \rho], \quad H = H_0 + H_1 \quad (4.4)$$

can be linearized by ignoring the second-order term in \tilde{A} . From Equations (4.1) and (4.4), we have

$$i\hbar \frac{\partial}{\partial t} \langle i | \rho^1 | j \rangle = \langle i | [H_1, \rho^0] | j \rangle + \langle i | [H_0, \rho^1] | j \rangle \quad (4.5)$$

where the higher order term $[H_1, \rho^1]$ has been ignored and the unperturbed contribution

$$i\hbar \frac{\partial}{\partial t} \langle i | \rho^0 | j \rangle = \langle i | [H_0, \rho^0] | j \rangle \quad (4.6)$$

has been subtracted. With

$$\tilde{A}(\vec{r}, t) = \tilde{A}(\vec{q}, \omega) e^{i(\vec{q} \cdot \vec{r} - \omega t)} \quad (4.7)$$

making the ansatz that $\langle i | \rho^1 | j \rangle$ has the same time dependence as $\tilde{A}(\vec{r}, t)$, and using the $i\eta$ prescription to switch adiabatically on the perturbation from $t = -\infty$ (throughout this chapter, $\lim_{\eta \rightarrow 0}$ is implicit), we have

$$\langle i | \rho^1 | j \rangle = \frac{f_i - f_j}{E_i - E_j - \hbar\omega - i\eta} \langle i | H_1 | j \rangle \quad (4.8)$$

By using Equations (4.2) and (4.7), we can rewrite Equation (4.8) as

$$\begin{aligned} \langle i | \rho^1 | j \rangle = & \frac{e}{mc} \frac{f_i - f_j}{E_{ij} - \hbar\omega - i\eta} \tilde{A}(\vec{q}, \omega) [\langle i | e^{i\vec{q} \cdot \vec{r}} \vec{p} | j \rangle \\ & + \frac{\hbar q}{2} \langle i | e^{i\vec{q} \cdot \vec{r}} | j \rangle] \end{aligned} \quad (4.9)$$

with $E_{ij} \equiv E_i - E_j$.

The induced current density $\vec{j}_{\text{ind}}(\vec{r}, t)$ may be derived from

$$\vec{j}_{\text{ind}}(\vec{r}, t) = \text{Tr} \{ \rho^0 \vec{j}^{(1)} + \rho^1 \vec{j}^{(0)} \} \quad (4.10)$$

where

$$\vec{j}^{(0)} = - \frac{e}{2m} [\vec{p} \delta(\vec{r} - \vec{r}_{\text{op}}) + \delta(\vec{r} - \vec{r}_{\text{op}}) \vec{p}] \quad (4.11a)$$

$$\vec{j}^{(1)} = - \frac{e^2}{mc} \tilde{A} \delta(\vec{r} - \vec{r}_{\text{op}}) \quad (4.11b)$$

and \vec{p} , \vec{r}_{op} are the momentum and position operators, respectively. By using the relation for an operator Ω in a statistical ensemble

$$\text{Tr}(\rho \Omega) = \sum_{ij} \langle i | \rho | j \rangle \langle j | \Omega | i \rangle \quad (4.12)$$

we have

$$\begin{aligned} \vec{J}_{\text{ind}}(\vec{r}, t) = & -\frac{e^2}{mc} \sum_{ij} f_i \langle i | \vec{A} \delta(\vec{r} - \vec{r}_{\text{op}}) | i \rangle \delta_{ij} \\ & - \sum_{ij} \langle i | \rho^1 | j \rangle \langle j | \vec{J}^{(0)} | i \rangle \end{aligned} \quad (4.13)$$

Carrying out the Fourier transformation on Equation (4.13), and using Equation (4.9), we obtain

$$\begin{aligned} \vec{J}_{\text{ind}}(\vec{k}, \omega) = & \frac{ie^2}{Vmc} \vec{A}(\vec{q}, \omega) \sum_i f_i \langle i | e^{i(\vec{q}-\vec{k}) \cdot \vec{r}} | i \rangle \\ & - \frac{e^2}{Vmc^2} \sum_{ij} \frac{f_i - f_j}{E_{ij} - \hbar\omega - i\eta} \\ & \cdot \left[\langle i | e^{i\vec{q} \cdot \vec{r}} \vec{A}(\vec{q}, \omega) \cdot \vec{p} | j \rangle \right. \\ & \left. + \frac{1}{2} \hbar \vec{q} \cdot \vec{A}(\vec{q}, \omega) \langle i | e^{i\vec{q} \cdot \vec{r}} | j \rangle \right] \\ & \times \left[\langle j | e^{i\vec{k} \cdot \vec{r}} \vec{p} | i \rangle - \frac{1}{2} \hbar \vec{k} \cdot \langle j | e^{i\vec{k} \cdot \vec{r}} | i \rangle \right] \end{aligned} \quad (4.14)$$

where V is the volume of the system and \vec{k} is the Fourier component vector.

By assuming homogeneity in the system, i.e., that there is a response only at the wave vector of the external field (i.e., that $\vec{q} = \vec{k}$), and by taking the $\vec{q} \rightarrow 0$ limit) dipole approximation), as appropriate for a small particle,⁷³ we find

$$\begin{aligned} \vec{J}_{\text{ind}}(\omega) = & \frac{ie^2}{mc} \frac{N_e}{V} A(\omega) \\ & - \frac{e^2}{Vm^2c} \sum_{ij} \frac{f_i - f_j}{E_{ij} - \hbar\omega - i\eta} [\vec{A}(\omega) \cdot \langle i | \vec{p} | j \rangle \langle j | \vec{p} | i \rangle] \end{aligned} \quad (4.15)$$

where $N_e = \sum_i f_i$, the total number of electrons in the system.

Therefore, we can derive the conductivity, $\sigma(\omega)$, and the dielectric function, $\epsilon(\omega)$, by using the following formulae with the Coulomb gauge.

$$\vec{E}(\omega) = \frac{i\omega}{c} \vec{A}(\omega) \quad (4.16)$$

$$\vec{J}_{\text{ind}}(\omega) = \sigma(\omega) \vec{E}(\omega) \quad (4.17)$$

and

$$\epsilon(\omega) = 1 + \frac{4\pi i \sigma(\omega)}{\omega} \quad (4.18)$$

$\epsilon(\omega)$

From Equations (4.15) and (4.17), we have

$$\sigma(\omega) = i \left[\frac{e^2}{m\omega} \frac{N_e}{V} + \frac{e^2}{Vm^2\omega} \sum_{ij} \frac{f_i - f_j}{E_{ij} - \hbar\omega - i\eta} |\langle i | \vec{p} | j \rangle|^2 \right] \quad (4.19)$$

Here the vector notation in \vec{p} represents the direction of the momentum along the applied field. Also, the dielectric function $\epsilon(\omega)$ can be found from Equations (4.18) and (4.19):

$$\epsilon(\omega) = \left[1 - \frac{\omega_p^2}{\omega^2} \right] - \frac{4\pi e^2}{Vm^2\omega^2} \sum_{ij} \frac{f_i - f_j}{E_{ij} - \hbar\omega - i\eta} |\langle i | \vec{p} | j \rangle|^2 \quad (4.20)$$

where $\omega_p^2 = \frac{4\pi ne^2}{m}$ and $n = N_e/V$. Now, we have the free electron behavior term in the square brackets and a correction term due to the broken symmetry in the third term of Equation (4.20). This correction term will vanish in the $a \rightarrow \infty$ limit. This limit describes the free electron system without relaxation (i.e., $\tau \rightarrow \infty$, τ = electron relaxation time).

It is normally assumed that η goes to zero after the integration. This is a prescription included in the RPA to prevent the divergence of the time integral. In contrast, Wood and Ashcroft⁴⁹ assumed an actual physical meaning to the $i\eta$ term. They identified η with \hbar/τ , τ being the usual (Drude-model) relaxation time.

A different interpretation, however, will be made in this dissertation, which uses the identity

$$\lim_{\eta \rightarrow 0} \frac{1}{x - i\eta} = P\left(\frac{1}{x}\right) + i\pi\delta(x) \quad (4.21)$$

where P stands for the principal part. Then we can explicitly separate the real part and the imaginary part of the dielectric function such as

$$\epsilon_1(\omega) \equiv \text{Re } \epsilon(\omega) = 1 - \frac{\omega_p^2}{\omega^2} - \frac{4\pi e^2}{V_m \omega^2} \sum_{ij} \frac{f_i - f_j}{E_{ij} - \hbar\omega} \langle i | \vec{p} | j \rangle^2 \quad (4.22)$$

and

$$\epsilon_2(\omega) \equiv \text{Im } \epsilon(\omega) = \frac{4\pi^2 e^2}{V_m \omega^2} \sum_{ij} (f_j - f_i) |\langle i | \vec{p} | j \rangle|^2 \delta(E_{ij} - \hbar\omega) \quad (4.23)$$

Also, from Equation (4.18), we can find the conductivity such as

$$\sigma(\omega) = \frac{i\omega}{4\pi} [1 - \epsilon(\omega)] \equiv \sigma_1(\omega) + i\sigma_2(\omega) \quad (4.24)$$

Equations (4.22) and (4.23) describe divergences in $\epsilon(\omega)$ at $\hbar\omega = E_{ij} = E_i - E_j$ and give infinitely sharp absorption lines in ϵ_2 . In practice, we never see such sharp absorption lines because of broadening effects. For a small particle, a quantum mechanical broadening needs to be considered, as discussed in Chapter I and Appendices A and B, since the quantum mechanical role of the surface is not that of a scattering center, but in determining the eigenstates of bound electrons. Because the random irregularity of the surface plays an important role (level correlation), averaging a physical quantity over impurities and imperfections on the surface⁷⁴ is the most important contribution to the broadening.

Small Particle and Matrix Element

The crucial point in the RPA small particle theory is the evaluation of the matrix element

$$|\vec{p}_{ij}|^2 = |\langle i | \vec{p} | j \rangle|^2 \quad (4.25)$$

The momentum matrix elements given by Equation (4.25) can be transformed into a position matrix representation, which is more appealing in the case of a small particle because the effect of broken symmetry can be directly visualized, by making use of the Ehrenfest theorem

$$\frac{d}{dt} \langle \vec{r} \rangle = -\frac{i}{\hbar} [\vec{r}, H] \quad (4.26)$$

Thus, we have

$$\langle i | \vec{p} | j \rangle = -i \frac{m}{\hbar} \langle i | [\vec{r}, H_0] | j \rangle = -i \frac{m}{\hbar} E_{ij} \langle i | \vec{r} | j \rangle \quad (4.27)$$

Here the vector notation represents the direction along the applied field again. Therefore, the momentum matrix elements will be replaced with the corresponding position matrix elements whenever we need a clear physical description of $\epsilon(\omega)$ and $\sigma(\omega)$.

The matrix elements given by Equation (4.27) can be evaluated, in principle, if we know the eigenstates and eigenvalues of a given Hamiltonian from the solution to the Schrödinger equation. However, finding the solutions to the Schrödinger equation is impossible in our model because of the random nature in the boundary condition. Hence,

a reasonable approximation needs to be made to evaluate the matrix elements.

Low Frequency Limit

Now, because the matrix elements generally depend on the energy eigenvalues of given eigenstates, for frequencies below a minimum energy gap of the system, we can approximate the matrix elements by considering electrons on the Fermi surface such as

$$|\langle i | \vec{r} | j \rangle|^2 \equiv |\vec{r}_{ij}|^2 = \frac{1}{3} |r_{ij}|^2 \quad (4.28a)$$

and

$$|r_{ij}|_{E_F}^2 = \left\{ \frac{1}{V} \int r^2 d\vec{r} \right\}_{E=E_F} = \frac{3}{5} a^2 \quad (4.28b)$$

Here we have taken the spatial average on $|r_{ij}|^2$.

For frequencies above the minimum energy gap, we expect that electrons in a small particle will recover some "free" electron nature. Thus, we can treat the problem semiclassically by employing the Shapoval method⁷⁵ when the De Broglie wave length of electrons do not exceed the roughness of the surface (i.e., the diffusive scattering case).

Starting from the Heisenberg picture, the average of two physical observables $f(t)$ and $g(t + t')$ in a state $|i\rangle$ at a time difference t' can be calculated as

$$\begin{aligned}
\langle f(t)g(t+t') \rangle_i &= \langle i | f(t)g(t+t') | i \rangle \\
&= \sum_j \langle i | f(t) | j \rangle \langle j | g(t+t') | i \rangle
\end{aligned} \quad (4.29)$$

By changing Equation (4.29) to the Schrödinger picture, we have

$$\langle f(t)g(t+t') \rangle_i = \sum_j e^{-i\omega_{ij}t'} \langle i | f | j \rangle \langle j | g | i \rangle \quad (4.30)$$

where we have defined ω_{ij} as $\omega_{ij} \equiv \frac{E_{ij}}{\hbar}$. For $f = g = r$, we have

$$\langle r(t)r(t+t') \rangle_i = \sum_j e^{-i\omega_{ij}t'} |r_{ij}|^2 \quad (4.31)$$

Now, by changing the summation to an integration, we can rewrite Equation (4.31) as

$$\langle r(t)r(t+t') \rangle_i = \hbar v(E_F) \int_{-\infty}^{\infty} e^{-i\omega t'} |r_{ij}|^2 d\omega \quad (4.32)$$

where $v(E_F)$ is the density of states at the Fermi level $\left\{ v(E_F) = \frac{V m p_F}{\pi^2 \hbar^3} \right.$, p_F = Fermi momentum $\left. \right\}$. After the Fourier transformation, we get

$$|r_{ij}|^2 = \frac{1}{2\pi \hbar v(E_F)} \int_{-\infty}^{\infty} \langle r(t)r(t+t') \rangle_i e^{i\omega_{ij}t'} dt' \quad (4.33)$$

Next, the quantity in the angular brackets of Equation (4.33) can be averaged by taking into account the classical trajectory of electrons in the diffusive scattering limit as

$$\langle r(t)r(t+t') \rangle_i = \frac{1}{2T} \int_{-T}^T dt r(t)r(t+t') \quad (4.34)$$

The autocorrelation function, $\langle r(t)r(t+t') \rangle$ vanishes when t' coincides with a/v_F , which is the minimum time interval to have a surface scattering. Also, since the autocorrelation function is an even function, we can rewrite Equation (4.33) in the form of a cosine Fourier transform:

$$|r_{ij}|^2 = \frac{1}{\pi \hbar v(E_F)} \int_0^\infty \langle r(t)r(t+t') \rangle_i \cos(\omega_{ij}t') dt' \quad (4.35)$$

For very low frequencies ($\omega \ll v_F/a$), we can ignore the frequency dependence of the matrix elements because $\cos(\omega t')$ is close to unity. Thus, the matrix elements are independent of the energy states in this limit. Therefore, we can set the matrix elements to

$$\begin{aligned} |r_{ij}|^2 &= |r_{ij}|_0^2 = \frac{1}{\pi \hbar v(E_F)} \int_0^\infty \langle r(t)r(t+t') \rangle_i dt \\ &= \frac{1}{\pi \hbar v(E_F)} \frac{1}{2T} \int_{-T}^T dt \int_0^\infty dt' r(t)r(t+t') \end{aligned} \quad (4.36)$$

The integration given by Equation (4.36) can be done⁷ to give

$$|r_{ij}|_0^2 = \frac{139}{150} \frac{a^2}{2\pi \hbar v(E_F)} \left[\frac{a}{v_F} \right] \quad (4.37)$$

High Frequency Limit

In the limit of high frequencies ($\omega \gg v_F/a$), a quasi-continuous behavior of electrons in a small particle is anticipated. In other words, unlike the low frequency limit, the details of discrete level structures become unimportant. However, in our small particle model, surface roughness is expected still to play an important role. This point will be clear later in the surface plasmon broadening section.

For a sphere with a smooth surface, we can easily find eigenstates of the Schrödinger equation in terms of spherical Bessel functions (see Appendix A and Reference 48). But, working with these eigenstates to evaluate the position matrix elements is cumbersome. Furthermore, it is impossible to determine the eigenstates for a sphere with a rough surface. However, Kawabata and Kubo⁴⁸ simplified the situation for a smooth sphere by introducing a surface potential, $U(\vec{r})$, as follows:

$$\begin{aligned}
 \langle i | \vec{r} | j \rangle &= \frac{1}{E_{ij}} \langle i | [H, \vec{r}] | j \rangle \\
 &= -\frac{i\hbar}{m} \frac{1}{E_{ij}^2} \langle i | [H, \vec{p}] | j \rangle \\
 &= \frac{\hbar^2}{m} \frac{1}{E_{ij}^2} \langle i | \frac{\partial U(\vec{r})}{\partial \vec{r}} | j \rangle
 \end{aligned} \tag{4.38}$$

from the commutation relations

$$[H, \vec{r}] = -\frac{i\hbar}{m} \vec{p} \quad \text{and} \quad [H, \vec{p}] = i\hbar \frac{\partial U(\vec{r})}{\partial \vec{r}} \quad (4.39)$$

This idea can be used in our small particle model by treating $U(\vec{r})$ as a position dependent random surface potential to take into account the effect of surface roughness. However, further systematic investigation needs to be done in the future.

Calculation of $\epsilon(\omega)$

From Equations (4.22), (4.23), (4.24), and (4.27), we have the desired expression for $\epsilon(\omega)$ as follows:

$$\epsilon(\omega) = \epsilon_1(\omega) + \frac{4\pi\sigma_1(\omega)}{\omega} \quad (4.40)$$

where

$$\epsilon_1(\omega) = 1 - \frac{\omega_p^2}{2} \sum_{ij} \frac{f_i - f_j}{E_{ij} - \hbar\omega} \left[\frac{E_{ij}}{\hbar\omega} \right]^2 |\vec{r}_{ij}|^2 \quad (4.41)$$

and

$$\sigma_1(\omega) = \frac{\pi e^2 \omega}{V} \sum_{ij} (f_j - f_i) |\vec{r}_{ij}|^2 (E_{ij} - \hbar\omega) \quad (4.42)$$

$\epsilon(\omega)$ given by Equation (4.41) can be rearranged in two equivalent forms to give a better convergence in a series expansion or a clearer physical meaning by interchanging indices i and j in the summation in Equation (4.41) to

$$\epsilon_1(\omega) = 1 - \frac{\omega_p^2}{\omega^2} - \frac{4\pi e^2}{V} \sum_{ij} \left(\frac{E_{ij}}{\hbar\omega} \right)^2 \frac{(f_i - f_j) E_{ij} |\vec{r}_{ij}|^2}{E_{ij}^2 - (\hbar\omega)^2} \quad (4.43)$$

or

$$\epsilon_1(\omega) = 1 - \frac{\omega_p^2}{\omega^2} - \frac{8\pi e^2}{V} \sum_{ij} \left(\frac{E_{ij}}{\hbar\omega} \right)^2 \frac{f_i E_{ij} |\vec{r}_{ij}|^2}{E_{ij}^2 - (\hbar\omega)^2} \quad (4.44)$$

from

$$\frac{f_i - f_j}{E_{ij} - \hbar\omega} = \frac{E_{ij}(f_i - f_j)}{E_{ij}^2 - (\hbar\omega)^2} \text{ and } \sum_{ij} \frac{f_i - f_j}{E_{ij} - \hbar\omega} = 2 \sum_{ij} \frac{f_i E_{ij}}{E_{ij}^2 - (\hbar\omega)^2}$$

Level Correlation

The most interesting physical quantities in a small particle are correlation functions. The energy correlation function of a small particle $R(\omega)$, defined as

$$R(\omega) = \frac{1}{4\hbar\omega[V(E_F)]^2} \sum_{ij} (f_j - f_i) \delta(E_{ij} - \hbar\omega) \quad (4.45)$$

has a direct connection to the response to an external electromagnetic field, because it gives the probability of finding two energy levels a distance $\hbar\omega$ apart. Here the angular brackets in Equation (4.45) represent the average over all impurities and imperfections in the system. This averaging process is necessary to include the quantum broadening as discussed earlier in this chapter.

Generally, the evaluation of averaged physical quantities like Equation (4.45) is difficult because it is impossible to find exact solutions of the Schrödinger equation in such systems. Perturbation techniques can be used in limited cases, when the Hamiltonian can be expanded in a series over sufficiently weak random potentials.

Another method developed to calculate such averaged quantities is the replica method,^{76,77} applied first to the spin glass problem, which replaces the random system by n subsystems identical to the original and uses the identity

$$\ln x = \lim_{n \rightarrow 0} \left[\frac{x^n - 1}{n} \right] \quad (4.46)$$

Thus, one can carry out the averaging procedure before taking the $n \rightarrow 0$ limit (e.g., for a free energy, $F = -k_B T \ln Z$, we can calculate the average value of Z first and then take $n \rightarrow 0$ limit). However, there are many difficulties in applying this method because analytical continuation or an integer condition for n in the standard approximation usually fails in the $n \rightarrow 0$ limit.

Recently, Efetov⁷⁸ evaluated the two-level correlation function given by Equation (4.45) which can be rewritten in terms of the retarded (-) and advanced (+) Green's function, G^\pm , such as

$$R(\omega) = \frac{1}{8\pi^2 \hbar \omega [v(E_F)]^2} < \text{Re} \int_{-\infty}^{\infty} dE \sum_{ij} [f(E + \hbar\omega) - f(E)] G_i^+(E) \\ \times \{ G_j^+(E + \hbar\omega) - G_j^-(E + \hbar\omega) \} > \quad (4.47)$$

by applying the supersymmetry method.^{79,80} The main advantage of using this method is that the Green's function can be reexpressed in the form of functional integrals by employing the supervector and the supermatrix algebra and the new Green's function does not have the weight denominator which appears in the ordinary form.

Now, we can take the average on Equation (4.47) at the beginning on the product of new Green's functions and this procedure requires a fair amount of mathematical art. Surprisingly, Efetov⁷⁸ found results which exactly coincide with those derived on the basis of Dyson's phenomenological theory for three different ensembles, shown in Appendix B, by using a zero-dimensional supermatrix σ -model.

With the aid of this important consequence of the new calculation of the two-level correlation function, we can evaluate averaged quantities over surface imperfections and impurities.

Low Frequency Limit

In the low frequency limit where the discreteness of energy levels and their correlation is important, a subtle distinction is necessary to obtain the correct low frequency form because of the diamagnetic current contribution which results in ω_p^2/ω^2 term in Equation (4.22).

If we can choose a minimum gap energy, ΔE_{\min} , one may expand the formula given by Equation (4.44) for the frequency range below ΔE_{\min} to obtain the low frequency form such as

$$\begin{aligned} \epsilon_1(\omega) = 1 - \frac{\omega_p^2}{\omega^2} - \frac{8\pi e^2}{V} \frac{1}{(\hbar\omega)^2} \sum_{ij} f_i E_{ij} |\vec{r}_{ij}|^2 \left\{ 1 \right. \\ \left. + \left(\frac{\hbar\omega}{E_{ij}} \right)^2 + O(\omega^4) \right\} \\ = \left\{ 1 - \frac{8\pi e^2}{V} \sum_{ij} \frac{f_i |\vec{r}_{ij}|^2}{E_{ij}} \right\} - \frac{\omega_p^2}{\omega^2} \frac{m}{m^*} + O(\omega^2) \end{aligned} \quad (4.48)$$

where

$$\frac{m}{m^*} \equiv 1 + \frac{8\pi e^2}{V} \frac{1}{(\hbar\omega_p)^2} \sum_{ij} f_i E_{ij} |\vec{r}_{ij}|^2 \quad (4.49)$$

We can show that the optical effective mass (m^*) defined by Equation (4.49) becomes infinite (i.e., there is no continuum contribution) in a truly discrete quantum system for frequencies smaller than the gap by applying the Thomas-Reiche-Kuhn sum rule

$$\sum_j E_{ij} |\vec{r}_{ij}|^2 = -\frac{\hbar^2}{2m} \quad (4.50)$$

and $\sum_i f_i = N_e$. Thus, the optical effective mass ratio vanishes in a small particle for the same reason. Therefore, we may rewrite the general result given by Equation (4.41) as

$$\epsilon_1(\omega) = 1 - \frac{4\pi e^2}{V} \left\langle \sum_{ij} \frac{(f_i - f_j) E_{ij} |\vec{r}_{ij}|^2}{E_{ij}^2 - (\hbar\omega)^2} \right\rangle \quad (4.51)$$

for frequencies below the gap by following the argument given in Equation (4.48). Here the angular brackets represent the average over all impurities and imperfections on the surface. Also, the same averaging process needs to be considered for $\sigma_1(\omega)$ to give

$$\sigma_1(\omega) = \frac{\pi e^2 \omega}{V} \left\langle \sum_{ij} (f_j - f_i) |\vec{r}_{ij}|^2 \delta(E_{ij} - \hbar\omega) \right\rangle \quad (4.52)$$

At this point, we have confirmed the Kubo formula derived from the fluctuation-dissipation theorem which leads to

$$\sigma_1(\omega) = \text{Re } \sigma(\omega) = \int_0^\infty dt \int_0^\beta d\lambda e^{-i\omega t} \langle \vec{J}(0) \vec{J}(t + i\lambda) \rangle \quad (4.53)$$

Here $\beta = 1/k_B T$ and $\vec{J}(t)$ represents the current operator in the Heisenberg picture. Equation (4.52) can be recovered immediately from Equation (4.53) after some algebra.⁸¹

Now, the static part of the electric susceptibility defined as

$$\chi_e^0 \equiv \lim_{\omega \rightarrow 0} \chi_e(\omega) = \lim_{\omega \rightarrow 0} \left\{ \frac{\epsilon_1(\omega) - 1}{4\pi} \right\} \quad (4.54)$$

$$= - \frac{e^2}{V} \left\langle \sum_{ij} \frac{(f_i - f_j) |\vec{r}_{ij}|^2}{E_{ij}} \right\rangle \quad (4.55)$$

can be evaluated as

$$\chi_e^0 = \frac{3}{80\pi} \frac{(\hbar\omega_p)^2}{E_F} \left(\frac{a_0}{e}\right)^2 \left(\frac{a}{a_0}\right)^2 \quad (4.56a)$$

or

$$= \frac{\gamma k_F a_0}{5\pi^2} \left(\frac{a}{a_0}\right)^2 \quad (4.56b)$$

where a_0 = Bohr radius = $\frac{\hbar^2}{me^2}$, $\hbar k_F = m^* v_F$, and γ is the specific heat mass ratio (m^*/m). [N.B., γ is different from the mass ratio defined by Equation (4.49).] We have used the following relations to obtain Equation (4.56) from Equation (4.55):

$$f_i - f_j \sim -\delta(E_F - E_j) E_{ij} \quad (4.57a)$$

$$v(E_F) = 2 \sum_j \delta(E_F - E_j) \quad (4.57b)$$

and Equation (4.28).

By taking into account the statistical nature of the energy gap of a small particle as discussed in Appendix B, we obtain the frequency dependent susceptibility, $\chi_e(\omega)$ as

$$\chi_e(\omega) = \frac{e^2}{V} \left(\frac{a^2}{5} \right) \left\langle \sum_{ij} \frac{E_{ij}^2}{E_{ij}^2 - (\hbar\omega)^2} \delta(E_F - E_{ij}) \right\rangle, \quad \hbar\omega \lesssim \Delta E \quad (4.58)$$

$$\begin{aligned} &= \frac{e^2}{V} \left(\frac{a^2}{5} \right) \frac{1}{2} v(E_F) \left\{ v(E_F) \int_0^\infty dE \frac{E^2 P(E)}{E^2 - (\hbar\omega)^2} \right\} \\ &= \chi_e^0 \int_0^\infty dx \frac{x^2 P(x)}{x^2 - \left(\frac{\hbar\omega}{\Delta E} \right)^2}, \quad x = E/\Delta E \end{aligned} \quad (4.59)$$

where $P(E_{ij})$ is the level distribution function which depends on a statistical ensemble in the system. These $P(E_{ij})$ have been shown to be^{82,83}

$$p^{\text{ort}}(x) = \frac{\pi x}{2} e^{-\frac{\pi}{4}x^2} \quad (\text{orthogonal ensemble}) \quad (4.60)$$

$$p^{\text{unit}}(x) = \frac{32}{\pi} x^2 e^{-\frac{4}{\pi}x^2} \quad (\text{unitary ensemble}) \quad (4.61)$$

$$p^{\text{symp1}}(x) = \left(\frac{8}{3} \right)^6 \frac{1}{\pi} x^4 e^{-\frac{64}{9\pi}x^2} \quad (\text{symplectic ensemble}) \quad (4.62)$$

For the orthogonal ensemble, for example, we find

$$\chi_e^{\text{ort}}(\omega) = \chi_e^0 \left\{ 1 - \frac{\pi}{4} \left(\frac{\hbar\omega}{\Delta E} \right)^2 e^{-\frac{\pi}{4} \left(\frac{\hbar\omega}{\Delta E} \right)^2} \text{Ei} \left[\frac{\pi}{4} \left(\frac{\hbar\omega}{\Delta E} \right)^2 \right] \right\} \quad (4.63)$$

with the aid of the formula

$$\int_0^{\infty} \frac{n^2 e^{-\mu x}}{x + \beta} dx = (-1)^{n-1} \beta^n e^{\beta\mu} \text{Ei}(-\beta\mu) + \sum_{k=1}^n (k-1)! (-\beta)^{n-k} \mu^{-k} \quad (4.64)$$

from Gradshteyn and Ryzhik.⁸⁴ Here $\text{Ei}(x)$ is the exponential integral defined as

$$\text{Ei}(x) = \int_{-\infty}^x \frac{e^t}{t} dt \quad (4.65)$$

But, one difficulty arising in the analytic evaluation of $\chi_e(\omega)$ is the limitation on the range of x in $\text{Ei}(x)$ because the level distribution function covers the frequencies up to $\hbar\omega/\Delta E \sim 25$ for a smooth connection to $\chi_e(\omega)$ for $\hbar\omega > \Delta E$. Therefore, $\chi_e(\omega)$ was evaluated numerically in this work.

Also, the real part of the conductivity, $\sigma_1(\omega)$, given by Equation (4.52) can be calculated as the same way done in the $\chi_e(\omega)$ calculation to give

$$\sigma_1(\omega) = \frac{\pi e^2 \omega}{V} \left(\frac{a^2}{5} \right) \left\langle \sum_{ij} E_{ij} \delta(E_F - E_j) \delta(E_{ij} - \hbar\omega) \right\rangle \quad (4.66)$$

$$= \frac{\pi e^2 \omega}{V} \left(\frac{a^2}{5} \right) \cdot \frac{1}{2} v(E_F) \left\{ v(E_F) \int_{-\infty}^{\infty} dE E P(E) \delta(E - \hbar\omega) \right\} \quad (4.67)$$

Therefore, for $\hbar\omega \lesssim \Delta E$, we have

$$\sigma_1^N(\omega) = c_N \left(\frac{\gamma k_F a_0}{5\pi} \right) \left(\frac{a}{a_0} \right)^2 \left(\frac{\Delta E}{\hbar} \right) \left(\frac{\hbar\omega}{\Delta E} \right)^{N+2} e^{-\mu_N \left(\frac{\hbar\omega}{\Delta E} \right)^2} \quad (4.68)$$

Here

$$c_1 = \frac{\pi}{2} \text{ and } \mu_1 = \frac{\pi}{4} \quad \text{for orthogonal ensemble (N = 1)}$$

$$c_2 = \frac{32}{\pi^2} \text{ and } \mu_2 = \frac{4}{\pi} \quad \text{for unitary ensemble (N = 2)}$$

and

$$c_4 = \left(\frac{8}{3} \right)^6 \frac{1}{3} \text{ and } \mu_4 = \frac{64}{9\pi} \quad \text{for symplectic ensemble (N = 4)}$$

One interesting prediction of this calculation is that the dc conductivity defined as

$$\sigma_{dc} = \lim_{\omega \rightarrow 0} \sigma_1(\omega) \quad (4.69)$$

vanishes for a small particle. Classically, this point can be viewed as a finite q case³² (note that the Drude dielectric function is a limiting case of $q = 0$). Therefore, a small particle is an insulator!*

For frequencies above the gap, we cannot use the low frequency form of $\epsilon_1(\omega)$ given by Equation (4.51) directly because the role of the diamagnetic current becomes important in this frequency range. Thus, by rewriting the ω_p^2/ω^2 term in Equation (4.43) as

*The term insulator means the vanishing dc conductivity at zero temperature.

$$\frac{\omega_p^2}{\omega^2} = - \frac{4\pi e^2}{V} \frac{1}{(\hbar\omega)^2} \sum_{ij} (f_i - f_j) E_{ij} |\vec{r}_{ij}|^2 \quad (4.70)$$

we obtain

$$\epsilon_1(\omega) = 1 - \frac{4\pi e^2}{V} \left\langle \sum_{ij} \frac{(f_i - f_j) E_{ij} |\vec{r}_{ij}|^2}{E_{ij}^2 - (\hbar\omega)^2} \right\rangle, \quad \hbar\omega > \Delta E_{\min} \quad (4.71)$$

without loss of generality. Note that Equation (4.71) is identical with Equation (4.51) except that the valid frequency range is above the gap and the position matrix elements are different in this frequency range. In other words, the contribution of the static part of the susceptibility should vanish for this frequency range. This result provides a correct physical description of a small particle because there will be no contributions of transitions across the gap to the susceptibility at frequencies above the gap like ordinary nonmetallic systems.

Because the electrons in a small particle are expected to recover some free electron character for frequencies above the gap, we have

$$\sigma_1(\omega) = \frac{\pi e^2 \omega}{V} |\vec{r}_{ij}|_0^2 \left\langle \sum_{ij} (f_j - f_i) \delta(E_{ij} - \hbar\omega) \right\rangle \quad (4.72)$$

$$= \frac{139}{600 \pi^2} \frac{\gamma}{k_F a_0} \omega \left\{ \frac{2\pi \hbar \omega}{\Delta E} R(\omega) \right\} \quad (4.73)$$

from the definition of $R(\omega)$ given by Equation (4.43) and the matrix elements given by Equation (4.37).

For $\epsilon_1(\omega)$ above the gap, we obtain

$$\epsilon_1(\omega) = 1 + 4\pi \left\{ \frac{139}{1200} \frac{\gamma}{\pi^2} \frac{\gamma}{k_F a_0} \cdot \frac{1}{2} (\hbar\omega)^2 v(E_F) \right. \\ \left. \cdot \int_{-\infty}^{\infty} dE \frac{R(E)}{E^2 - (\hbar\omega)^2} \right\} \quad (4.74)$$

$$= 1 + 4\pi \left\{ \frac{139}{2400} \frac{\gamma}{\pi^2} \frac{\gamma}{k_F a_0} F(\omega) \right\} \quad (4.75)$$

because the effects of the averaging process are now absorbed into the level correlation. The dimensionless function $F(\omega)$ defined as

$$F(\omega) = (\hbar\omega)^2 v(E_F) \int_{-\infty}^{\infty} dE \frac{R(E)}{E^2 - (\hbar\omega)^2} \quad (4.76)$$

is identical to the real part of the function $A(\omega)$ defined by Gor'kov and Eliashberg⁷ [however, note that Devaty and Sievers⁸⁵ reevaluated the function $A(\omega)$ and corrected errors in the original calculation].

$F(\omega)$ for three different ensembles are given by

$$F^{\text{ort}}(x) = 2 - \frac{\sin x}{x} + (2x) \text{Ci}(x) \frac{d}{dx} \left[\frac{\sin x}{x} \right] \quad (4.77)$$

$$F^{\text{unit}}(x) = 2 - \frac{\sin x}{x} \quad (4.78)$$

and

$$F^{\text{symp1}}(y) = 2 - \frac{\sin 2y}{2y} + y \operatorname{Si}(y) \frac{d}{dx} \left(\frac{\cos y}{y} \right) \quad (4.79)$$

where

$$y = 2x = \frac{2\pi\hbar\omega}{\Delta E}, \quad \operatorname{Ci}(x) = - \int_x^\infty \frac{\cos t}{t} dt, \quad \text{and} \quad \operatorname{Si}(x) = \int_0^x \frac{\sin t}{t} dt$$

A general behavior of $\epsilon_1(\omega)$ and $\sigma_1(\omega)$ for three different ensembles is shown in Figure 4.1. One remarkable result of this theory is that $\epsilon_1(\omega)$ naturally converges to $(1 + 4\pi\chi_e^0)$ as $\omega \rightarrow 0$ unlike the Gor'kov and Eliashberg case which will be shown in the next section. Note that the static part of the dielectric function is effectively canceled out as the frequency increases across the gap frequency and the dielectric function converges toward 1 and makes a smooth connection to the result of Equation (4.75) at frequencies away from the gap. Also, note that the behavior of $\epsilon_1(\omega)$ is quite similar to that of an ideal insulator at the visible and ultraviolet frequency ranges.⁸⁶ In other words, the same physical phenomena occurring at high frequencies in a nonmetallic system have been brought down to FIR or microwave frequencies.

The particle size dependence of $\epsilon_1(\omega)$ and the corresponding $\sigma_1(\omega)$ are shown in Figures 4.2 and 4.3, respectively. Notice that the small particle conductivity follows a ω^2 dependence above the gap frequency and a small particle has intrinsically poor ac conductivity which resembles exactly the three-dimensional Anderson insulator!⁵⁹

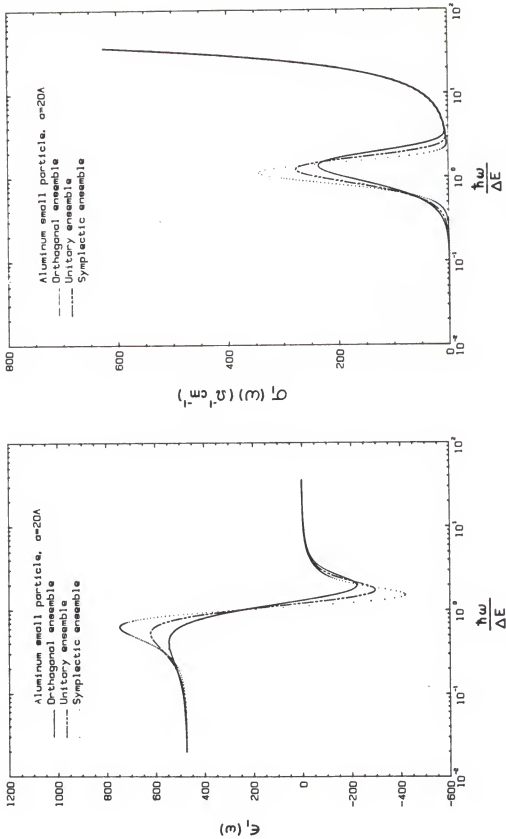


Figure 4.1 General frequency dependence of $\epsilon_1(\omega)$ and $\sigma_1(\omega)$ near the gap for a 20 Å aluminum small particle

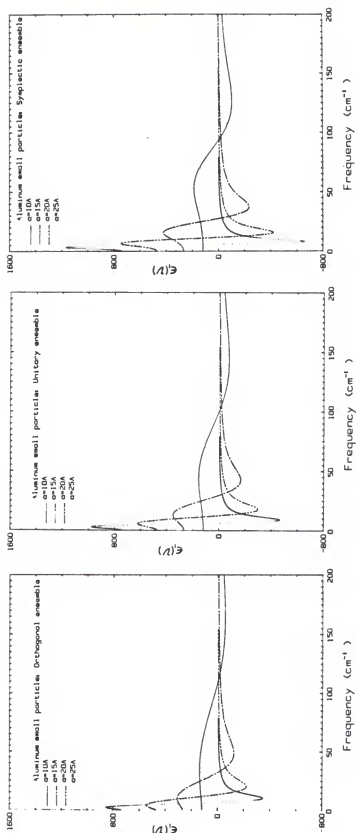


Figure 4.2 Particle size dependence of $\epsilon_1(\nu)$ for three different ensembles

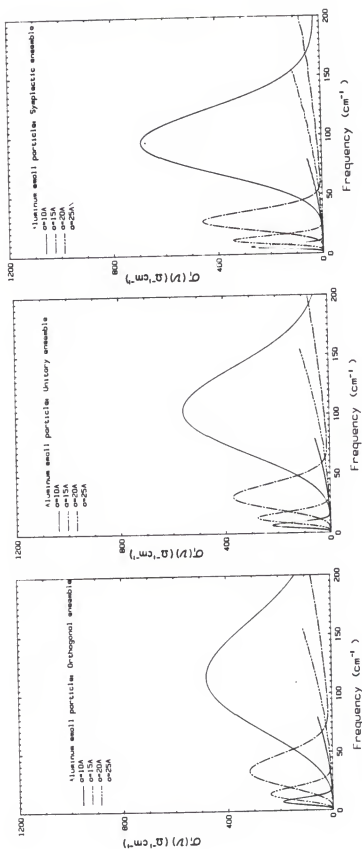


Figure 4.3 Particle size dependence on $\sigma_1(v)$ for three different ensembles

Additionally, a comparison among $a = 20 \text{ \AA}$ Al, Au, and Sn small particles for three different ensembles is made in Figures 4.4 and 4.5 for $\epsilon_1(\omega)$ and $\sigma_1(\omega)$, respectively.

Gor'kov and Eliashberg Theory

Gor'kov and Eliashberg (GE)¹⁷ applied the idea of energy level correlation in a random system to the small particle problem and obtained the electric susceptibility, χ_e , by evaluating the expectation value of the electric dipole moment operator, $\vec{d} = e\vec{r}$, directly as

$$\langle \vec{d} \rangle = \langle e\vec{r} \rangle = V \chi_e \langle \vec{E} \rangle \quad (4.80)$$

with a perturbation $H_1 = -\vec{d} \cdot \vec{E}$. By using the same approximation used in the general theory review section of this chapter, we find the electric susceptibility as

$$\chi_e |\vec{E}|^2 = \langle \vec{d} \rangle \cdot \vec{E} / V \quad (4.81)$$

$$= \left\{ -\frac{e^2}{V} \sum_{ij} \frac{(f_i - f_j) |\vec{r}_{ij}|^2}{E_{ij} - \hbar\omega - i\eta} \right\} |\vec{E}|^2 \quad (4.82)$$

Therefore, from

$$\epsilon(\omega) \vec{E} = (1 + 4\pi\chi_e) \vec{E} \quad (4.83)$$

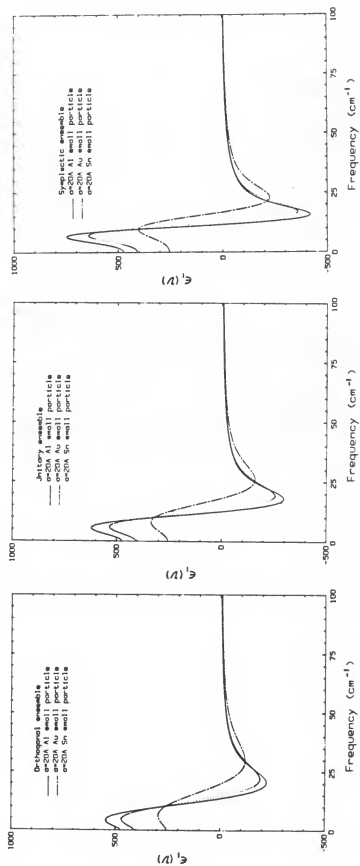
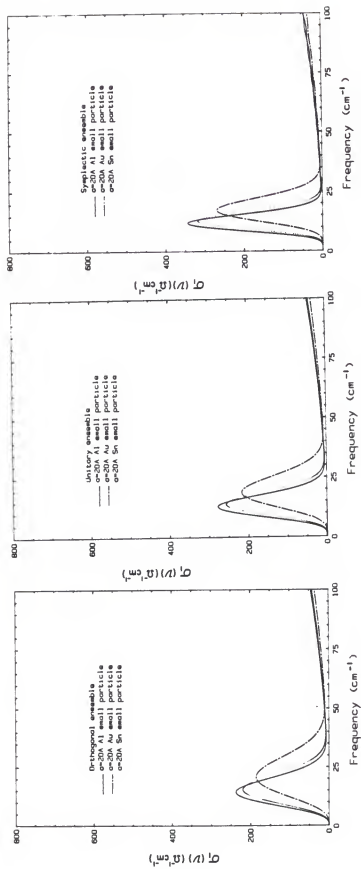


Figure 4.4 $\epsilon_1(\nu)$ for different types of metal small particles for three different ensembles

Figure 4.5 $\sigma_1(\nu)$ for Al, Au, and Ag small particles for different ensembles

we find

$$\epsilon(\omega) = 1 - \frac{4\pi e^2}{V} \sum_{ij} \frac{(f_i - f_j) |\vec{r}_{ij}|^2}{E_{ij} - \hbar\omega - i\eta} \quad (4.84)$$

which is essentially the same as Equation (4.51). At this point, GE applied the two-level correlation function, $R(\omega)$, conjectured by Dyson⁶ to change the summation to an integration after separating $\epsilon(\omega)$ into static and dynamic parts and found

$$\chi_e^{GE}(\omega) = \chi_0^{GE} + QA(\omega) \quad (4.85)$$

where

$$\chi_0^{GE} = \frac{\gamma k_F a_0}{5\pi^2} \left(\frac{a}{a_0} \right)^2 \quad \text{and} \quad Q = \frac{139}{1200 \pi^2} \frac{\gamma}{k_F a_0}$$

Here the function $A(\omega)$ is defined as

$$A(\omega) = (\hbar\omega)^2 v(E_F) \int_{-\infty}^{\infty} \frac{R(E) dE}{E^2 - (\hbar\omega + i\eta)^2} \quad (4.86)$$

Note that the real part of $A(\omega)$ is identical to the dimensionless function $F(\omega)$ introduced in Equation (4.75). The imaginary part of $A(\omega)$ can be found as

$$A_2^{\text{ort}}(x) = 2x - \frac{2 \sin^2 x}{x} + (2x) \left\{ \text{Si}(x) - \frac{\pi}{2} \right\} \frac{d}{dx} \left(\frac{\sin x}{x} \right) \quad (4.86a)$$

$$= (2x) R^{\text{ort}}(x) \quad (4.86b)$$

$$A_2^{\text{unit}}(x) = 2x - \frac{2 \sin^2 x}{x} \quad (4.87a)$$

$$= (2x) R^{\text{unit}}(x) \quad (4.87b)$$

and

$$A_2^{\text{symp1}}(y) = y - \frac{\sin^2 y}{y} + y \text{Si}(y) \frac{d}{dy} \left(\frac{\sin y}{y} \right) \quad (4.88a)$$

$$= y R^{\text{symp1}}(y) \quad (4.88b)$$

where $y = 2x = \frac{2\pi\hbar\omega}{E}$ and $A(\omega) = A_1(\omega) + iA_2(\omega)$.

Therefore, we have

$$\sigma_1(\omega) = Q A_2(\omega) \quad (4.89)$$

and

$$\epsilon_1(\omega) = 1 + 4\pi\chi_0^{\text{GE}} + 4\pi Q A_1(\omega) \quad (4.90)$$

GE results given by Equations (4.89) and (4.90) are shown in Figure 4.6. Note that Equation (4.90) does not have the correct physical description in a sense that the static part of the electric

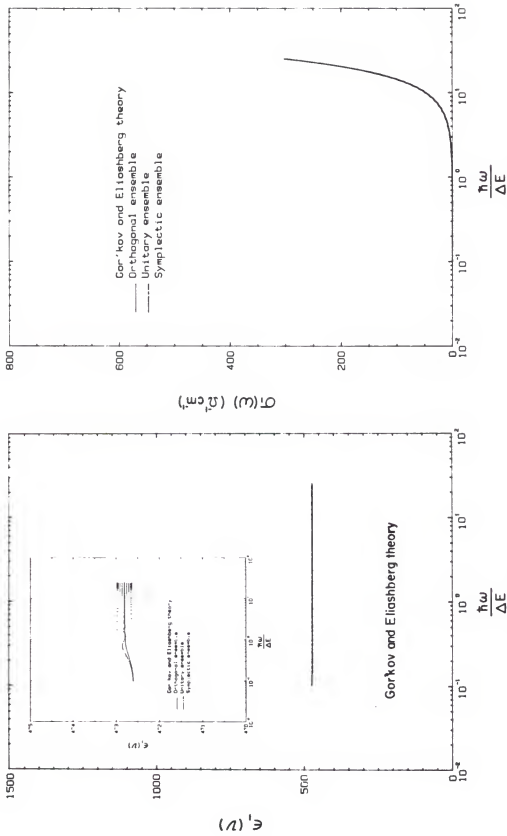


Figure 4.6 $\epsilon_1(\omega)$ and $\sigma_1(\omega)$ of Gorkov and Eliashberg theory; note that the small insert in $\epsilon_1(\omega)$ plot shows the oscillatory nature arising from the two level correlation

remains unchanged as frequency increases across the gap. Also, notice, therefore, that $\sigma_1(\omega)$ does not have the correct behavior across the gap. All these discrepancies are due to the lack of information about the diamagnetic current contribution in the induced dipole moment approximation. However, for the frequencies far below the gap, the GE theory qualitatively explains the electromagnetic properties of a small particle because the low frequency tail of the level correlation function $[R(E)]$ has the same behavior as the level distribution function $[P(E)]$.

High Frequency Limits

In the limit of high frequencies, we expect that the level correlation loses its meaning and the system can be treated in a quasi-continuum limit. However, the calculation of the position matrix elements with random surface potential (random superposition of individual atomic potential) is important because the origin of broadening has to come from the random nature of the surface. But, at the present time, no systematic method has been developed and research needs to be done on this problem in the future.

The Classical (Bulk) Limit

The $a \rightarrow \infty$ Limit

As the geometrical size of a particle increases, the average energy gap will approach zero and the cutoff frequency $\omega_c = v_F/a$ in the low frequency matrix elements will also become zero.

For the conductivity $\sigma_1(\omega)$, Equation (4.68) will become a delta function as $\Delta E \rightarrow 0$ from

$$\delta(x) = \lim_{n \rightarrow \infty} \frac{n}{\sqrt{\pi}} e^{-n^2 x^2} \quad (4.91)$$

This is the case of metal without relaxation as given by Equation (1.1). Also, $\epsilon_1(\omega)$ given by Equation (4.44) converges to

$$\lim_{\omega \rightarrow \infty} \epsilon_1(\omega) = 1 - \frac{\omega_p^2}{\omega^2} \quad (4.92)$$

as it should be in the bulk limit of electron gas without relaxation. The two limiting case of $\sigma_1(\omega)$ and $\epsilon_1(\omega)$ in our calculation is remarkable because Equations (4.68) and (4.44) show the correct behavior unlike the GE calculation.

Now, if there exists a finite electron mean free path (ℓ), a small particle is expected to recover the classical (Drude) conductivity from the small particle conductivity as the size of a particle exceeds the electron mean free path. To make this argument more transparent, the position matrix elements need to be reexamined in this limit. Because there exist random scattering centers for electrons (or electrons have a finite lifetime, $\tau = \ell/v_F$), an exponentially decaying behavior in the correlation function may be assumed. Thus, the electron position correlation function given by Equation (4.31) can be rewritten as

$$\langle \vec{r}(t) \vec{r}(t + t') \rangle_i = \sum_{\ell} |\langle i | \vec{r}(0) | \ell \rangle|^2 e^{-|t'|/\tau} \quad (4.93)$$

Hence, the position matrix element can be calculated from Equation (4.33) to give

$$|\vec{r}_{ij}|^2 = \frac{1}{\pi \hbar \nu(E_F)} \frac{\tau}{1 + (\omega_{ij}\tau)^2} \cdot \frac{1}{\hbar \omega} \sum_{\ell} (E_i - E_{\ell}) |<i|\vec{r}(0)|\ell>|^2 \quad (4.94a)$$

$$= - \frac{1}{2\pi m \nu(E_F)} \frac{\tau}{\omega [1 + (\omega_{ij}\tau)^2]} \quad (4.94b)$$

where $\sum_{\ell} (E_i - E_{\ell}) |<i|\vec{r}(0)|\ell>|^2 = - \frac{\hbar^2}{2m}$ and $E_i - E_{\ell} \sim \hbar \omega$ have been used.

Therefore, the Drude conductivity can be recovered by rearranging Equation (4.42) in terms of the absorption and emission of radiation parts such as

$$\sigma_1(\omega) = \frac{\pi e^2 \omega}{V} \sum_{i,j} f_i |\vec{r}_{ij}|^2 [\delta(E_{ij} + \hbar \omega) - \delta(E_{ij} - \hbar \omega)] \quad (4.95)$$

and by changing the summation about j to integral as

$$\sum_j \rightarrow \hbar \nu(E_F) \int_{-\infty}^{\infty} d\omega \quad (4.96)$$

we have

$$\sigma_1(\omega) = \frac{e^2}{2mV} \sum_i f_i \int_{-\infty}^{\infty} d\omega \frac{\tau}{1 + (\omega_{ij}\tau)^2} \left[\frac{\omega_{ji}}{\omega} \right] [\delta(\omega_{ij} + \omega) - \delta(\omega_{ij} - \omega)] \quad (4.97a)$$

$$= \frac{ne^2\tau}{m} \frac{1}{1 + (\omega\tau)^2} \quad (4.97b)$$

where $\sum_i f_i = N_e$, $n = N_e/V$, and $\omega_{ij} \equiv E_{ij}/\hbar$ (Q.E.D.).

The $\omega \rightarrow \infty$ Limit

For high frequencies, we also expect to recover the classical result for $\epsilon_1(\omega)$ because the quasi-continuum limit sets in. Thus, from Equation (4.44), we have

$$\epsilon_1(\omega) = 1 - \frac{\omega_p^2}{\omega^2} + \frac{1}{(\hbar\omega)^4} \frac{8\pi e^2}{V} \sum_{ij} f_i E_{ij}^3 |\vec{r}_{ij}|^2 + O(\omega^{-6}) \quad (4.98)$$

for the high frequency limit. Therefore,

$$\lim_{\omega \rightarrow \infty} \epsilon_1(\omega) = 1 - \frac{\omega_p^2}{\omega^2} \quad (4.99)$$

as expected.

The Small Particle Problem

Anomalous FIR Absorption

The FIR absorption coefficients of $a = 20 \text{ \AA}$ Al and Au small particles calculated from our small particle model are shown in Figure 4.7 for three different ensembles. Notice that our calculation clearly shows the effect of energy gap distributed by the level distribution function on the FIR absorption coefficient. In other words, the "visibility" of the quantum size effect in the FIR frequency is enhanced due to the level distribution. Also, the effect of magnetic field is found to be observable as a result of breaking the time reversal symmetry which changes the ensemble of energy levels from orthogonal to unitary ensemble.

In actual experimental situations, there exists a particle size distribution⁶⁰ as an inevitable factor, which is expected to broaden the measured absorption coefficient. The effect of size distribution on the FIR absorption coefficient is shown in Figure 4.8, along with the absorption coefficient of individual ensemble members. Also, the effect of the size distribution on the FIR absorption for three different ensembles is shown in Figure 4.9, while the detailed particle size dependence of the FIR absorption coefficient is shown in Figures 4.10, 4.11, and 4.12 for each ensemble. Notice that the frequency dependence of the FIR absorption coefficient is not quadratic any more for the frequencies away from the gap frequency because $\sigma_2(\omega)$ defined as $\sigma_2(\omega) = \{1 - \omega\epsilon_1(\omega)\}/4\pi$ becomes much smaller than $\sigma_1(\omega)$ in magnitude as frequency increases above the gap unlike the GE case and

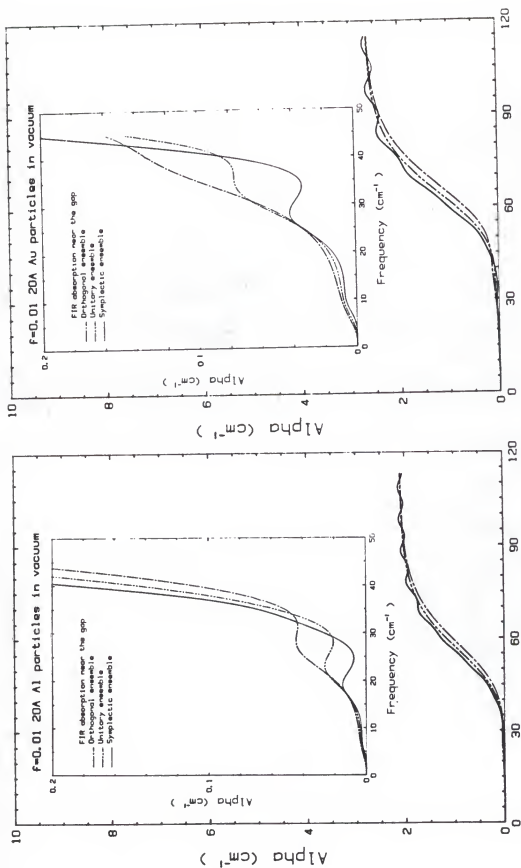


Figure 4.7 FIR absorption coefficients of 20 Å size Al and Au particles for three different ensembles

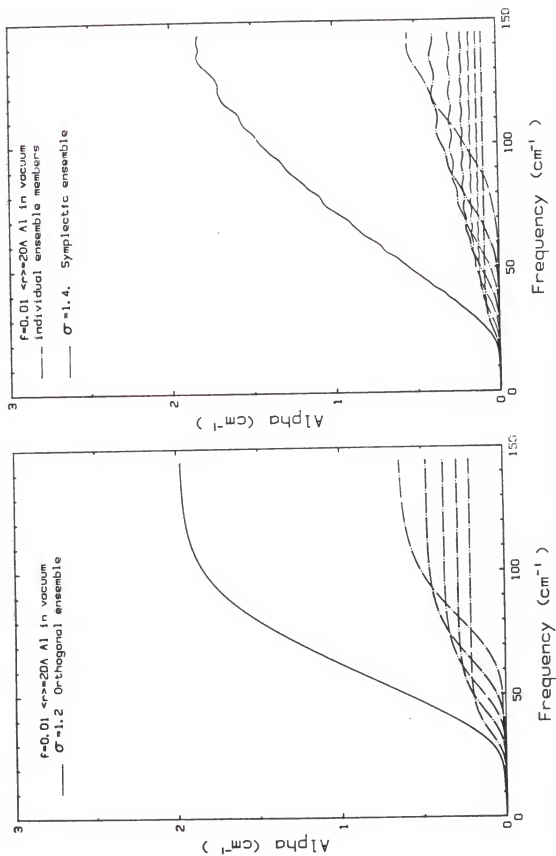


Figure 4.8 Details of the size distribution effect on 20 Å Al small particles with the geometrical standard deviation 1.2

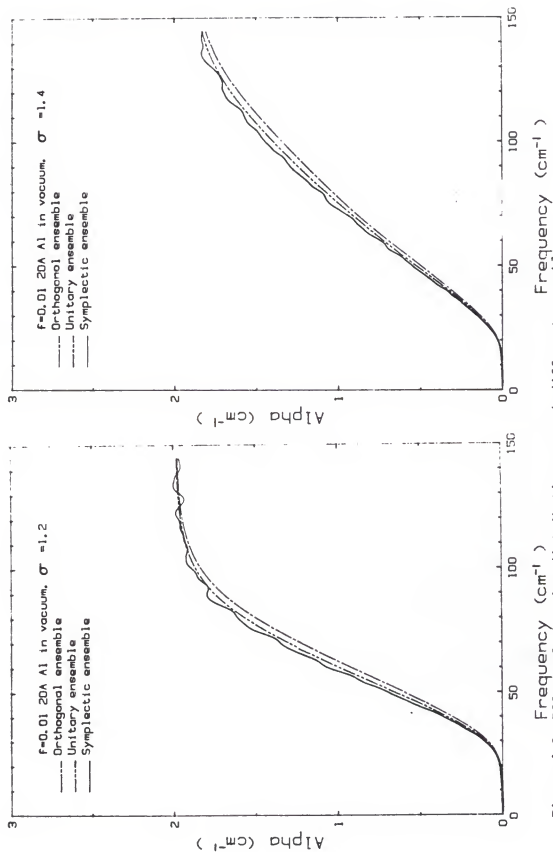


Figure 4.9 Effect of the size distribution on each different ensemble

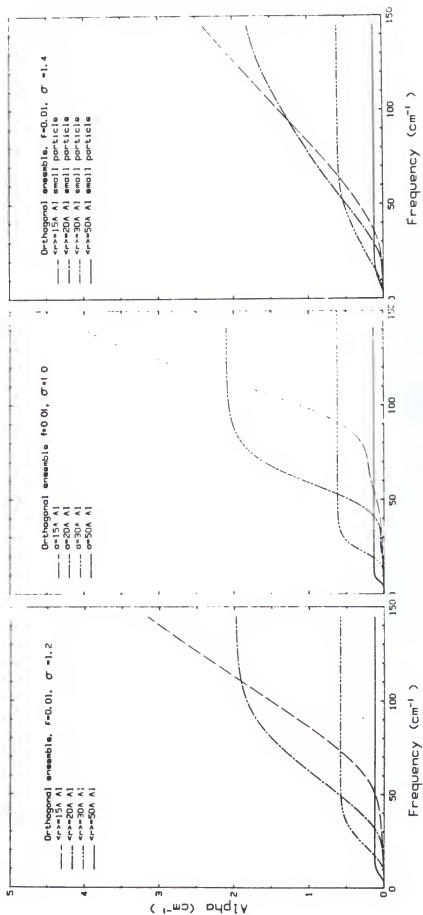


Figure 4.10 Size dependence of the FIR absorption coefficient for Orthogonal ensemble

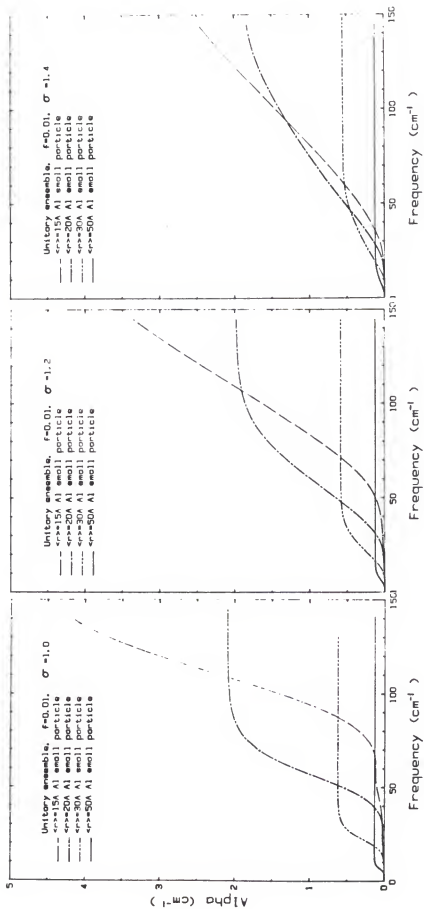


Figure 4.11 Size dependence of the FIR absorption coefficient for Unitary ensemble

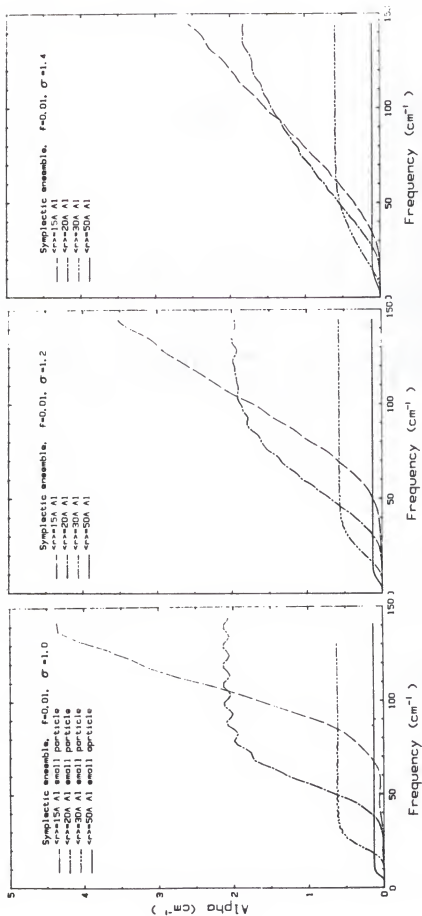


Figure 4.12 Size dependence of the FIR absorption coefficient for Symplectic ensemble

the absorption coefficient is sensitive to both $\sigma_1(\omega)$ and $\sigma_2(\omega)$ as can be seen from

$$\alpha_e \sim f\epsilon_0^{3/2} \left\{ \frac{\sigma_1}{\sigma_1^2 + \sigma_2^2} \right\} \omega^2 \quad (4.100)$$

and

$$\alpha_m \sim f\epsilon_0^{1/2} \sigma_1 a^2 \omega^2 \quad (4.101)$$

where α_e (α_m) is the classical result for the electric (magnetic) dipole absorption coefficient discussed in Chapter I.

However, the quadratic nature in frequency dependence in $\sigma_1(\omega)$ is expected to change to $\omega^{1/3}$ dependence above the gap like the normal Anderson insulator above the crossover frequency (see Appendix E). This effect can be put in phenomenologically by introducing the semiclassical approach⁴⁹ with a proper prescription because introducing arbitrary broadening does not conserve the local electron number.

For large size particles, the magnetic dipole contribution can be important as discussed in Chapter I. But, Equation (4.101) totally depends on a classical argument. Therefore, it is necessary to go to the multipole calculation beyond the dipole approximation in order to have the quantum mechanical justification. However, if we use Equation (4.101) to describe higher order effect ($\lambda = 1$) as a good approximation, we have additional ω^4 contribution to the absorption as shown in Figures 4.13, 4.14, and 4.15 and this additional contribution changes the shape of the absorption coefficient significantly for large

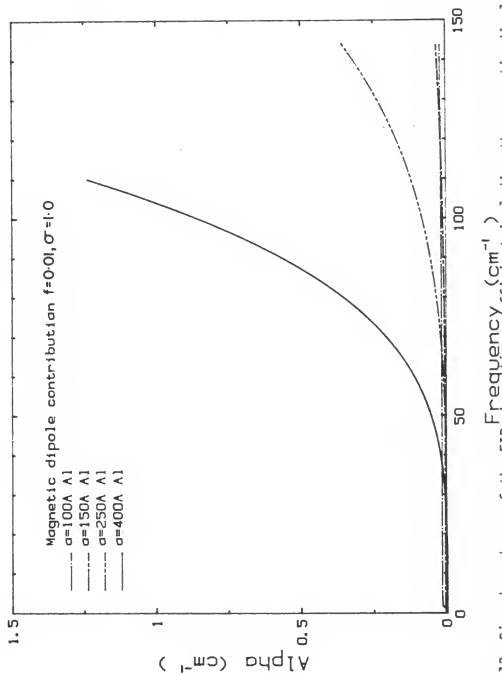


Figure 4.13 Size dependence of the FIR absorption coefficient including the magnetic dipole contribution for the geometrical standard deviation 1.0

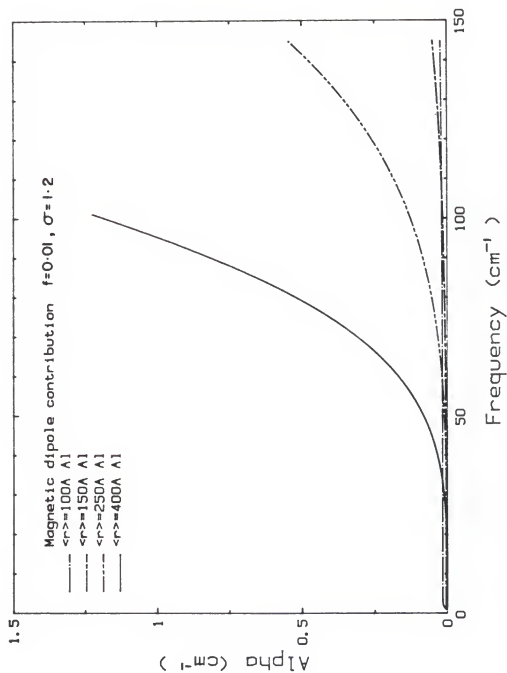


Figure 4.14 Size dependence of the FIR absorption coefficient including the magnetic dipole contribution for the geometrical standard deviation 1.2

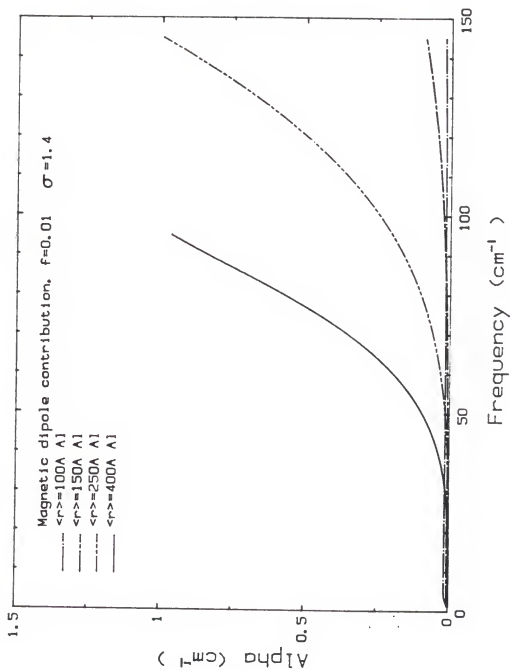


Figure 4.15 Size dependence of the FIR absorption coefficient including the magnetic dipole contribution for the geometrical standard deviation 1.4

size particles. But, the magnitude of absorption for large particles is still much smaller than the experimental results shown in Chapter III and the frequency dependence is not correct. This discrepancy is perhaps due to the incompleteness of the theory. Especially, the approximation given by Equation (4.37) requires more theoretical speculation because we totally excluded the frequency dependence on the position matrix elements in the approximation.

Therefore, we will restrict the theoretical speculation on the FIR problem for frequencies much smaller than the cutoff frequency, v_F/a . Now, for small frequencies, we can examine purely particle size independent response by rescaling $\chi_e(\omega)$ and $\sigma_1(\omega)$ given by Equations (4.59) and (4.68), respectively, as

$$\tilde{\chi}_e(\omega) = \chi_e(\omega)/\chi_e^0 = -\frac{\tilde{\sigma}_2(\omega)}{\omega} \quad (4.102)$$

and

$$\tilde{\sigma}_1(\omega) = \sigma_1(\omega)/\chi_e^0 \quad (4.103)$$

Therefore, we have a scaled FIR absorption coefficient, which is particle size independent as

$$\tilde{\alpha}(\omega) = \frac{1}{\epsilon} \cdot \frac{\Delta E}{\hbar} \cdot \chi_e^0 \alpha(\omega) \quad (4.104)$$

and the graphs of $\tilde{\alpha}(\omega)$ for the three different ensembles are shown in Figure 4.16.

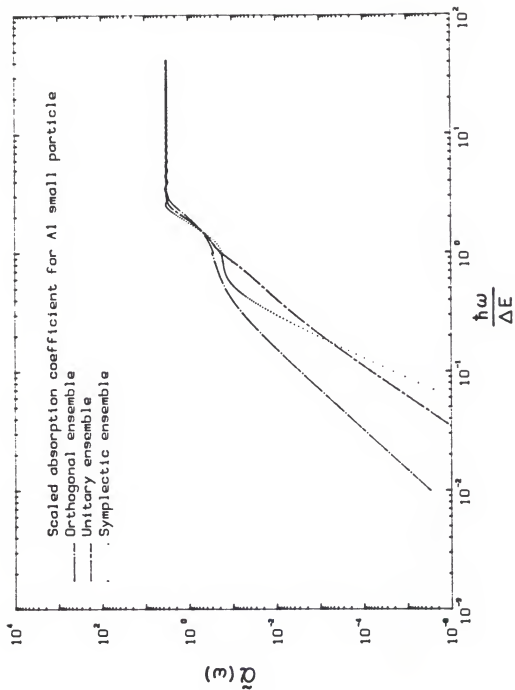


Figure 4.16 Normalized FIR absorption coefficient to three different ensembles

In summary, the "anomalous" FIR absorption is truly a quantum size effect resulting from the broken symmetry. And this effect can be observed experimentally in FIR frequencies for small particles and microwave frequencies for large particles (i.e., the experimental test purely depends on the size quantization gap). However, the extension to higher frequencies to explain the experimental results for an order of 100 Å particles fails mainly because of the incomplete approximation in the matrix element calculation.

Surface Plasmon Broadening

As shown in Table 1.1 in Chapter I, a significant broadening in the Maxwell-Garnett (or Mie) resonance peak has been observed experimentally which does not count on either classical calculation or Kawabata-Kubo calculation. In addition, a weak temperature dependence of the resonance strength and width⁸⁴ which does not seem to arise obviously in classical theory.

A general description of the Maxwell-Garnett resonance can be obtained from Equation (1.23) as

$$\alpha(\omega) = f \frac{4\pi\omega}{c} \sqrt{\epsilon_0} \operatorname{Im} \gamma_e(\omega) \quad (4.105)$$

Here again, α is the absorption coefficient, f is the volume fraction of small particles in a medium with ϵ_0 , and γ_e is the electric polarizability per unit volume of a particle in a medium, ϵ_0 .

By separating the dielectric function of a small particle, $\epsilon_m(\omega)$ into real and imaginary parts as $\epsilon_m(\omega) = \epsilon_1 + i\epsilon_2$, we find

$$\operatorname{Im} \gamma_e(\omega) = \frac{9}{4\pi} \frac{\epsilon_0 \epsilon_2}{(\epsilon_1 + 2\epsilon_0)^2 + \epsilon_2^2} \quad (4.106)$$

from Equation (1.10). Therefore, the absorption coefficient becomes

$$\alpha(\omega) = f \frac{9\omega}{c} \epsilon_0^{3/2} \frac{\epsilon_2}{(\epsilon_1 + 2\epsilon_0)^2 + \epsilon_2^2} \quad (4.107)$$

Note that Equation (1.27) is the limiting case of Equation (4.107) in the limit of $\epsilon_0 \ll \epsilon_1$ for the electric dipole contribution only.

Now, in the vicinity of the resonance frequency ω_{sp} , which satisfies $\epsilon_1(\omega_{sp}) = -2\epsilon_0$, $\epsilon_1(\omega)$ can be expanded as

$$\epsilon_1(\omega) \sim \epsilon_1(\omega_{sp}) + \left. \frac{d\epsilon_1(\omega)}{d\omega} \right|_{\omega=\omega_{sp}} (\omega - \omega_{sp}) + \dots \quad (4.108)$$

because $\epsilon_1(\omega)$ varies slowly at high frequencies. Thus, we obtain $\alpha(\omega)$ near the resonance as

$$\alpha(\omega) = \frac{9\omega_{sp}}{c} f \epsilon_0^{3/2} \left[\frac{\epsilon_2(\omega_{sp})}{\Lambda^2 (\omega - \omega_{sp})^2 + \epsilon_2^2(\omega_{sp})} \right] \quad (4.109)$$

where

$$\Lambda \equiv \left. \frac{d\epsilon_1(\omega)}{d\omega} \right|_{\omega=\omega_{sp}}$$

From Equation (4.109), we can clearly see that the line width is determined by $\epsilon_2(\omega)$ and Λ and we, therefore, have the full width at half maximum, $\Delta\omega$, as

$$\Delta\omega = 2|\omega_{1/2} - \omega_{sp}| = \frac{2\epsilon_2(\omega_{sp})}{\Lambda} \quad (4.110)$$

Here $\omega_{1/2}$ stands for the frequency at half maximum. For example, $\Delta\omega$ of a Drude-like small particle becomes

$$(\Delta\omega)_{\text{Drude}} = \frac{1}{\tau} \left\{ 1 + \frac{1}{(\omega_{sp}\tau)^2} \right\} \quad (4.111)$$

$$\sim \frac{v_F}{a}$$

as found elsewhere.^{26,88,89}

However, the quantum mechanical calculation of $\Delta\omega$ for a sphere^{48,90} or a cube^{49,91,92} with the smooth surface gives $\Delta\omega$ close to the classical result within less than 20% variation except for the result of Kawabata and Kubo,⁴⁸ which gives $\frac{1}{2} \tau_{\text{classical}}$. Therefore, as briefly discussed before, the role of the surface roughness should be taken into account in order to explain the broadening observed in this work and in the work of others.

CHAPTER V SUMMARY AND CONCLUSION

Since the anomalous FIR absorption by small particles was discovered by Tanner,¹³ many efforts have been made to explain the peculiar phenomenon starting from how to take the average of the composite system (metal-insulator) and ending with clustering theories. In this dissertation, two major issues have been raised and studied extensively: One is the clustering theory and the other is the possibility of nonmetallic behavior of small particles.

For the first issue, we have demonstrated the experimental results of clustered and nonclustered small particle composite systems via direct FIR and MIR absorption measurements and the TEM studies and we have verified that the clustering effect does enhance the FIR absorption, but the anomalous FIR absorption observed in this experiment is truly a small particle phenomenon! In addition, unexpected new observations were made in the MIR frequency range, oxide contribution and substantially smaller MIR absorption coefficient. Also, the grinding effect study in the MIR range showed a clear evolution process from a clustered to a nonclustered system, which eventually shows the linear dependence in the volume fraction, f , on the absorption coefficient.

A test for the constant relaxation time of electrons in a small particle was made in order to verify the second issue, nonmetallic

possibility. Surprisingly, what we observed was the behavior of an insulator! In other words, the intrinsically poor conductivity of a small particle is responsible for the puzzling anomalous FIR absorption problem. This point stimulated the theoretical speculation on the fundamental properties of a small particle and we found the behavior of an insulator as discussed in Chapter IV. However, this theoretical attempt is far from the reality to explain all physical phenomena of small particles, which we have observed experimentally. Even so, we believe that our model calculation explains the correct behavior of a small particle near the gap frequency and we are on the right track. Hence, further extensive theoretical research needs to be done in the future to obtain the correct description of a small particle at high frequencies, which will also lead to the answer to the surface plasmon broadening problem.

The observation of the red-shifted interband transition and the possible "localized band" in aluminum small particles, which disappear in the bulk limit as shown in Appendix D, adds up to a new feature to the small particle problem.

In conclusion, the anomalous FIR absorption is arising from the intrinsic properties of a small particle, which cannot be explained by the classical theory and remains, therefore, unsolved. Also, a small particle is an insulator and it has a different energy band structure from its bulk state.

APPENDICES

APPENDIX A SURFACE ROUGHNESS

As described earlier in Chapter I, the roughness of the surface of a small particle to atomic scale plays a crucial role in breaking degeneracies of eigenstates and alters the static and dynamic properties of a small particle significantly.

If we model a small particle as a system of free electron gas confined in a sphere and treat the surface as a smooth and infinite potential barrier, then we can get all necessary information, in principle, by solving the Schrödinger equation.

$$H\phi_n(r) = \epsilon_n \phi_n(r) \quad (A.1)$$

where the solution $\phi_n(r)$ vanishes at the boundary. Therefore, the corresponding eigenvalues and eigenfunctions are found as follows:

$$\epsilon_{n\ell} = \frac{\hbar^2}{2m} \left(\frac{k_{n\ell}}{a} \right)^2 \quad (A.2)$$

and

$$\phi_{n\ell}(r) = c_{n\ell} j_\ell \left(k_{n\ell} \frac{r}{a} \right) \quad (A.3)$$

where a is the radius of the sphere, $j_\ell(r)$ is the ℓ^{th} order spherical Bessel's function, $k_{n\ell}$ is the zeros of $j_\ell(r)$, and $c_{n\ell}$ is the normalization constant.

Now, if we introduce the roughness to the smooth surface

$$H(r') \psi_n(r') = E_n \psi_n(r') \quad (\text{A.4})$$

and $\psi_n(r') = 0$ at the boundary. Here r' represents another coordinate for a new sphere with rough surface. If the degree of the roughness is not serious, we can treat the deviation from the perfect surface as a perturbation.⁹³ By considering one parameter mapping $r' \rightarrow r = r(r', \lambda)$ where r is an analytic function of λ and λ is the mapping parameter. Then, r can be expanded as

$$r = r' + \lambda \left(\frac{\partial r}{\partial \lambda} \right)_0 + \frac{\lambda^2}{2} \left(\frac{\partial^2 r}{\partial \lambda^2} \right)_0 + O(\lambda^3) \quad (\text{A.5})$$

and Jacobian (J) of the mapping becomes

$$J = \left| \frac{\partial r}{\partial r'} \right| = 1 + \lambda \left(\frac{\partial J}{\partial \lambda} \right)_0 + \frac{\lambda^2}{2} \left(\frac{\partial^2 J}{\partial \lambda^2} \right)_0 + O(\lambda^3) \quad (\text{A.6})$$

Thus, the Hamiltonian $H(r')$ can be expressed as follows:

$$\begin{aligned} H(r') &= H(r, \lambda) \\ &= H(r) + \lambda \left(\frac{\partial H}{\partial \lambda} \right)_0 + \frac{\lambda^2}{2} \left(\frac{\partial^2 H}{\partial \lambda^2} \right)_0 + O(\lambda^3) \end{aligned} \quad (\text{A.7})$$

with $H'(r, 0) = H(r)$.

Now, from Equation (A.4), a new Hamiltonian can be obtained such as

$$\bar{H}(r) \bar{\Psi}_n(r) = E_n \bar{\Psi}_n(r) \quad (A.8)$$

where $\bar{H}(r) = J^{-1/2} H(r') J^{1/2}$ and $\bar{\Psi}_n(r) = J^{-1/2} \Psi_n(r')$. Next, from Equations (A.6) and (A.7), we have

$$\bar{H}(r) = H(r) + \lambda H_1 + \frac{\lambda^2}{2} H_2 + O(\lambda^3) \quad (A.9a)$$

and

$$H_1 \equiv \left(\frac{\partial H'}{\partial \lambda} \right)_0 + \frac{1}{2} \left[H(r), \left(\frac{\partial J}{\partial \lambda} \right)_0 \right] \quad (A.9b)$$

$$\begin{aligned} H_2 \equiv & \left(\frac{\partial^2 H'}{\partial \lambda^2} \right)_0 + \left[\left(\frac{\partial H'}{\partial \lambda} \right)_0, \left(\frac{\partial J}{\partial \lambda} \right)_0 \right] + \frac{1}{2} \left[H(r), \left(\frac{\partial^2 J}{\partial \lambda^2} \right)_0 \right] \\ & + \frac{3}{2} \left(\frac{\partial^2 J}{\partial \lambda^2} \right)_0^2 H(r) - \frac{1}{4} H(r) \left(\frac{\partial^2 J}{\partial \lambda^2} \right)_0^2 \\ & - \frac{1}{2} \left(\frac{\partial J}{\partial \lambda} \right)_0 H(r) \left(\frac{\partial J}{\partial \lambda} \right)_0 \end{aligned} \quad (A.9c)$$

Therefore, by expanding $\bar{\Psi}_n(r)$ in powers of λ ,

$$\bar{\Psi}_n(r) = \phi_n(r) + \lambda \bar{\Psi}_n^{(1)} + \frac{\lambda^2}{2} \bar{\Psi}_n^{(2)} + O(\lambda^3) \quad (A.10)$$

and defining a similar expansion for E_n ,

$$E_n = \epsilon_n + \lambda E_n^{(1)} + \left(\frac{\lambda^2}{2} \right) E_n^{(2)} + O(\lambda^3) \quad (A.11)$$

we can apply a standard perturbation theory to get the correction terms.

For a simple case $r' = r(1 + \lambda)$, an easy justification of the perturbation treatment can be made by solving Equation (A.4) with the condition $\Psi_{n\ m}[a(1 + \lambda)] = 0$. By considering transformations,

$$\begin{aligned} r &= \left(\frac{1}{1 + \lambda} \right) r' \\ \theta &= \theta' \\ \phi &= \phi' \end{aligned} \tag{A.12}$$

then, the Jacobian for the transformation becomes

$$J = \frac{1}{1 + \lambda} = 1 - \lambda + \lambda^2 + \dots \tag{A.13}$$

Hence,

$$\begin{aligned} \bar{H} &= J^{-1/2} H\left((1 + \lambda) r, \theta, \phi\right) J^{1/2} \\ &= H(r, \theta, \phi) - 2\lambda H(r, \theta, \phi) + 3\lambda^2 H(r, \theta, \phi) \end{aligned} \tag{A.14}$$

and

$$\begin{aligned} E_n &= \epsilon_n + \lambda E_n^{(1)} + \frac{\lambda^2}{2} E_n^{(2)} + O(\lambda^3) \\ \bar{\Psi}_n &= \phi_n(r) + \lambda \bar{\Psi}_n^{(1)}(r) + \frac{\lambda^2}{2} \bar{\Psi}_n^{(2)}(r) + O(\lambda^3) \end{aligned} \tag{A.15}$$

Thus, we obtain

$$\lambda E_n^{(1)} = -2\lambda \varepsilon_{n\ell}, \quad \frac{\lambda^2}{2} E_n^{(2)} = 3\lambda^2 \varepsilon_{n\ell} \quad (\text{A.16})$$

where $\varepsilon_{n\ell}$ is given in Equation (A.2). And

$$\bar{\Psi}_n^{(1)} = - \sum_{m \neq n} \left[\frac{\phi_m^* H_1 \phi_n d^3 r}{\varepsilon_m - \varepsilon_n} \right] \phi_m = 0 \quad (\text{A.17})$$

and

$$\begin{aligned} \bar{\Psi}_n^{(2)} = \sum_{m \neq n} \left[\phi_m^* (H_1 - E_n^{(1)}) \bar{\Psi}_n^{(1)} d^3 r \right. \\ \left. + \int \phi_m^* (H_2 - E_n^{(2)}) \phi_n d^3 r \right] \frac{\phi_m}{E_n - E_m} = 0 \end{aligned} \quad (\text{A.18})$$

due to the orthogonality of the unperturbed eigenfunction ϕ_n given in Equation (A.3).

Now, let's consider the exact solution. The eigenfunction $\Psi(r')$ can be written as

$$\Psi(r') = c'_{n\ell} j_\ell \left(k_{\ell n} \frac{r'}{(a + \lambda)} \right) \quad (\text{A.19})$$

with eigenvalue

$$E_{n\ell} = \frac{\hbar^2}{2m} \left(\frac{k_{\ell n}}{(a + \lambda)} \right)^2 \quad (\text{A.20})$$

From Equation (A.8),

$$\Psi_n(r') = j^{1/2} \bar{\Psi}_n(r) \quad (\text{A.21})$$

therefore,

$$\Psi_n(r') = c_{n\ell} \left[1 - \frac{\lambda}{2} + \frac{3}{8} \frac{\lambda}{a} \right]^2 j_\ell \left[k_{\ell n} \left\{ 1 - \lambda + \lambda^2 \right\} \frac{r'}{a} \right] \quad (\text{A.22})$$

which agrees with Equation (A.19) to the second order with

$$c'_{n\ell} = c_{n\ell} \left[1 - \frac{\lambda}{2} + \frac{3}{8} \lambda^2 \right] \quad (\text{A.23})$$

Tavel⁹⁴ carried out a detailed perturbation calculation for a mapping

$$r' = r[1 + \lambda f(\theta, \phi)] \quad (\text{A.24})$$

$$\theta' = \theta$$

$$\phi' = \phi$$

and by expressing the surface perturbation $\lambda f(\theta, \phi)$ in the most general form

$$\lambda f(\theta, \phi) = \lambda \sum_{\ell=1}^{\infty} \sum_{m=-\ell}^{\ell} \left[a_{\ell m} (Y_{\ell m} + Y_{\ell m}^*) + i b_{\ell m} (Y_{\ell m} - Y_{\ell m}^*) \right] \quad (\text{A.25})$$

where $Y_{\ell m}$ are the spherical harmonics and each of the coefficients $a_{\ell m}$ and $b_{\ell m}$ is chosen from uncorrelated Gaussian distributions with zero

mean and unit standard deviation, following important results are found in this model, after a tremendous amount of calculation:

1. There is an upper limit to the value of ℓ which can break the degeneracy of any given level. In this model, $\ell_{\max} = 13$. Therefore, each surface in the ensemble gives rise to a 27×27 matrix and only spherical harmonics up to the 26^{th} order in the surface perturbation contribute to the level splitting from the Wigner-Eckart theorem.
2. The degree of roughness can be varied by multiplying the harmonic coefficients by inverse powers of ℓ to damp out the contributions of higher order spherical harmonics. For the maximally rough case (ℓ^{-1} damping with $\lambda = 0.6$), a distribution of level spacings which agrees with the Wigner distribution is obtained, thus supporting the applicability of the random matrix theory.
3. There is a significant correlation between the eigenvalues, regardless of their particular symmetry, even though the matrix element themselves are chosen to be uncorrelated. This correlation reflects the consequence of the level repulsion predicted by Wigner.
4. As the degree of the roughness decreases, a significant change occurs in the level distribution which is rather close to the level attraction case.

Although this model calculation is an idealized case and does not describe the realistic small particle surface, the idea of correlation arising from the random irregularity of the surface would be feasible and there is no doubt about the necessity of new classes of ensemble which can describe the level correlation and its distribution in a small particle.

-

APPENDIX B LEVEL STATISTICS

Kubo⁴ suggested that the effect of random surface irregularities of a small particle randomize the distribution of energy levels and the author took the adjacent energy gap distribution to be a Poisson distribution

$$p(\epsilon) = \frac{e^{-\epsilon/\Delta E}}{\Delta E} \quad (\text{B.1})$$

where ϵ is the energy level spacing and ΔE is the average spacing.

Gor'kov and Eliashberg⁷ discussed the effect of level repulsion between two crossing eigenvalues by employing the random matrix theory introduced first by Wigner⁹⁵ and developed further by Dyson,⁹⁶ which had proven to be quite realistic in describing excited nuclear states.

Because the eigenvalues of the nuclear Hamiltonian are essentially unknown due to the extensive energy level configuration mixing and there exists a well-established connection between the spacing distribution of adjacent eigenvalues of a matrix with random chosen elements and the level spacing distribution of excited nuclear states, it is a logical conclusion to make the same analogy to a small particle whose Hamiltonian describing electrons in the particle is not known due to some complex interactions between electrons and the impurities and irregularities of the surface.

Wigner first made a statistical hypothesis that all matrix elements H_{mn} of a system having N energy levels are statistically independent and satisfies the equal a priori condition. However, one cannot define a uniform probability distribution on an infinite range and this problem can be avoided by introducing a cutoff into the theory which could correspond to excluding the strong interactions in the nuclear theory. The best description of such a system is the Gaussian distribution

$$P(H) = A \exp \left[- \sum_{m,n}^N \left| \frac{H_{mn}}{\Lambda^2} \right|^2 \right] \quad (B.2)$$

where Λ is the cutoff excluding the divergence.

Later, Dyson conjectured that it is impossible to define an ensemble in terms of the H_{mn} in which all interactions are equally probable and the requirement of the cutoff was imposed without clear physical motivation. Also, the author pointed out that it is not reasonable to picture the H_{mn} as resulting from some random process of a conventional statistical ensemble.

In the phenomenological Dyson theory,⁹⁶ the Hamiltonian matrix element description was rejected and a unitary $N \times N$ matrix S which is related to the Hamiltonian of the system in a complicated way was considered. According to Dyson's hypothesis, the correlation of n consecutive energy levels of a system ($n \ll N$) is statistically equivalent to that in the ensemble of n consecutive angles θ_i on the

unit circle. The connection between S and H is left to be vague to reality, but a definite relation, for example, may be considered such as

$$S = \exp [iH], \quad S = \frac{1 + iH}{1 - iH} \quad (B.3)$$

and S can be diagonalized in terms of a unitary matrix U as follows:

$$S^0 = U^\dagger S U \quad (B.4)$$

with $(S^0)_{ij} = \delta_{ij} e^{i\theta_i}$ and $U^\dagger U = 1$.

Now, the unitary matrix S can have a definite mathematical symmetry which depends on the existing symmetries in the real system.

If the Hamiltonians have time reversal and spin rotation invariant symmetry, then all wave function can be made to be real. Thus, all the matrix elements of the Hamiltonian are real in this case and an ensemble of such Hamiltonian is invariant under orthogonal transformation (i.e., Hamiltonian of a system with even electron spins and zero external magnetic field). The matrix S has the same symmetry as H which is obvious from Equation (B.3). Therefore, now Equation (B.4) can be made to be real and U takes the form

$$U U^T = 1 \quad (B.5)$$

where U is a real matrix.

When the time reversal invariant symmetry is broken, the matrix elements of H can no longer be real. Then the unitary matrix S does not

have any additional symmetry. Therefore, U is now an arbitrary unitary matrix and this symmetry is suitable for the system in the presence of a magnetic field. The third possible class of symmetry is the symplectic case that a system has the time reversal symmetry, but has no rotational symmetry (i.e., a system with odd number electron spins in a zero magnet field or one-electron Hamiltonian with strong spin orbit coupling in a zero magnetic field). Thus, all levels in the system have Kramer's doublets due to spin-orbit interactions (i.e., the spin and the orbital states are inseparably coupled together), and each eigenvalue of S has to appear twice.

Now the concept of equal probabilities for all matrix elements of S in calculating the average implies an equal contribution of each elementary volume ΔS on the hypersurface $\{S\}$. In terms of the coordinates θ_i and U , the elementary area $(dL)^2$ becomes

$$(dL)^2 = \text{Tr}(dS dS^\dagger) \quad (\text{B.6})$$

Now, from

$$dS = U^\dagger S^0 \delta U + \delta U^\dagger S^0 U + U^\dagger (i d\theta_i) U \quad (\text{B.7})$$

we obtain,

$$(dL)^2 = 2\text{Tr} (S^0 \delta U \delta U^\dagger S^{0\dagger} - \delta U S^{0\dagger} \delta U^\dagger S^0) + \sum_i (d\theta_i)^2 \quad (\text{B.8})$$

where the property $\delta U U^\dagger = -U \delta U^\dagger$ have been used. Equation (B.8) can also be written as

$$(dL)^2 = \sum_{i,j}^N (\delta U_{ij} \delta U_{ij}^+) \left| 2 \sin \frac{1}{2} (\theta_i - \theta_j) \right| + \sum_i (d\theta_i)^2 \quad (\text{B.9})$$

by using

$$(S^0 S^{0+})_{ij} = e^{i(\theta_i - \theta_j)/2}$$

Thus,

$$(dL)^2 = \sum_{i,j}^N (\delta U_{ij} \delta U_{ij}^+) \left| e^{i\theta_i} - e^{i\theta_j} \right| + \sum_i (d\theta_i)^2 \quad (\text{B.10})$$

The volume element ΔS can be calculated by considering the off diagonal elements such as

$$\Delta S_{\text{orth}} = \prod_{i < j} \left| e^{i\theta_i} - e^{i\theta_j} \right| \prod_i d\theta_i \Delta U \quad (\text{B.11})$$

where ΔU is the volume element of vector δU_{ij} . Therefore, the probability of finding a system of orthozonal group belongs to the volume of ΔS is

$$p(\Delta S) = \frac{1}{V} \Delta S \quad (\text{B.12})$$

where $V = \int_S \Delta S$, is the total volume. For unitary the ensemble case, since all the elements of the Hamiltonian are not real, there are three independent variables for two adjacent level Hamiltonians by choosing

the off-diagonal term a_{12} to be $a_{12}' + ia_{12}''$. Consequently, we have to consider a transformation

$$U \rightarrow GU \quad (B.13)$$

if G is the diagonal unitary matrix with $(G)_i = \delta_{ij} e^{i\tau_j}$ where τ_j are an arbitrary angle on a unit circle. Therefore, the total volume element in this group will be

$$\Delta S_{\text{unit}} = \Delta S_{\text{orth}} \Delta G$$

and (B.14)

$$\Delta G = \prod_j d\tau_j = \prod_{i < j} \left| e^{i\theta_i} - e^{i\theta_j} \right|$$

thus,

$$\Delta S_{\text{unit}} = \prod_{i < j} \left| e^{i\theta_i} - e^{i\theta_j} \right|^2 \prod_i d\theta_i \Delta U \quad (B.15)$$

Now, for the symplectic ensemble case, we have a Hamiltonian consisting of quaternoions. In other words, we have two more random variables in the eigenvalue of the Hamiltonian; therefore, two more volume elements have to be considered because the unitary matrix U is also symplectic.

$$\Delta S_{\text{symol}} = \prod_{i < j} \left| e^{i\theta_i} - e^{i\theta_j} \right|^4 \prod_i d\theta_i \Delta U \quad (B.16)$$

with $\Delta G = \prod_{\alpha, j} d\tau_j^\alpha$, $\alpha = 1, 2, 3$.

A constant density of states can be calculated from the probability distribution because it depends only on the differences of θ_i and θ_j .

The next interesting quantity is the two-level correlation function, which determines the probability that a level falls in an energy interval ϵ from another level. Dyson⁶ calculated the following correlation functions for three different ensembles:

$$R^{\text{ort}}(x) = 1 - \frac{\sin^2 x}{x^2} - \left(\int_1^\infty \frac{\sin xt}{t} dt \right) \frac{d}{dx} \left(\frac{\sin x}{x} \right) \quad (\text{B.17})$$

for the orthogonal ensemble,

$$R^{\text{unit}}(x) = 1 - \frac{\sin^2 x}{x^2} \quad (\text{B.18})$$

for the unitary ensemble, and

$$R^{\text{symp1}}(x) = 1 - \frac{\sin^2 x}{x^2} + \left(\int_0^1 \frac{\sin xt}{t} dt \right) \frac{d}{dx} \left(\frac{\sin x}{x} \right) \quad (\text{B.19})$$

for the symplectic ensemble. Here $x = \frac{\pi \epsilon}{\Delta E}$, ΔE is the average level spacing. The detailed behavior of $R(x)$ is shown in Figure B.1.

Notice that the two-level correlation function has essentially the same behavior as the pair correlation function of identical hard spheres with the radius ΔE . However, these correlation functions have completely different limiting cases⁶ as

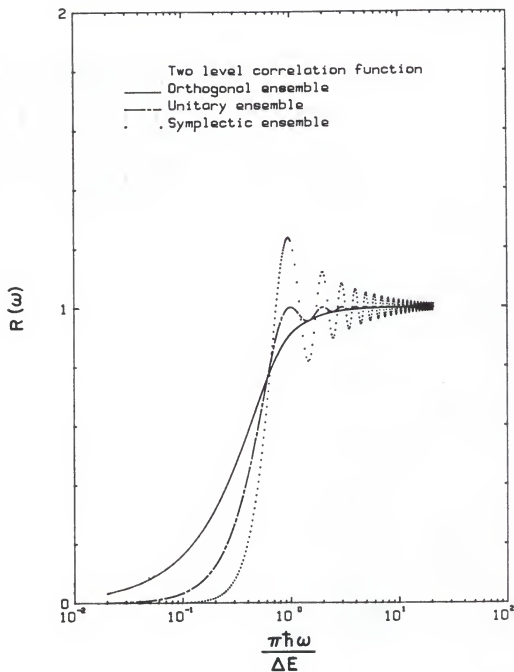


Figure B.1 Two level correlation function for three different ensembles

$$R^{\text{ort}}(x) \rightarrow \frac{\pi}{6} x, \quad x \rightarrow 0, \quad \text{and} \quad 1 - \frac{1}{x^2} + \frac{1}{x^4} (1 + \cos^2 x), \quad x \rightarrow \infty \quad (\text{B.20})$$

$$R^{\text{unit}}(x) \rightarrow \frac{x^2}{3}, \quad x \rightarrow 0, \quad \text{and} \quad 1 - \frac{\sin^2 x}{x^2}, \quad x \rightarrow \infty \quad (\text{B.21})$$

$$R^{\text{symp1}}(x) \rightarrow \frac{x^4}{135}, \quad x \rightarrow 0, \quad \text{and} \quad 1 + \frac{\pi}{2} \frac{\cos x}{x}, \quad x \rightarrow \infty \quad (\text{B.22})$$

APPENDIX C INTERBAND TRANSITION

The optical properties of simple polyvalent metals are known to show an interband transition. Because these nearly free electron metals have the inverse square root singularities in the joint density of states, which has direct relation with the optical conductivity, these metals have the optical absorption associated with the energy gap arising from the singularity.

Theoretically, the concept of pseudopotential, which is on the basis of the idea of the screening of the ion by electrons, allows us to construct a model of nearly free electrons, which now feels only the weak pseudopotential. However, unlike the free electron case, the nearly free electrons suffer the coherent scattering by the Bragg plane even in the weak pseudopotential which greatly modifies the optical properties of metals. In other words, the existence of a periodic pseudopotential introduces an energy gap at Bragg planes. Thus, when the wave vector \vec{k} of an electron varies from one branch to another continuously, the energy changes discontinuously at $\vec{G}/2$ by $2|U_{\vec{G}}|$ when the periodic pseudopotential is expanded in a Fourier series such as

$$U(\vec{r}) = \sum_{\vec{G}} U_{\vec{G}} e^{i\vec{G} \cdot \vec{r}} \quad (\text{C.1})$$

where \vec{G} is the reciprocal lattice vector. Now $U_{\vec{G}}$ can be determined by the deHaas-van Alphen effect analysis or by the optical measurements.

A pseudopotential calculation of the aluminum energy band done by Ashcroft⁹⁷ found that a pair of bands may be substantially parallel when they are plotted in a plane parallel to the zone face. By using this fact, there are two different interband transitions: one is the parallel band transition and the other is the normal interband transition.

The electron wave function away from the Bragg plane can be regarded as a plane wave of a free particle, and the wave function near the Bragg plane can be written as a superposition of two plane waves. Ashcroft and Sturm⁹⁸ carried out the interband conductivity in a local pseudopotential approximation, and found the following results by separating the lower (-) and upper (+) bands:

$$\Psi_{\vec{k}} = \frac{1}{\sqrt{V}} \left[c_{\vec{k}} e^{i\vec{k} \cdot \vec{r}} + c_{\vec{k}-\vec{G}} e^{i(\vec{k}-\vec{G}) \cdot \vec{r}} \right] \quad (C.2)$$

where

$$c_{\vec{k}}^2 = \frac{1}{2} \left[1 + \gamma (1 + \gamma^2)^{-1/2} \right] \quad (C.3)$$

$$c_{\vec{k}-\vec{G}}^2 = \frac{1}{2} \left[1 - \gamma (1 + \gamma^2)^{-1/2} \right]$$

with

$$\gamma = \frac{\hbar^2}{2m} \frac{(\vec{k} - \vec{G})^2 - \vec{k}^2}{2U_{\vec{G}}} \quad (C.4)$$

and the energy in the upper bands (+) and lower bands (-) as

$$E_{\pm} = \frac{\hbar^2}{2m} (k_{\perp}^2 + k_{\parallel}^2) + |U_G^{\pm}| \left[|\gamma| \pm (1 + \gamma^2)^{1/2} \right] \quad (C.5)$$

where \vec{k} has been resolved into its components parallel (k_{\parallel}), perpendicular (k_{\perp}) to \vec{G} , and γ is a function of k_{\parallel} only by definition.

Now, as shown in Figure C.1(a), the transition for the lower band to the upper band has a constant interband energy difference, which is called "parallel band" absorption. Also the normal interband absorption is shown in Figure C.1(b). Clearly, these two different contributions are categorized as follows. For parallel band absorption, the condition written below should be satisfied at the Fermi energy

$$k^2 = \frac{2m}{\hbar^2} \left\{ E_F - |U_G^{\pm}| \left[\gamma + (1 + \gamma^2)^{1/2} \right] \right\} - k_{\parallel}^2 > 0 \quad (C.6)$$

Therefore, we have

$$\{k_{\perp}^{(+)}\}^2 - \{k_{\perp}^{(-)}\}^2 = \vec{G}^2 (2|U_G^{\pm}|/E_G^{\pm})(1 + \gamma^2)^{1/2} \quad (C.7)$$

with $E_G^{\pm} = \frac{\hbar^2}{2m} \vec{G}^2$ for fixed k_{\parallel} from Equation (C.5).

There is a high frequency cutoff in the parallel band transition which comes from the eigenvalue equation for k_{\parallel} at $E = E_F$

$$\hbar\omega_0 = 2(E_G^{\pm}E_F + U_G^2)^{1/2} - E_G^{\pm} \quad (C.8)$$

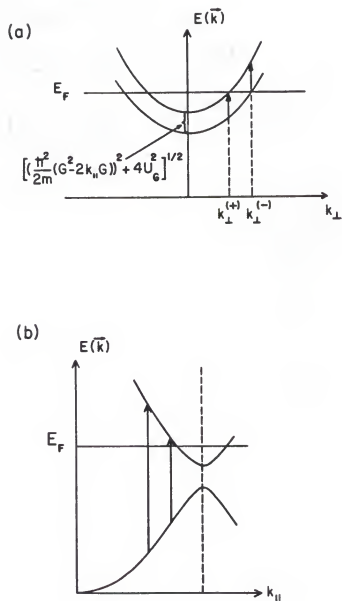


Figure C.1 Aluminum energy bands (from Reference 98)
 (a) Plotted for k near the L point zone face where parallel band character is exhibited and (b) normal interband absorption

or

$$\hbar\omega_0 = E_G^+ \left[\frac{2k_F}{G} - 1 \right] \quad (\text{C.9})$$

to the first order in (U_G^+/E_F) . And the gap energy becomes

$$E_+ - E_- = 2|U_G^+| (1 + \gamma^2)^{1/2} \hbar\omega_g (1 + \gamma^2)^{1/2} \quad (\text{C.10})$$

from Equation (C.5) or (C.7).

When the upper band is above the Fermi energy and the lower band is below

$$\frac{2m}{\hbar^2} \left\{ E_F - |U_G^+| \left[\gamma + (1 + \gamma^2)^{1/2} \right] \right\} < 0 \quad (\text{C.11a})$$

and

$$\frac{2m}{\hbar^2} \left\{ E_F - |U_G^+| \left[\gamma - (1 + \gamma^2)^{1/2} \right] \right\} > 0 \quad (\text{C.11b})$$

then we are in the region of the normal interband transition as shown in Figure C.1(b). Thus, we have

$$\{k_1^+\}^2 - \{k_1^-\}^2 = \left[\frac{E_F}{E_G^+} - \left(\frac{k_{\parallel}}{G} \right)^2 - \frac{|U_G^+|}{E_G^+} [\gamma - (1 + \gamma^2)^{1/2}] \right] \tilde{g}^2 \quad (\text{C.12})$$

Equation (C.12) can be rewritten as

$$\{k_1^+\}^2 - \{k_1^-\}^2 = \frac{\tilde{g}^2}{4E_G^+} (\hbar\omega + \hbar\omega_0) (\hbar\omega_1 - \hbar\omega) \quad (\text{C.13})$$

where

$$\hbar\omega = 2|U_G| (1 + \gamma^2)^{1/2}$$

and

$$\hbar\omega_1 = 2(E_G^* E_F + U_G^2)^{1/2} + E_G^*$$

Therefore, there is an upper cutoff frequency $\hbar\omega_1$ for the normal interband transition with $\hbar\omega_1 = \hbar\omega_0 + 2E_G^*$ and the transition takes place between $\hbar\omega_0$ and $\hbar\omega_1$.

For aluminum, there are two parallel transitions at U_{111} and U_{200} . However, the pseudopotential U_{111} gives an absorption at 0.44 eV ($3,550 \text{ cm}^{-1}$) which is weaker than the absorption due to U_{200} . U_{200} is responsible for the absorption at 1.52 eV ($= 12,260 \text{ cm}^{-1}$), which is strong enough to be seen in ordinary optical reflection measurement.

One remark on this type of calculation is that a broadening effect needs to be considered for a real system as done by Ashcroft and Sturm.⁹⁸ But Benbow and Lynch⁹⁹ found a good agreement with the Ashcroft and Sturm theory after introducing separate relaxation time for 0.44 eV, and Drude contributions to the optical conductivity.

APPENDIX D RECOVERY OF THE BULK NATURE

As we have seen in Chapter III, another peculiar behavior of the small particle is the interband transition in small aluminum particles. If this peculiar behavior is a true small particle phenomenon, then these characteristics will be lost when these small particles recover their bulk characteristics. One idea is to make a pure aluminum pellet by compressing the aluminum small particles and then study the reflectivity of the aluminum pellet.

The measured DC conductivity of the aluminum pellet was in the range of $100\text{--}200\ \Omega^{-1}\text{ cm}^{-1}$, which is a rather low value to judge the complete recovery of the bulk characteristics. However, since the aluminum pellets are slightly over the percolation threshold, we can, therefore, expect that the single small particle characteristics will disappear to some extent since particles are touching one another in this regime.

In order to see the interband transition clearly, a silver mirror was used from FIR to $20,000\text{ cm}^{-1}$ frequency range. Beyond $20,000\text{ cm}^{-1}$, an Al mirror was used and normalized to an Ag mirror since Ag has the screened plasma frequency at 3.9 eV ($\sim 31,500\text{ cm}^{-1}$).

The reflection measurements for two different aluminum pellets are shown in Figure D.1; one was made with $\langle r \rangle = 103\text{ \AA}$ Al small particles and the other was made with $\langle r \rangle = 280\text{ \AA}$ particles. There are

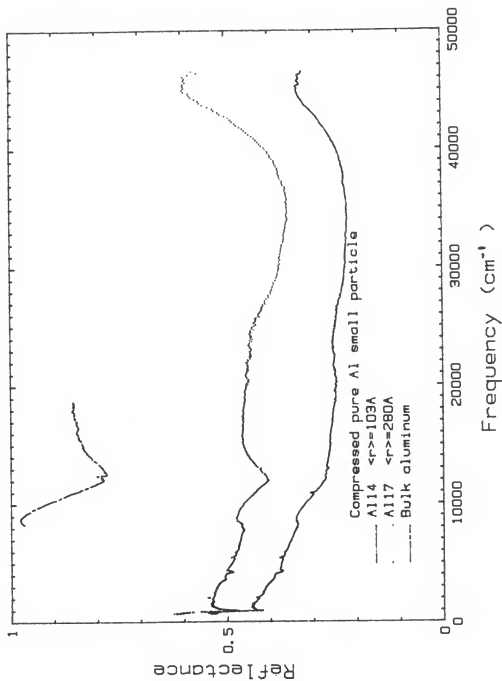


Figure D.1 Reflection data for two compressed aluminum small particle sample

two noticeable changes from Figure B.17 in the plot: One is the recovery of the bulk interband transition peak and the other is the trace of the broad absorption around $20,000\text{ cm}^{-1}$, which was interpreted as a result of the surface localization which still exists in $\langle r \rangle = 103\text{ \AA}$ particle data, but not in $\langle r \rangle = 280\text{ \AA}$ data. Also, the result of the Kramers-Kronig analysis is shown in Figure D.2. Note that the overall ac conductivity is quite similar to that of small particles obtained in Chapter III.

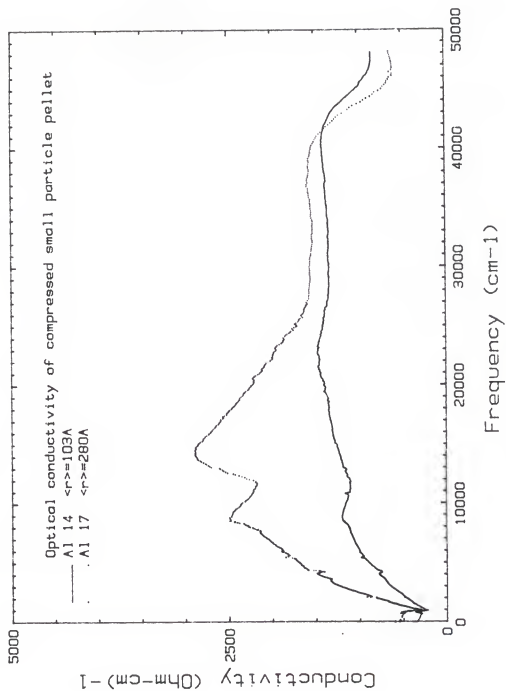


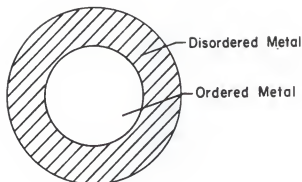
Figure D.2 Optical conductivity of compressed aluminum small particle pellets

APPENDIX E AN UNSUCCESSFUL MODEL CALCULATION

Ordered-Disordered Metal Model

As discussed in Chapter II, small particles have an oxide coating on their surface. Since the electron diffraction study of small aluminum particles did not show any direct evidence of well-crystalized aluminum oxide and the experimental study in MIR frequency done in Chapter III suggests that the degree of amorphism in the oxide coating of a small aluminum particle is even higher than the result of Reference 68 (remember that the amorphism tends to push the longitudinal modes of aluminum oxide towards the higher frequencies), it has been assumed that the oxide was formed in an amorphous state or formed in a nonstoichiometrical way. However, in actual calculation, we have assumed that the amorphous oxide is loss-free or negligible, if any. This assumption requires somehow further speculation because as we can see from Equation (4.100), the FIR absorption can be enhanced if $\sigma_1 \sim \sigma_2 \ll \sigma_{\text{Drude}}$. Also, Sievers¹⁰⁰ observed the similar anomalous FIR absorption by fully oxidized particles (evaporated in O_2 atmosphere). Additionally, the experimental evidence on the insensitivity of the absorption coefficient to the particle size variation suggests that the observed anomalous FIR absorption may not be due to the quantum size effect of pure electron gas confined in a restricted volume, rather may be due to the amorphous oxide coating with some finite but poor dc

(a)



(b)

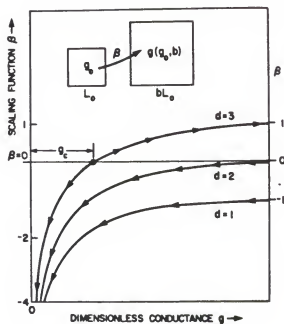


Figure E.1 A small particle model incorporated with Anderson insulator (a) An illustration of a small particle and (b) general behavior of Anderson system for various dimensions (from Reference 101)

conductivity as examined by Sen and Tanner⁵⁴ or with some combination of poor ac σ_1 and σ_2 as mentioned above if the amorphous oxide is an insulator.

Judging from this evidence, we can construct a small particle model which consists of two parts as shown in Figure E.1(a): One part is the core part with crystalline (ordered) metal; the other is the outer shell formed with the disordered metal (metal with lots of impurities and lattice defects), which we view within the Anderson localization model as a disordered electron system.

Anderson Localization

The disorder driven metal-insulator transition which is known as the Anderson transition is well understood and generally believed to occur in a 3-D system but not in 2-D and 1-D systems. By considering a tight-binding one-electron Hamiltonian,

$$H = \sum_i E_i c_i^\dagger c_i + \sum_{i \neq j} J_{ij} c_i^\dagger c_j \quad (\text{E.1})$$

where E_i is the energy level of an electron at site i , J_{ij} is the hopping integral between site i and j , and c_i^\dagger (c_i) is the creation (annihilation) operator of an electron at site i . Now, if we carry out a standard tight binding expansion of the eigenfunction Ψ with eigenvalue E in terms of atomic orbitals such as

$$\Psi = \sum_i a_i \phi_i \quad (\text{E.2})$$

where ϕ_i is the atomic orbital centered at site i . Therefore, we find an equation for the expansion coefficient as

$$E a_i = E_i a_i + \sum_j J_{ij} a_j \quad (\text{E.3})$$

Now, in the case of the nearest neighbor hopping only, we have an expression for the coefficient a_i such as

$$E a_i = E_i a_i + \frac{z}{2} J_{01} (a_{i-1} + a_{i+1}) \quad (\text{E.4})$$

where z is the number of the nearest neighbors.

Next, we want to set up a criterion for the metal-insulator transition in terms of the random impurity potential height w and the band width in the absence of disorder, U . When $w = 0$, we have a completely extended regime (i.e., $E_i = 0$), thus we find

$$E a_m = \frac{z}{2} J_{01} (a_{m-1} + a_{m+1}) \quad (\text{E.5})$$

By assuming a plane wave solution for the coefficient, a_m as

$$a_m = a_0 e^{im\alpha} \quad (\text{E.6})$$

we obtain a solution

$$E = z J_{01} \cos \alpha \quad (\text{E.7})$$

and the band width becomes

$$U = 2z J_{01} \quad (\text{E.8})$$

Next, by starting from $U = 0$ localized limit and treating the hopping term in Equation (E.1) as a perturbation, we can determine the localization criterion by simply examining the convergence condition for the perturbation series expansion. Assuming a uniform energy distribution over the nearest neighbor sites (i.e., $w = 2z|E_i - E_j|$), we have

$$\frac{\langle i | H_1 | j \rangle}{E_i - E_j} = \frac{2z J_{01}}{w} = \frac{U}{w} < 1, \text{ the condition of convergence} \quad (\text{E.9})$$

from the amplitude of mixing of the unperturbed states i with its neighboring states j to the first order. In other words, if we can treat the hopping term as a perturbation, electrons are localized. Otherwise, electrons are in the extended state. Therefore, we have the condition $U/W < 1$ for the Anderson localization.

Another important aspect of the Anderson localization is the scaling behavior discussed by Thouless¹⁰ and Abrahams et al.¹⁰¹ They considered a block of solid containing many sites with volume L^d in d -dimension and by comparing two energy scales (a similar way as done in Chapter I), the dimensionless, scale-dependent conductance $g(L) = \delta E(L)/\Delta E(L)$ was obtained as

$$g(L) = \frac{\hbar}{e^2} \sigma_0 L^{d-2} \quad (\text{E.10})$$

where $\sigma_0 = e^2 D v(E_F)$ and D is the diffusion constant. The key point of the formulation done by Thouless is that once we know a fundamental

conductance g_0 for a system with a cube of side L_0 , the conductance $g(bL_0)$ is completely determined by the fundamental conductance g_0 and the scale factor b . If we treat b as a continuous transformation such as

$$g[(1 + \epsilon)L] = f(\epsilon, g(L)), \quad \epsilon \ll 1 \quad (\text{E.11a})$$

$$= g(L) \left[1 + \epsilon \frac{d}{d} \frac{\ln g(L)}{\ln L} \right] \quad (\text{E.11b})$$

then we obtain the scaling behavior which can be specified by a differential scaling function $\beta(g)$:

$$\beta(g) = \frac{d}{d} \frac{\ln g(L)}{\ln L} \quad (\text{E.12})$$

From Equations (4.121) and (4.123), the limiting cases can be found as

$$\lim_{g \rightarrow \infty} \beta(g) = d - 2 \quad (\text{E.13})$$

and

$$\lim_{g \rightarrow 0} \beta(g) = \ln g \quad (\text{E.14})$$

The detailed behavior of function $\beta(g)$ is shown in Figure E.1(b). Note that there exists an unstable fixed point g_c which satisfies $\beta(g_c) = 0$ only for $d = 3$. The existence of g_c signals the Anderson transition.

Conductivity near the Anderson Transition

Vollhardt and Wölfle¹⁰² obtained a scaling function $\beta[g(L)] = d \ln g/d \ln L$ which is consistent with the results given in the previous section by using the self-consistent diagrammatic theory. Also, they found the generalized diffusion coefficient $D(\omega)$ of a disordered system within the same context.

The frequency dependent conductivity in the disordered electron system can be found by calculating the diffusion coefficient $D(\omega)$ for $2 < d < 4$ given by

$$D(\omega)/D_0 = 1 - \lambda d k_F^{2-d} \int_0^{k_0} dk \frac{k^{d-1}}{[-i\omega/d(\omega)] + k^2} \quad (E.15)$$

where the bare diffusion constant $D_0 = (\pi d m \lambda)^{-1}$ with $\lambda = \left(\frac{\hbar}{2\pi E_F \tau} \right)$, the disorder parameter. Here the cutoff k_0 is given by $k_0 = (\pi \lambda k_F)$.

Rearranging Equation (E.15) gives

$$\begin{aligned} \frac{D(\omega)}{D_0} = 1 - \frac{\lambda d}{d-2} \left(\frac{k_0}{k_F} \right)^{d-2} \\ + \lambda d \left(\frac{-i\omega}{D(\omega) k_F^2} \right)^{(d-2)/2} \int_0^{L(\omega)} dx \frac{x^{d-3}}{1+x^2} \end{aligned} \quad (E.16)$$

where $L(\omega) = [D(\omega)/(-i\omega\tau D_0)]^{1/2}$. Thus, we have the critical coupling constant λ_c from

$$\frac{D(\omega)}{D_0} = 1 - \frac{\lambda}{\lambda_c} \quad (E.17a)$$

Here

$$\lambda_c = \frac{d-2}{d} \left(\frac{k_0}{k_F} \right)^{2-d} = \left(\frac{d-2}{d} \pi^{2-d} \right)^{1/(d-1)} \quad (\text{E.17b})$$

For $\omega\tau \ll 1 - \lambda/\lambda_c$, Equation (E.16) can be solved by taking the $L(\omega) \rightarrow \infty$ limit in the conducting regime ($\lambda < \lambda_c$) and in the insulating regime ($\lambda_c \leq \lambda$) to obtain

$$\frac{\sigma(\omega)}{\sigma_0} = 1 - \frac{\lambda}{\lambda_c} + \alpha_d \frac{\lambda}{\lambda_c} \left[\frac{-i\omega\tau}{\sigma(\omega)/\sigma_0} \right]^{(d-2)/2} \quad (\text{E.18})$$

where $\alpha_d = \Gamma(d/2)\Gamma(2-d/2)$.

For $d = 3$, the cubic equation can be solved¹⁰³ to find

$$\frac{\sigma(\omega)}{\sigma_0} = (\omega_c\tau)^{1/3} \left[1 + \frac{\pi}{2} (-i/\omega_c)^{1/2} \right], \quad \omega \ll \omega_c \quad (\text{E.19a})$$

$$= (\omega_c\tau)^{1/3} \left(\frac{\pi}{2} \right)^{2/3} \left\{ \left(\frac{-i\omega}{\omega_c} \right)^{1/3} + \frac{2}{3} \right\}, \quad \omega \gg \omega_c \quad (\text{E.19b})$$

in the conducting regime ($\lambda < \lambda_c$). In the insulating regime ($\lambda \geq \lambda_c$), the solutions are

$$\frac{\sigma(\omega)}{\sigma_0} = (\omega_c\tau)^{1/3} \left(\frac{\pi}{2} \right)^2 \left[\frac{\pi^2}{2} \left(\frac{\omega}{\omega_c} \right)^2 - \frac{i\omega}{\omega_c} \right], \quad \omega \ll \omega_c \quad (\text{E.20a})$$

$$= (\omega_c\tau)^{1/3} \left(\frac{\pi}{2} \right)^{2/3} \left\{ \left(-\frac{i\omega}{\omega_c} \right)^{1/3} - \frac{2}{3} \right\}, \quad \omega \gg \omega_c \quad (\text{E.20b})$$

Here the crossover frequency ω_c is defined as

$$(\omega_c \tau) = \frac{4}{9\pi^2} \left(\frac{\lambda}{\lambda_c} - 1 \right)^3 \quad (\text{E.21})$$

and ω_c also can be written as

$$\omega_c = \frac{e^2 D_0}{\hbar \sigma_0} \xi^{-3} = \frac{V}{\hbar v(E_F)} \xi^{-3} \quad (\text{E.22})$$

in terms of the localization length ξ .

FIR Absorption Coefficient

Now, the FIR absorption coefficient of our new model is ready to be calculated by using the formula given by Equation (3.6). Since we are dealing with fairly large particles ($\sim 100 \text{ \AA}$) in the experiment, we describe the core part of a small particle with Drude dielectric function as a good approximation. In fact, the anomalous FIR absorption does not come from the core part in this model. Hence, it is almost independent of the choice of $\epsilon_m(\omega)$ for the core part of a small particle.

For the oxide coating, $\sigma_1(\omega)$ and $\sigma_2(\omega)$ calculated in Equation (E.20) is used. As a result, a remarkably good agreement between this model and the FIR experimental result was obtained as shown in Figure E.2. Notice that the contribution of the magnetic dipole term in addition to the electric dipole term shows a nice fit for large size particles.

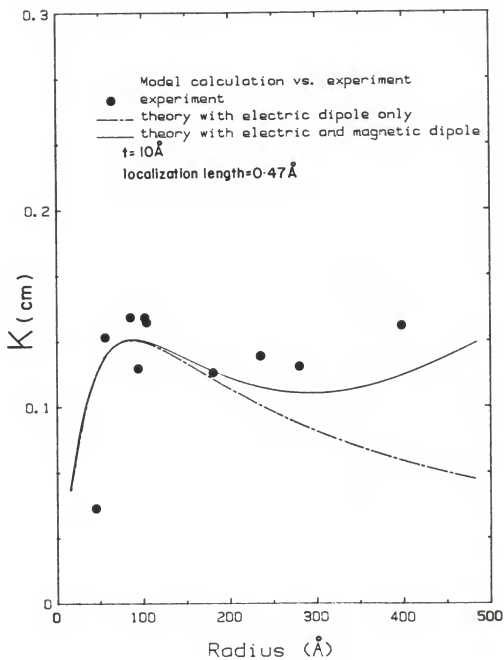


Figure E.2 A fit obtained from the model calculation

However, this model calculation fails to explain the superconducting state behavior of small particles as observed by Carr et al.¹⁰⁴ unless the Anderson insulator undergoes a superconducting transition.

REFERENCES

1. C. M. Hurd, Electrons in Metals (John Wiley and Sons, New York, 1975).
2. J. M. Ziman, ed., The Physics of Metals, Vol. 1 (Cambridge Univ. Press, Cambridge, England, 1969).
3. T. Holstein, Ann. of Physics 29, 410 (1964).
4. R. Kubo, J. Phys. Soc. Japan 17, 975 (1962).
5. S. D. Walck and J. J. Hren, private communication.
6. F. J. Dyson, J. Math. Phys. 3, 140 (1964).
7. L. P. Gor'kov and G. M. Eliashberg, Sov. Phys. JETP 21, 940 (1965).
8. N. F. Mott, Adv. Phys. 16, 49 (1967).
9. N. W. Ashcroft and N. D. Mermin, Solid State Physics, Chapter 18 (Saunders College, Philadelphia, 1976).
10. D. J. Thouless, Phys. Rev. Lett. 39, 1167 (1977).
11. A. F. Ioffe and A. R. Regel, Prog. Semicond. 4, 237 (1960).
12. The actual observed line width of the resonance peak is broader than the prediction given by the classical theory by a factor of 2 or larger, approximately.
13. D. B. Tanner, Ph.D. Dissertation, Cornell Univ. (1972).
14. D. B. Tanner, A. J. Sievers, and R. A. Buhrman, Phys. Rev. B11, 1330 (1974).
15. C. G. Granqvist, R. A. Buhrman, J. Wyns, and A. J. Sievers, Phys. Rev. Lett. 37, 625 (1976).
16. N. E. Russell, J. C. Garland, and D. B. Tanner, Phys. Rev. B23, 632 (1981).
17. G. L. Carr, R. L. Henry, N. E. Russell, J. C. Garland, D. B. Tanner, Phys. Rev. B24, 777 (1981).

18. E. Simanek, Phys. Rev. Lett. 38, 1161 (1977).
19. R. P. Devaty and A. J. Sievers, Phys. Rev. Lett. 52, 1344 (1984).
20. S. I. Lee, T. W. Noh, K. Cummings, and J. R. Gaines, Bull. Am. Phys. Soc. 30, 307 (1985).
21. A. E. Hughes and S. C. Jain, Adv. Phys. 28, 717 (1979) and references therein.
22. R. H. Doremus, J. Chem. Phys. 40, 2389 (1966).
23. A. B. Scott, W. A. Smith, and M. A. Thompson, J. Phys. Chem. 57, 757 (1953).
24. W. T. Doyle, Phys. Rev. 111, 1067 (1958).
25. S. C. Jain and N. D. Arora, J. Phys. Chem. Solids 35, 1231 (1974).
26. U. Kreibig, J. de Physique C2, 97 (1977).
27. C. G. Granqvist and O. Hunderi, Phys. Rev. B16, 3513 (1977).
28. S. Norrman, T. Andersson, and C. G. Granqvist, Solid State Commun. 23, 261 (1977).
29. B. N. J. Persson and A. Liebsh, Solid State Commun. 44, 1637 (1982).
30. U. J. Gibson and R. A. Buhrman, Phys. Rev. B27, 5046 (1983).
31. W. J. Kaiser and E. M. Logothetis, preprint (1984).
32. G. L. Carr, S. Perkowitz, and D. B. Tanner, "Far infrared properties of inhomogeneous materials," in Infrared and Millimeter Waves, Vol. 15, K. J. Button, ed. (Academic Press, Orlando, 1984).
33. R. L. Henry, Ph.D. Dissertation, The Ohio State Univ. (1980).
34. J. D. Jackson, Classical Electrodynamics, 2nd ed. (John Wiley and Sons, New York, 1975). See also L. D. Landau and E. M. Lifshitz, Electrodynamics of Continuous Media (Pergamon Press, New York, 1960), section 72 and 73.
35. D. Stroud and F. P. Pan, Phys. Rev. B17, 1602 (1978).
36. J. C. M. Garnett, Phil. Trans. Roy. Soc. (London) 203, 385 (1904); 205, 237 (1906).

37. C. Kittel, Introduction to Solid State Physics, 5th ed., p. 410 (John Wiley and Sons, New York, 1976).
38. D. A. G. Bruggeman, Ann. Physik (Peipz.) 24, 636 (1935).
39. D. Stroud, Phys. Rev. B12, 3368 (1975).
40. D. M. Wood and N. W. Ashcroft, Phil. Mag. 35, 269 (1977).
41. D. B. Tanner, Phys. Rev. B30, 1042 (1984).
42. D. M. Grannan, J. C. Garland, and D. B. Tanner, Phys. Rev. Lett. 46, 375 (1981).
43. J. P. Straley, Phys. Rev. B15, 5733 (1977).
44. D. J. Bergman and Y. Imry, Phys. Rev. Lett. 39, 1222 (1977).
45. S. Strässler, M. J. Rice, and P. Wyder, Phys. Rev. B6, 2575 (1973).
46. A. A. Lushnikov and A. J. Simonov, Phys. Lett. 44A, 45 (1973).
47. R. P. Devaty and A. J. Sievers, Bull. Am. Phys. Soc. 30, 307 (1985).
48. A. Kawabata and R. Kubo, J. Phys. Soc. Japan 21, 1765 (1966).
49. D. M. Wood and N. W. Ashcroft, Phys. Rev. B25, 6255 (1982).
50. R. Ruppin, Phys. Rev. B19, 1318 (1979).
51. W. A. Curtin, R. C. Spitzer, N. W. Ashcroft, and A. J. Sievers, Phys. Rev. Lett. 54, 1071 (1985).
52. Q. A. Curtin and N. W. Ashcroft, Phys. Rev. B31, 3287 (1985).
53. P. M. Hui and D. Stroud, Bull. Am. Phys. Soc. 30, 307 (1985).
54. P. N. Sen and D. B. Tanner, Phys. Rev. B26, 3582 (1982).
55. A. J. Glick and E. D. Yorke, Phys. Rev. B18, 2490 (1978).
56. H. P. Baltes and E. R. Hilf, Spectra of Finite Systems (Bibliographische Institut, Mannheim, 1976).
57. P. B. Allen, Phys. Rev. B3, 305 (1971).
58. Y. H. Kim and D. B. Tanner, unpublished (1984).

59. P. A. Lee and T. V. Ramakrishnan, *Rev. Mod. Phys.* 57, 287 (1985) and references therein.
60. C. G. Granqvist and R. A. Buhrman, *J. Appl. Phys.* 47, 2200 (1976).
61. M. V. Klein, Optics (John Wiley and Sons, New York, 1970), Chapter 6.
62. R. J. Bell, Introductory Fourier Transform Spectroscopy (Academic Press, New York, 1972).
63. R. B. Sanderson, "Fourier Spectroscopy," in Molecular Spectroscopy: Modern Research, Vol. I, K. Narahari Rao and C. W. Mathews, ed. (Academic Press, New York, 1972).
64. R. B. Sanderson and H. E. Scott, *Appl. Sop.* 10, 1097 (1971).
65. R. L. Henry and D. B. Tanner, *Infrared Physics* 19, 163 (1979).
66. K. D. Cummings, Ph.D. Dissertation, The Ohio State Univ. (1982).
67. A. S. Barker, *Phys. Rev.* 132, 1474 (1963).
68. T. S. Eriksson, A. Hjortberg, G. A. Niklasson, and C. G. Granqvist, *Applied Optics* 20, 2742 (1981).
69. C. G. Bohren and D. R. Huffman, Absorption and Scattering of Light by Small Particles (John Wiley and Sons, New York, 1983).
70. C. Kittel, Quantum Theory of Solids (John Wiley and Sons, New York, 1964).
71. D. Pines, Elementary Excitations in Solids (W. A. Benjamin, Inc., New York, 1964).
72. S. L. Adler, *Phys. Rev.* 126, 413 (1962).
73. M. Cini and P. Ascarelli, *J. Phys.* F4, 1998 (1974).
74. The particle surface plays an important role in the self-purification from impurities and lattice imperfections. See P. E. Chizhov, V. I. Petinov, and A. V. Grigorevski, *Solid State Comm.* 42, 327 (1982).
75. E. A. Shapoval, *Sov. Phys. JETP* 20, 675 (1965).
76. S. F. Edwards and P. W. Anderson, *J. Phys.*, F5, 965 (1975).
77. D. Sherrington and S. Kirkpatrick, *Phys. Rev. Lett.* 35, 1792 (1975).

78. K. B. Efetov, Sov. Phys. JETP 56, 467 (1982).
79. G. Parisi and N. Sourias, J. Physique 41, L403 (1980).
80. K. B. Efetov, Adv. Phys. 32, 53 (1983).
81. A. O. E. Animalu, Phys. Rev. B2, 282 (1970).
82. R. Kubo, J. Phys. (Paris) 38, C2, 69 (1977).
83. C. E. Porter, Statistical Theories of Spectra: Fluctuations, p. 55 (Academic Press, New York, 1965).
84. I. S. Gradshteyn and I. M. Ryzhik, Tables of Integrals, Series, and Products (Academic Press, New York, 1965).
85. R. P. Devaty and A. J. Sievers, Phys. Rev. B22, 2123 (1980).
86. F. Wooten, Optical Properties of Solids, Chapter 3 (Academic Press, New York, 1972).
87. U. Kreibig, J. Phys. F4, 999 (1974).
88. U. Kreibig and C. V. Fragstein, Z. Physik 224, 307 (1969).
89. P. Apell and D. R. Penn, Phys. Rev. Lett. 50, 1316 (1983).
90. A. A. Lushnikov and A. J. Simonov, Z. Physik 270, 17 (1974).
91. L. Genzel, T. P. Martin, and U. Kreibig, Z. Physik B21, 339 (1975).
92. R. Ruppin and H. Yatom, Phys. Stat. Sol. (b) 74, 647 (1976).
93. J. F. Tavel, K. F. Ratcliff, and N. Rosenzweig, Phys. Lett. 73A, 353 (1979).
94. J. F. Tavel, Ph.D. Dissertation, State Univ. of New York at Albany (1978).
95. M. L. Mehta, Random Matrices and the Statistical Theory of Energy Levels (Academic Press, New York, 1967).
96. F. J. Dyson, J. Math. Phys. 3, 140 (1962).
97. N. W. Ashcroft, Phil. Mag. 8, 2055 (1963).
98. N. W. Ashcroft and K. Sturm, Phys. Rev. B3, 1898 (1971).
99. R. L. Benbow and D. W. Lynch, Phys. Rev. B12, 5615 (1975).

100. A. J. Sievers, private communication with E. Simanek, Solid State Comm. 37, 97 (1981).
101. E. Abrahams, P. W. Anderson, D. C. Licciardello, and T. V. Ramakrishnan, Phys. Rev. Lett. 42, 673 (1979).
102. D. Vollhardt and P. Wölfle, Phys. Rev. Lett. 48, 699 (1982).
103. B. Shapiro, Phys. Rev. B25, 4266 (1982).
104. G. L. Carr, J. C. Garland, and D. B. Tanner, Phys. Rev. Lett. 50, 1607 (1983).

BIOGRAPHICAL SKETCH

Young Hoon Kim was born the third son of Chong Seo Kim and Bang Ji Kim (Chang) in Pusan, Korea, on November 30, 1954. He was raised and educated in a small town outside Seoul, Korea. After high school, he went to Seoul National University to major in materials engineering in 1973 and was awarded a B.S. in 1977. He joined the graduate school of his home university to continue his career as a materials scientist in 1978 after having been discharged from a 14-month military service. During this period, he developed an interest in physics and decided to go abroad for further studies. He started his graduate studies in physics at the Ohio State University in 1980 and he began his research under Professor David B. Tanner in 1981. In 1982, he moved to Florida with Professor Tanner and continued to work on the small particle problem at the University of Florida. He married Hye Kyong in 1980 and had a son, Eugene, in 1984.

I certify that I have read this study and that in my opinion it conforms to acceptable standards of scholarly presentation and is fully adequate, in scope and quality, as a dissertation for the degree of Doctor of Philosophy.



David B. Tanner, Chairman
Professor of Physics

I certify that I have read this study and that in my opinion it conforms to acceptable standards of scholarly presentation and is fully adequate, in scope and quality, as a dissertation for the degree of Doctor of Philosophy.



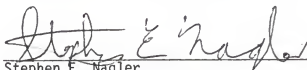
Neil S. Sullivan
Professor of Physics

I certify that I have read this study and that in my opinion it conforms to acceptable standards of scholarly presentation and is fully adequate, in scope and quality, as a dissertation for the degree of Doctor of Philosophy.



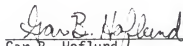
Pierre Sikivie
Associate Professor of Physics

I certify that I have read this study and that in my opinion it conforms to acceptable standards of scholarly presentation and is fully adequate, in scope and quality, as a dissertation for the degree of Doctor of Philosophy.



Stephen E. Nagler
Assistant Professor of Physics

I certify that I have read this study and that in my opinion it conforms to acceptable standards of scholarly presentation and is fully adequate, in scope and quality, as a dissertation for the degree of Doctor of Philosophy.



Gar B. Hoflund
Associate Professor of
Chemical Engineering

This dissertation was submitted to the Graduate Faculty of the Department of Physics in the College of Liberal Arts and Sciences and to the Graduate School and was accepted as partial fulfillment of the requirements for the Degree of Doctor of Philosophy.

May 1986

Dean, Graduate School